

REPORT DOCUMENTATION PAGE

Public reporting burden for this collection of information is estimated to average 1 hour per response, including the time for reviewing the data needed, and completing and reviewing the collection of information. Send comments regarding this burden estimate or any other aspect of this collection of information, including suggestions for reducing this burden, to Washington Headquarters Services, Directorate for Information Operations and Reports, 1204, Arlington, VA 22202-4302, and to the Office of Management and Budget, Paperwork Reduction Project (0334-0188).

3
ces, gathering
collection of
ighway, Suite

0401

1. AGENCY USE ONLY (Leave Blank)		2. REPORT DATE 1993		3. REPORT TYPE AND DATES COVERED Final	
4. TITLE AND SUBTITLE Measurements and Calculations of Loss due to Finite Conductivity and Surface Roughness in Microstrip Lines				5. FUNDING NUMBERS	
6. AUTHORS Todd W. Nichols					
7. PERFORMING ORGANIZATION NAME(S) AND ADDRESS(ES) University of Colorado				8. PERFORMING ORGANIZATION REPORT NUMBER	
9. SPONSORING/MONITORING AGENCY NAME(S) AND ADDRESS(ES) AFOSR/NI 110 Duncan Avenue, Room B-115 Bolling Air Force Base, DC 20332-8080				10. SPONSORING/MONITORING AGENCY REPORT NUMBER	
11. SUPPLEMENTARY NOTES					
12a. DISTRIBUTION AVAILABILITY STATEMENT Approved for Public Release				12b. DISTRIBUTION CODE	
13. ABSTRACT (Maximum 200 words) See attachment					
<div data-bbox="636 1094 1094 1234" data-label="Text"> <p>DISTRIBUTION STATEMENT A Approved for public release; Distribution Unlimited</p> </div> <div data-bbox="852 1461 1240 1539" data-label="Text"> <p>DTIC QUALITY INSPECTED 4</p> </div>					
14. SUBJECT TERMS				15. NUMBER OF PAGES	
				16. PRICE CODE	
17. SECURITY CLASSIFICATION OF REPORT Unclassified		18. SECURITY CLASSIFICATION OF THIS PAGE Unclassified		19. SECURITY CLASSIFICATION OF ABSTRACT Unclassified	
				20. LIMITATION OF ABSTRACT UL	

AFSC
AFSC OF TRANSMITTAL TO STIC
This technical report has been reviewed and is
approved for public release IAW AFR 190-12
distribution is unlimited.
John Rogers
STIC Program Manager

Approved for public release;
distribution unlimited.

19980505 005

MEASUREMENTS AND CALCULATIONS OF LOSS
DUE TO FINITE CONDUCTIVITY AND SURFACE ROUGHNESS
IN MICROSTRIP LINES

by

TODD W. NICHOLS

B.S., Clemson University, 1986

M.S., Clemson University, 1989

A thesis submitted to the
Faculty of the Graduate School of the
University of Colorado in partial fulfillment
of the requirements for the degree of
Doctor of Philosophy
Department of Electrical and Computer Engineering

1993

This thesis for the Doctor of Philosophy degree by

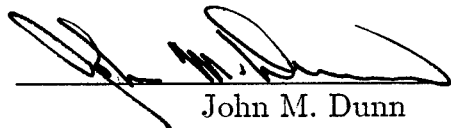
Todd W. Nichols

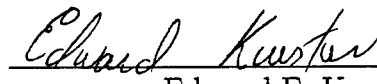
has been approved for the

Department of

Electrical and Computer Engineering

by



John M. Dunn

Edward F. Kuester

Date 4/30/93

Nichols, Todd W. (Ph.D., Electrical Engineering)

Measurements and Calculations of Loss Due to Finite Conductivity and Surface
Roughness in Microstrip Lines

Thesis directed by Assistant Professor John M. Dunn

Finite conductivity and surface roughness, two often significant causes of loss in microstrip lines, are examined in this dissertation. First, actual data are gathered. Gold lines are fabricated on semi-insulating gallium arsenide substrates. Losses are measured for the three canonical types of surface roughness in rectangular cross section lines: smooth lines, lines with grooves parallel to the line length, and lines with grooves transverse to the line length. Multi-line thru-reflect-line calibrations are performed, and on-wafer measurements are made on both long lines and two-port gap-coupled resonators. Data are compared with other methods of loss calculation, including commercial software.

The second major effort is solution of an exact integral equation for the current distribution in the strip conductor of a microstrip line on a perfect dielectric above a perfect ground plane. The strip conductor may have finite conductivity and arbitrary edge shape. A quasi-transverse electromagnetic mode is assumed and the moment method is applied to a discretized strip. The resulting matrix equation is a nonlinear complex eigenvalue problem for which the eigenvalues are the propagation constants of the possible modes. The real part of the dominant eigenvalue is the desired loss. The case with air dielectric ($\epsilon_r = 1$) is investigated.

ACKNOWLEDGMENTS

I would like to thank the Air Force Systems Command, the Air Force Office of Scientific Research, and Wright Research and Development Center for sponsoring this research.

I would like to thank the following people of the Avionics Laboratory at the Wright Research and Development Center for all their help, suggestions, and guidance: Mark Calcaterra, Carol Isbell, Brenda Johnson, Misoon Mah, Dave May, Phil Mumford, Bob Neidhard, Tony Quach, Kitt Reinhardt, Russ Scherer, Keith Stamper, and George Wilder.

A special thanks to Drs. John Dunn and Edward Kuester for their patience and assistance in the carrying out of this research and the writing of this document.

Finally, a heartfelt thanks to those people very close to me: my mother and father, and my wife Dottye. You now again have a son and a husband (respectively).

CONTENTS

Chapter

I. INTRODUCTION	1
1.1 Motivation	1
1.2 Effects of Finite Conductivity in Microstrip	2
1.3 Effects of Surface Roughness in Microstrip	4
1.4 Arrangement of the Dissertation	6
II. DESIGN AND FABRICATION OF A WAFER SUITABLE FOR LOSS MEASUREMENT	9
2.1 Design goals	9
2.2 Wafer inventory	12
2.3 Fabrication	13
2.3.1 Preliminaries	13
2.3.2 Grooves – first mask level	17
2.3.3 Front metal – second mask level	18
2.3.4 Wafer thinning	19
2.3.5 Vias – third mask level	23
2.3.6 Back metallization and demounting	29
III. LOSS MEASUREMENT METHODOLOGY	35
3.1 Thru-reflect-line (TRL) calibration	35
3.1.1 What is calibration?	35
3.1.2 TRL calibration and standards	36
3.1.3 NIST multi-line TRL calibration	42

3.1.4	Sources of error	43
3.2	Extraction of loss from $ S_{21} $ measurements on long lines	45
3.3	Extraction of loss from two-port gap-coupled resonator measurement	46
3.3.1	Extraction of loss from resonator parameters	46
3.3.2	Nonlinear curve fit to standard circuit model	48
3.4	Consideration of ground plane loss	53
IV.	LOSS MEASUREMENT RESULTS AND COMPARISONS	56
4.1	TRL extraction results	56
4.2	Direct $ S_{21} $ results from long lines	58
4.3	Two-port gap-coupled resonator results	59
4.4	Data from other methods and sources	61
4.4.1	Approximate calculations	61
4.4.2	Hewlett-Packard Microwave Design System (MDS)	72
4.4.3	Other experimental data	74
4.5	Comparisons	75
V.	SOLUTION OF THE INTEGRAL EQUATION FOR THE CURRENT DISTRIBUTION IN A STRIP CONDUCTOR	85
5.1	Basic integral equation solution technique [44]	85
5.2	Problem statement	86
5.3	Air dielectric case (substrate $\epsilon_r = 1$)	87
5.3.1	Discretization and application of Galerkin's method	87
5.3.2	Computer implementation	91
5.4	Perfect dielectric case (substrate $\epsilon_r \geq 1$)	96
VI.	CONCLUSIONS	97
	Bibliography	99
	Appendix	
A.	INITIAL WAFERS	103

A.1 Non-via-hole coplanar-to-microstrip transition	103
A.2 First wafer designs	106
B. MEASUREMENT SETUP	110
B.1 Power Up Sequence and Station Assembly	110
B.2 Mechanics of Probing	113
C. CITIFILE FORMAT CONVERSION	116

FIGURES

Figure		
1.1	"Perfect" microstrip model	2
1.2	Microstrip with real-life imperfections	2
2.1	Cross section of microstrip line with parallel grooves	11
2.2	Coplanar waveguide to microstrip transition	12
2.3	Calibration standards, resonators, and lines on the wafer . . .	14
2.4	View of the entire wafer	15
2.5	Scanning electron microscope photograph of etched grooves in a GaAs wafer	20
2.6	Expose mask to photoresist-covered GaAs substrate	22
2.7	Develop first layer of photoresist	22
2.8	Develop second layer of photoresist	23
2.9	Evaporate titanium and gold metal layers	23
2.10	Liftoff unwanted metal with acetone	24
2.11	Finished structure with vertical edge	24
2.12	Etched grooves and deposited gold near transverse resonator gap	25
2.13	Locations for wafer thickness measurements	26
2.14	Expose via hole mask to photoresist layer on backside	29
2.15	Develop photoresist	30
2.16	Etch silicon nitride "mask" layer and strip photoresist	30
2.17	Etch via holes, evaporate gold seed layer, and electroplate gold ground plane	31
2.18	Freshly etched via holes	31

2.19	Via holes with electroplated ground plane	32
2.20	Dektak plot of electroplated gold ground plane thickness . .	32
3.1	Partitioning of a real network analyzer system into a perfect network analyzer, error boxes, and the device under test	37
3.2	Standard transmission line model of a two-port gap-coupled resonator	47
3.3	Standard series RLC circuit model for resonator	49
3.4	Effect of varying $ S_{21} _{max}$ on the nonlinear curve fit	50
3.5	Effect of varying f_o on the nonlinear curve fit	51
3.6	Effect of varying Q_l on the nonlinear curve fit	52
3.7	Example of a "poor" fit	53
3.8	Example of a "good" fit	54
3.9	Numerically computed ground plane loss	55
4.1	Effective relative dielectric constant extracted from TRL calibration on wafer 6	57
4.2	Loss extracted from TRL calibration on wafer 6	58
4.3	Smooth loss extracted from line 2 $ S_{21} $ on wafer 6	59
4.4	Parallel loss extracted from line 3 $ S_{21} $ on wafer 6	60
4.5	Transverse loss extracted from line 2 $ S_{21} $ on wafer 6	61
4.6	Comparison of smooth, parallel, and transverse total losses .	62
4.7	Comparison of smooth, parallel, and transverse losses of strip	63
4.8	Comparison of smooth, parallel, and transverse resonator losses on Wafer 5	64
4.9	Comparison of parallel and transverse resonator losses on Wafer 6	65
4.10	$\epsilon_{re}(f)$ calculated from design formulas	70
4.11	Loss calculated from design formulas for $h = 96\mu$, variable roughness	72
4.12	Loss calculated from design formulas for $h = 98\mu$, variable roughness	73
4.13	Loss calculated from design formulas for $h = 100\mu$, variable	

roughness	74
4.14 Loss calculated from design formulas for rms roughness = 0.125μ , variable h	75
4.15 Loss calculated with MDS for $h = 96\mu$, variable roughness . .	76
4.16 Loss calculated with MDS for $h = 98\mu$, variable roughness . .	77
4.17 Loss calculated with MDS for $h = 100\mu$, variable roughness .	78
4.18 Loss calculated with MDS for rms roughness 0.125μ , variable h	79
4.19 Comparison of TRL and S-parameter measured smooth losses	81
4.20 Comparison of the measured and calculated smooth losses . .	82
4.21 Comparison of the measured and calculated parallel losses . .	83
4.22 Comparison of the measured and calculated transverse losses	84
5.1 Geometry of the microstrip problem	87
5.2 Discretization of the strip into a mesh of rectangular cells . .	92
5.3 Nomenclature for evaluation of the contour integrals for primed and unprimed cells	95
A.1 Coplanar probe to microstrip transition without vias	104
A.2 Impedance of non-via-hole coplanar transition for first wafer de- sign	105
A.3 Impedance of non-via-hole coplanar transition for second wafer design	106
A.4 Layout of first wafer design	107
A.5 Layout of second wafer design	108
B.1 Block diagram of the microwave measurement system at the Uni- versity of Colorado at Boulder	111

TABLES

Table

2.1	Complete wafer inventory	16
2.2	Resonator frequencies	17
2.3	Major processing steps	18
2.4	Groove lithography and etching steps	19
2.5	Front metal lithography, metallization, and liftoff steps	21
2.6	Wafer thinning steps	25
2.7	Measured wafer and ground plane thicknesses (microns)	27
2.8	Via hole lithography and etching steps	28
2.9	Back metallization and demounting steps	33
4.1	Wafer 6 R5P and R1P Curve Fit Statistics	66
4.2	Wafer 6 R2T Curve Fit Statistics	67
4.3	Wafer 5 R3S, R3P, R3T (Resonator 3: Smooth, Parallel, Transverse) Curve Fit Statistics	68
4.4	Goldfarb and Platzker Resonator Data	80
5.1	Basis function definitions	93
5.2	Dot product evaluations	94
C.1	Example HP 8510 raw data file in citifile format	120

CHAPTER I

INTRODUCTION

1.1 Motivation

The lowly microstrip transmission line has become firmly entrenched in such applications as hybrid microwave integrated circuits (MIC's) on ceramic and polytetrafluoroethylene (PTFE, or Teflon) substrates, and monolithic microwave integrated circuits (MMIC's) on silicon and gallium arsenide (GaAs). We live in an imperfect world, and microstrip is also subject to imperfection—the imperfection of loss: loss due to radiation, imperfect dielectrics, and imperfect conductors. Radiation losses arise from discontinuities, dielectric losses are due to finite resistivity or leakage of the substrate, and conductor losses—the subject of this dissertation—are the result of finite conductivity and surface roughness of the line's conductors.

Figure 1.1 shows the geometry of a “perfect” microstrip with perfect, lossless dielectric and conductors and zero-thickness strip conductor. The first step toward reality is to acknowledge that the strip has some nonzero thickness t . The substrate has a loss tangent which, for good microwave substrates, can usually be ignored (otherwise, it is not a very good substrate). The next step is to include effects of a finite conductivity σ . In this dissertation, the conductor losses dominate, both in the substrates considered and in the phenomena studied; therefore the loss tangent will be neglected. Finally, no metallic or ceramic surface is perfectly smooth. So we introduce a degree of surface roughness (usually given as a root-mean-square amplitude of the cross-section of the

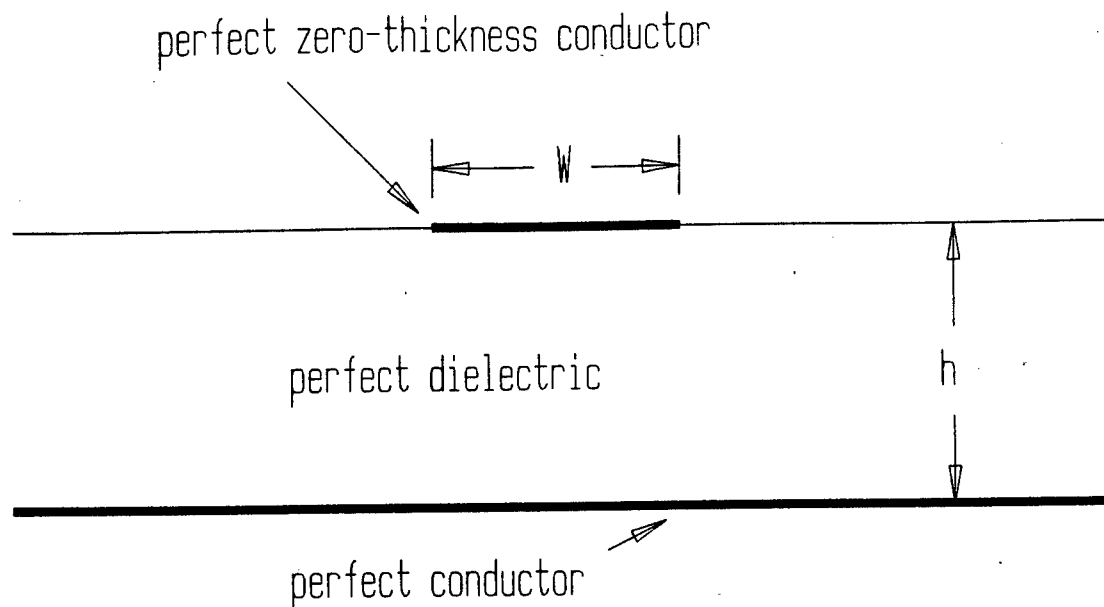


Figure 1.1 "Perfect" microstrip model

substrate height variation), and arrive at the "real-world" microstrip depicted in Figure 1.2.

Conductor and surface roughness losses in microstrip have been examined in great detail previously (see, for example, [1-7]); Wheeler's incremental inductance rule has especially seen considerable use [1]. This document, though, presents measurements made on a controlled rough surface, as well as examination of an integral equation which is not usually used for loss calculations.

1.2 Effects of Finite Conductivity in Microstrip

The conductor loss in a transmission line supporting a quasi-TEM mode is usually calculated with a perturbational technique [8-9]. Using transmission line theory, we can write a power-current definition of the line's characteristic impedance:

$$P = Z_0 |I|^2 \quad (1.1)$$

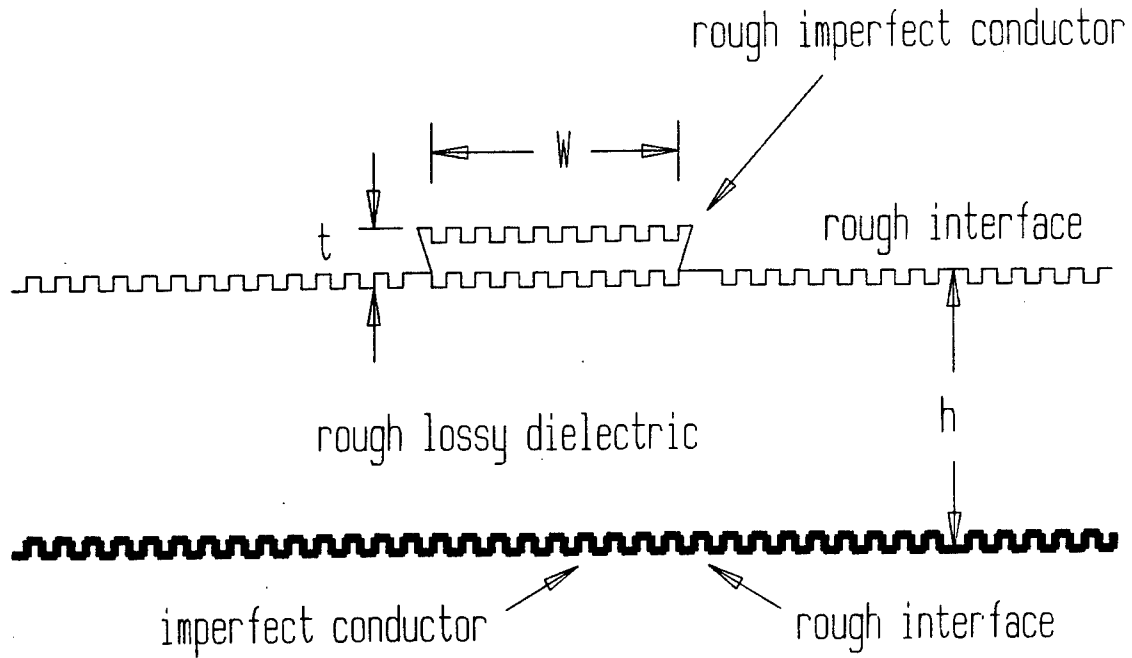


Figure 1.2 Microstrip with real-life imperfections

where Z_o is the characteristic impedance and I is the current flowing down the line. Substituting in the $I_+ e^{-\alpha z}$ form of a wave traveling in the positive z direction, we have

$$P = Z_o |I_+|^2 e^{-2\alpha z} \equiv P_o e^{-2\alpha z} \quad (1.2)$$

where P_o is the power at $z = 0$ and z is the direction of the line. Now the rate of power loss per unit length at some position z is given by

$$P_L = -\frac{\partial P}{\partial z} = 2\alpha P_o e^{-2\alpha z}; \quad (1.3)$$

therefore

$$\alpha = \frac{P_L}{2P} \text{ nepers/unit length} \quad (1.4)$$

This is the classic relation from which most derivations start.

The next step is to find and evaluate expressions from the two powers

in Equation (1.4); usually a Poynting vector approach is taken:

$$P = \frac{1}{2} \Re \int_S \bar{\mathbf{E}} \times \bar{\mathbf{H}}^* \cdot \bar{\mathbf{a}}_z dS \quad (1.5)$$

and

$$P_L = \frac{1}{2} \Re \oint_{C_1+C_2} (\bar{\mathbf{E}} \times \bar{\mathbf{H}}^*) \cdot \bar{\mathbf{a}}_n dS \quad (1.6)$$

where C_1 and C_2 are the contours of the two conductors and S is the line's cross section. P is the power flowing down the line. P_L is the (lost or dissipated) power flowing into the conductor. These two equations are still general.

Conventional approaches simplify (1.5) and (1.6) with the usual assumption that the Leontovitch impedance boundary condition is valid (that is, the line thickness t is much greater than a skin depth, and the conductor surfaces are smooth). That means that the fields internal to the conductor do not need to be calculated. Unfortunately, for modern microstrip lines this approximation is often not valid. Other more drastic measures are called for.

1.3 Effects of Surface Roughness in Microstrip

It is accepted that, since metals are known to have finite conductivity (for gold, $\sigma = 4.1\text{E}7$ S/m and for copper, $\sigma = 5.8\text{E}7$ S/m), there will be some impediment to wave transmission and that it must be calculated. This is usually taken into account by relating power dissipation to the current in a conductor through Ohm's Law ($\bar{\mathbf{E}} = \sigma \bar{\mathbf{J}}$). This means that the integrals in (1.5) and (1.6) have to be evaluated, as previously mentioned. But what about surface roughness? Surely we can see that the substrates (and metals) we are using are smooth? Let us examine them somewhat closer. As we do, let us bear in mind that the skin depth δ (in gold) can range from about 0.97μ at 6 GHz to about 0.38μ at 40 GHz (the frequency range examined in this work). Remember, this is the dimension which determines whether or not a surface really is rough.

Only two substances (substrate and conductor) make up microstrip, so only those two substances can be rough. First we look at substrates. Microstrip lines are fabricated on three main classes of dielectrics: PTFE, which is easily worked and inexpensive; ceramics (predominately aluminum oxide), which are hard to work and fairly expensive; and semiconductors, which are used in MMIC's and may have a wide cost and workability range. PTFE's surface roughness depends on processing and the amount and type of ceramic fibers mixed in with it, and may range from 0.3μ to 1.0μ [10]. For ceramics we will concentrate on alumina (Al_2O_3) since it is the most common [11]. Alumina is available in several purities, and the purity affects post-firing surface roughness. Of course the surface can be polished, but since alumina is 9 on the Mohs scale of hardness, it is expensive to do so. Fired unpolished 99.5% alumina may have a surface roughness from 1μ to as high as 8μ , depending on forming technique [12-13], whereas 96% alumina (cheaper) may have a gross surface roughness of 20μ . Polishing can reduce this roughness to 0.04μ on 99.5% alumina [14]. So both PTFE and unpolished ceramic substrates can lead to real problems. Semiconductors are usually supplied from the wafer manufacturer optically flat, so there is no substrate roughness problem there.

Now we will consider the metal. Conductor can join substrate, in which case the rougher and tougher material's roughness dominates, or it can join air (the top of the strip) where the metal's roughness (process dominant) matters more. Copper is usually rolled or electrodeposited; rolled copper surface roughness may range from 0.1μ on the substrate side to 1.0μ on the air side [15]. Electrodeposited copper, on the other hand, is a factor of ten rougher, which would seem to preclude its use; however, it adheres much better to the substrate [16]. Gold is also sometimes used on ceramic substrates. Gold is also the primary metal used on semiconductors. It is either evaporated or

electroplated onto the substrate; the electroplating usually takes place over an evaporated seed layer that may be a few thousand Angstroms thick. Gold electroplated onto wafers made at Wright-Patterson Air Force Base was seen to have a surface roughness of about 0.1μ to 0.4μ as determined from Dektak measurements.

One way to approximate surface roughness to make it amenable to analysis is to look at grooves, both parallel to and transverse to current flow in the strip. Morgan [17] made some early studies on the effects of grooves on attenuation. For parallel grooves with width of channel equal to width of mesa, as the groove depth to skin depth ratio increases, the attenuation increases also. Conceptually, this is because the current is trying to flow through a layer which is reduced in area (by the grooves), so there is less metal to flow through. For transverse grooves, as this ratio increases, the path length for the current flow effectively increases, so the attenuation goes up. If groove depth equals groove width, the loss could double. Of course, in real life the surface roughness is not this ideal, but it is obvious that surface roughness – especially that on the order of a skin depth – can noticeable increase the loss.

1.4 Arrangement of the Dissertation

The first major task in this research was the design and fabrication of a gallium arsenide (GaAs) MMIC with gold conductors. Chapter 2 details the items contained on the wafer and the techniques used to process it. This effort was spent mostly in the clean room; there is little to show for it but the wafers themselves – and a fairly well-debugged process flow. Producing these wafers, however, consumed much time. Trial and error associated with the initial wafers (as detailed in Appendix A) was a factor, as well as the fact that the final wafer design possessed via holes and required backside processing.

Chapter 3 investigates the loss measurement methodologies employed

to actually acquire data. Appendix B describes the hookup and use of the measurement equipment itself, since this facility — which is capable of probing on-wafer active devices to 40 GHz — took form mostly through this research; several good measurement habits were developed and documented. Since network analyzer calibration is an integral part of these procedures, calibration — particularly thru-reflect-line (TRL) calibration — is described. Measuring the loss of long lines directly and deducing the loss from resonator parameters are the two popular methods for loss measurement, and these two methods are scrutinized. Finally, the ground plane loss must be calculated and accounted for, since the ground plane is not roughened in this experiment.

The hard-won data are presented and discussed in Chapter 4. After a thorough discourse upon this data, results from traditional approximate formulas, other researchers, and commercial software calculations are compared with these numbers.

Chapter 5 marks a dramatic shift in subject matter. The solution of an exact integral equation for the current distribution in a finitely conducting strip of arbitrary cross section above a perfect dielectric upon a perfect ground plane is outlined. Applying the method of moments results in a complex nonlinear eigenvalue problem in which $\gamma = \alpha + j\beta$ is the eigenvalue. Starting values of γ are provided by traditional approximate formulas. The special case of air dielectric ($\epsilon_r = 1$) is first investigated; this approach eases and modularizes the solution. First, this case involves simple contour integrals instead of the more difficult to handle Sommerfeld integrals. Second, once the easier air dielectric case is working properly, the dielectric can be incorporated by changing the Green's function used. Finally, since the air dielectric case is easier to solve, it is easier to get working initially. With some forethought, the framework easily accommodates the nonunity dielectric constant later. There was not enough

time to complete addition of the dielectric, so only the air dielectric case is presented in detail.

CHAPTER II

DESIGN AND FABRICATION OF A WAFER SUITABLE FOR LOSS MEASUREMENT

How may one measure the loss due to finite conductivity and surface roughness in microstrip? Obviously the question necessitates the use of some form of microstrip transmission line. With that decided, the technology (substrate type, metallization type, and fabrication method) must be selected. But yet another question intrudes: How does one make a rough surface? This answer will surely influence the decision(s) about technology.

2.1 Design goals

Simply stated, the goal was to measure the loss in microstrip due to finite conductivity and surface roughness, in the frequency range where the strip thickness and surface roughness are both on the order of a skin depth. The effects of no surface roughness (on smooth lines), grooves running parallel to the line length (parallel grooves), and grooves running transverse to the line length (transverse grooves) were to be studied. These are the three different canonical problems. Any given surface roughness can be expressed as a linear combination of parallel and transverse roughness.

Under the terms of the Air Force fellowship, the clean room facilities at the Avionics Laboratory at Wright Research and Development Center (WRDC) located at Wright-Patterson Air Force Base in Dayton, Ohio were available. With this availability and with no readily discernable method for making a carefully controlled rough surface in more traditional microwave substrates (i.e.,

alumina and Teflon), the decision was made to fabricate gold lines on semi-insulating gallium arsenide (GaAs) wafers.

As noted earlier, surface finish and line thickness are of concern when their characteristic lengths are on the order of a skin depth. The skin depth δ for gold at 40 GHz is about 0.377μ and increases to 0.972μ as frequency decreases to 6 GHz. If the grooves are about one to one-half micron deep, then a strip conductor 2.5μ thick will both be thicker than twice the groove depth (so that there will always be metal across the width of the line) and be thin enough to be only a few skin depths thick.

Fifty ohms is the most common system characteristic impedance, and 100μ is the most common GaAs MMIC substrate thickness. Also the substrate must be thin in order to suppress undesired modes at frequencies to 40 GHz. Thus if a fifty-ohm line is desired on 100μ GaAs (whose relative permittivity is 12.9), its width must be about 73μ ; this value was calculated with standard design formulas [3, 5, 12]. For a line of these dimensions, the lowest-order TM mode cutoff frequency is about 292 GHz, and the lowest-order transverse strip resonance mode occurs at about 370 GHz; therefore this substrate is sufficiently thin. Also vertical edges are desired; therefore liftoff was the process used for fabricating the metal lines. Likewise vertical edges were desired for the grooves; reactive ion etching (RIE) for this shallow depth provides vertical side walls. As a backup, all grooves on the wafer run in the same direction, so that if chemical etching is ever desired, the anisotropy of certain etchants [18] will not be a factor. That is, all the grooves would always have the same cross-sectional appearance if chemical etching produced different edge slopes in different crystal lattice directions. Figure 2.1 shows the desired cross section of a microstrip line with grooves running parallel to the direction of propagation.

Finally, there is the question of actually making the measurements.

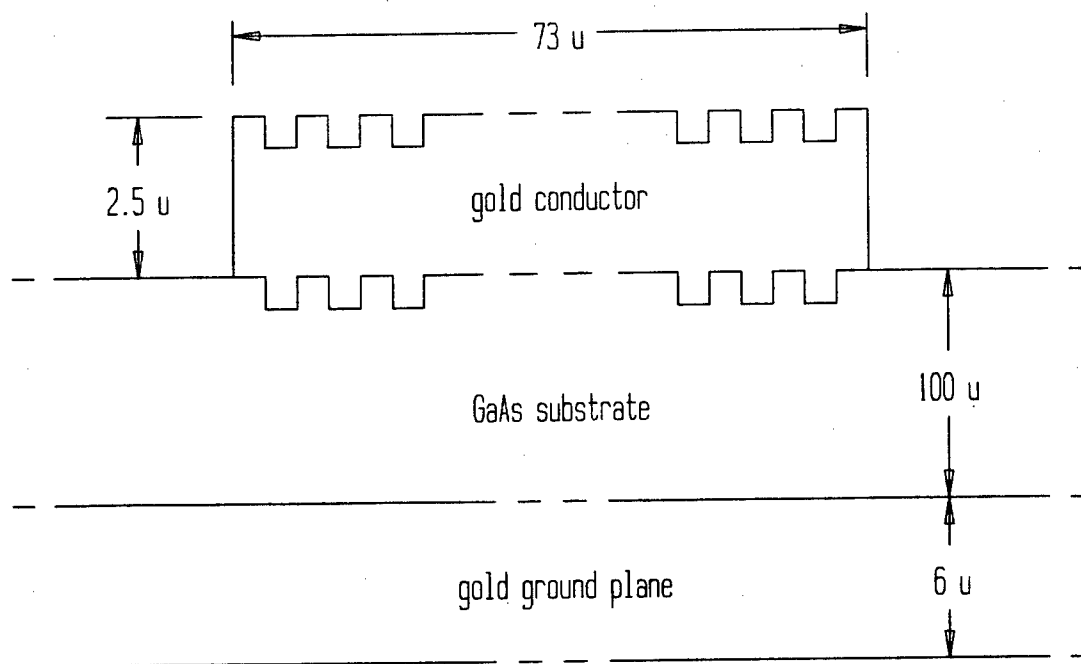


Figure 2.1 Cross section of microstrip line with parallel grooves (not to scale)

For less expensive and larger substrates, coaxial connectors are soldered onto the ends of the substrate. This approach is obviously infeasible for a wafer technology: on-wafer probing is required. Some sort of transition is therefore needed, because all wafer probes are variations of coplanar lines: ground-signal, ground-signal-ground (traditional coplanar waveguide), or other combinations. The microstrip ground, though, is on the bottom of the substrate and is normally inaccessible from the top of the wafer. Two approaches are available: using pads on the top surface, connected to the ground plane with metallized via holes; or using a large ground patch on the top surface whose reactance to ground is minimized in some frequency band of interest [19]. The latter approach was used first and later abandoned; it is presented in more detail in Appendix A. The resonant patch has the advantage of not requiring an extra mask layer and extra processing for via holes. However, it is a resonant struc-

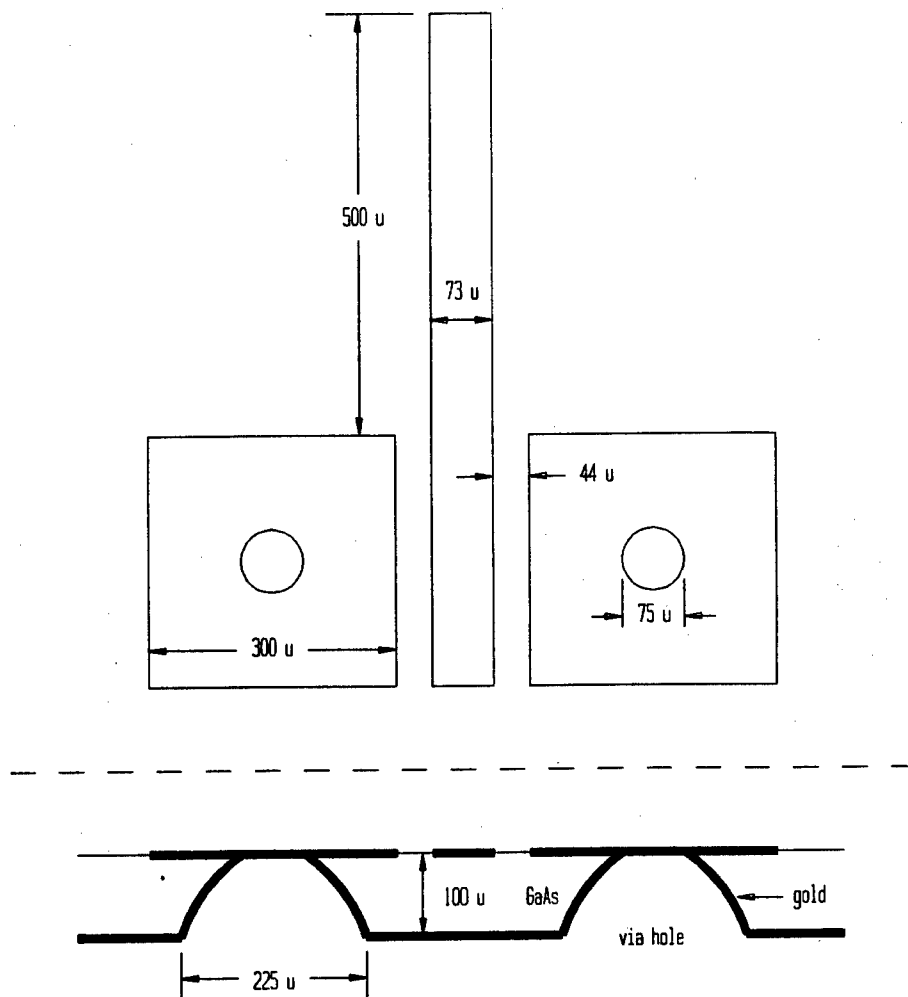


Figure 2.2 Coplanar waveguide to microstrip transition

ture and contributes to radiation losses. It also requires much more space on the wafer. Transitioning from wafer probes to microstrip with a via-hole transition is the standard method. Figure 2.2 shows the plan view and cross section of the transition used. The pad-to-line gaps are 44μ as shown in order to present a coplanar waveguide whose characteristic impedance is close to 50Ω ; this value was calculated with standard design formulas.

2.2 Wafer inventory

What should be included on the wafer? At a minimum, calibration

standards and the structures to be measured are required. There are two possible ways to make loss measurements. One method is to use TRL calibration with multiple lines (discussed in Chapter 3) to extract the loss; alternatively, after calibrating with TRL, the $|S_{21}|$ of a line can be measured directly. The other method is to fabricate a resonator and use it in one or more resonant modes: by measuring the resonant frequency, quality factor, and coupling coefficient, one can extract the loss. This method, though, only gives results at discrete frequencies. To satisfy adherents of both approaches and to make comparisons, both methods are used here. This means that sets of two-port gap-coupled resonators are present, as well as sets of long lines. Also, since some wafer area was available, structures were included to provide data for other researchers at the University of Colorado. Data on these structures are not presented in this dissertation.

As a precaution against low yield, two of every structure were included on the wafer. Moreover, every line and resonator is present in smooth, parallel, and transverse forms. In addition, the structures are spaced at least five, and usually eight to ten, substrate thicknesses apart to minimize coupling from structure to structure. The design of the particular calibration standards is discussed in Chapter 3. Figure 2.3 shows the structures present on the wafer, and Figure 2.4 is a view of the entire wafer. Table 2.1 is a detailed list of the structures present and their dimensions. Table 2.2 lists the frequencies at which the resonators will give loss measurements.

2.3 Fabrication

We will now discuss the actual fabrication procedures and process steps. This design process is essentially the same one used in GaAs MMIC foundries for commercial chips.

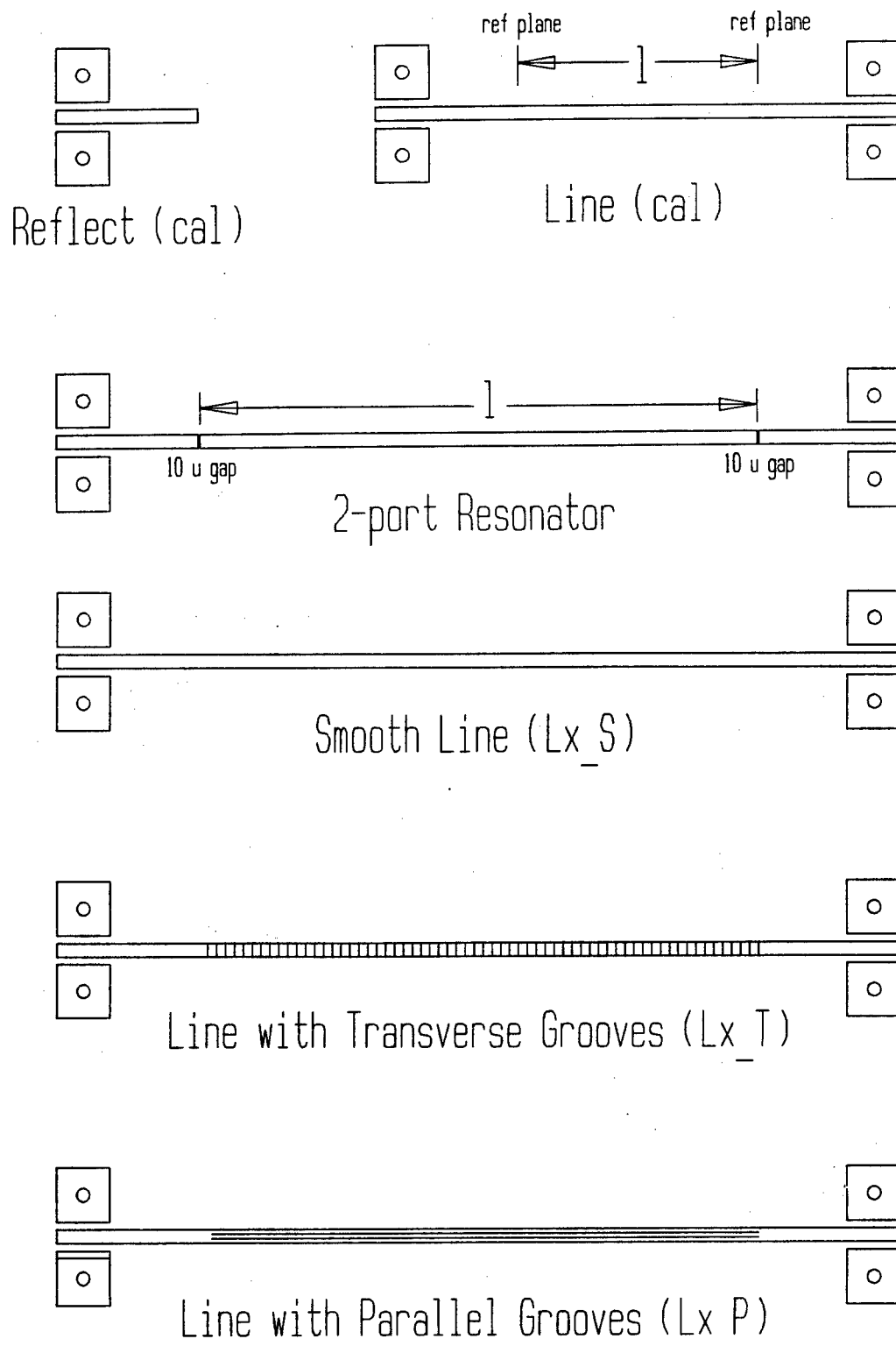


Figure 2.3 Calibration standards, resonators, and lines on the wafer

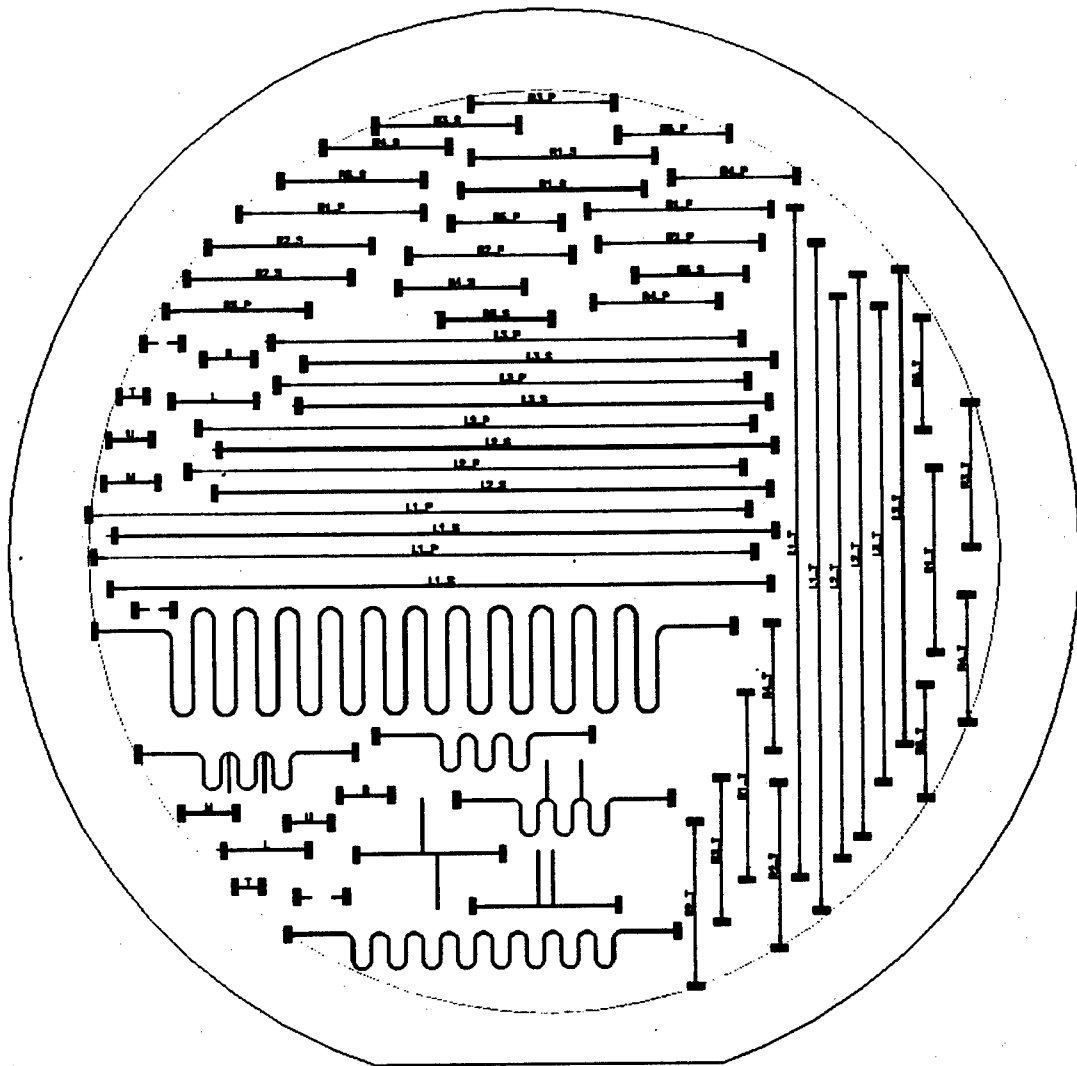


Figure 2.4 View of the entire wafer

2.3.1 Preliminaries

Prior to arriving at WRDC, the wafer design was completed at the University of Colorado, and a sketch was made. Upon arrival at WPAFB the design was entered into the Calma computer-aided design (CAD) system there. Chrome-on-glass masks were then made using electron-beam lithography.

Table 2.1 Complete wafer inventory

TRL Calibration Standards

- 4 - Offset opens (500 μ)
- 2 - Zero-length thru, T (1000 μ)
- 2 - Full-band line for 6-40 GHz, B (2121 μ)
- 2 - Lower-band line for 6-13 GHz, L (3713 μ)
- 2 - Middle-band line for 13-27 GHz, M (2289 μ)
- 2 - Upper-band line for 27-40 GHz, U (1769 μ)

Long Lines (2 of each line)

- 6 - 2.998 cm L1_S, L1_T, L1_P smooth, transverse grooves, parallel grooves
- 6 - 2.498 cm L2_S, L2_T, L2_P smooth, transverse grooves, parallel grooves
- 6 - 2.098 cm L3_S, L3_T, L3_P smooth, transverse grooves, parallel grooves

2-port Gap-coupled Resonators

- 6 - 7400 μ R1_S, R1_T, R1_P smooth, transverse grooves, parallel grooves
- 6 - 6450 μ R2_S, R2_T, R2_P smooth, transverse grooves, parallel grooves
- 6 - 5450 μ R3_S, R3_T, R3_P smooth, transverse grooves, parallel grooves
- 6 - 4650 μ R4_S, R4_T, R4_P smooth, transverse grooves, parallel grooves
- 6 - 3940 μ R5_S, R5_T, R5_P smooth, transverse grooves, parallel grooves

Miscellaneous Structures

- 1 - 13.66 cm smooth serpentine line
 - 3 - various serpentine lines with stubs (for other CU researchers)
 - 2 - double-stub resonators (for other CU researchers)
-

Table 2.2 Resonator frequencies

<u>Resonator Number</u>	<u>Length</u>	<u>Resonant Frequencies (GHz)</u>
1	7400 μ	7.0, 14.0, 20.9, 28.2, 34.6
2	6450 μ	8.0, 16.0, 23.9, 31.7, 39.5
3	5450 μ	9.4, 18.8, 28.1, 37.3
4	4650 μ	11.0, 22.0, 32.8
5	3940 μ	13.0, 25.8, 38.4

The starting material was two-inch-diameter semi-insulating GaAs wafers approximately 20 mils thick. They were already polished on one side and the major flat is parallel to the $\langle 100 \rangle$ crystal plane. Fifteen wafers were available at the beginning. Table 2.3 gives the order of the major steps in the fabrication process, and these steps will each be elaborated in the rest of this chapter. The processing steps were, unless noted otherwise, carried out in the Class 100¹ clean room in the Avionics Laboratory at WRDC. Such care is taken with this facility that it is often Class 50 or even 10.

2.3.2 Grooves – first mask level

The first step when masks are in hand is to fabricate the grooves in the substrate. Table 2.4 lists the steps. The general approach is to put down a layer of photoresist, expose the groove mask, develop, and use reactive ion etching to form the grooves. Care must be taken in exposing and developing because the grooves are one micron lines and spaces. It is very easy to over-expose or underexpose, and easy to leave too much photoresist behind or to

¹ Class 100 means that fewer than 100 particles with diameter greater than 100 μ are present per cubic foot of air.

Table 2.3 Major processing steps

-
- groove lithography
 - groove etch
 - front metal lithography
 - front metallization
 - liftoff
 - lapping and polishing
 - via hole lithography
 - via hole etch
 - back metallization
 - demounting
-

develop too much away. Close inspection under magnification after developing is mandatory. Figure 2.5 shows some fabricated grooves. Note that any particles in the photoresist where grooves are to be formed will distort the groove pattern in that area. This step is, therefore, very sensitive to contaminants in the photoresist, in the air, and in the tools (such as pipettes) used.

2.3.3 Front metal – second mask level

In this step the strip conductors of the microstrip structures are laid down. Table 2.5 gives the detailed process steps, while Figures 2.6 through 2.11 show graphically the steps involved. The liftoff process as given here results in vertical metal edges because the base photoresist is thicker than the desired metal thickness, and because the metal is deposited by evaporation—an essentially line-of-sight process. The overlap of the upper level of photoresist enables solvent to be used to dissolve photoresist underneath undesired metal so that

Table 2.4 Groove lithography and etching steps

Groove Lithography

Clean wafer with acetone, methanol, isopropyl 30 sec

Bakeout at 150°C for 10 min

Spin on 1400-27 photoresist at 4000 rpm 30 sec

Bake at 100°C for 5 min on hot plate

Edge removal - expose 405 nm UV 10 sec

Develop 5:1 DI:351 at 500 rpm 30 sec

DI rinse 30 sec

Expose mask (grooves) 405 nm UV 3 sec

Develop DI:351 at 500 rpm 13 sec

DI rinse 30 sec

Groove Etch

Bake at 100°C for 5 min on hot plate (to harden resist)

O₂ plasma etch 30 sec

HCl:H₂O 1:1 rinse 30 sec

RIE to 0.8 μ depth $\pm 2 \mu$

it will “lift off”; hence the name. Figure 2.12 shows a vertical edge on a 2.5 μ thickness of gold on a GaAs substrate.

2.3.4 Wafer thinning

This procedure, though low in number of process steps, is dangerous – both to the operator and to the wafer. In this step the wafer is reduced in thickness from 500 μ - 600 μ to the 100 μ which is the desired final substrate

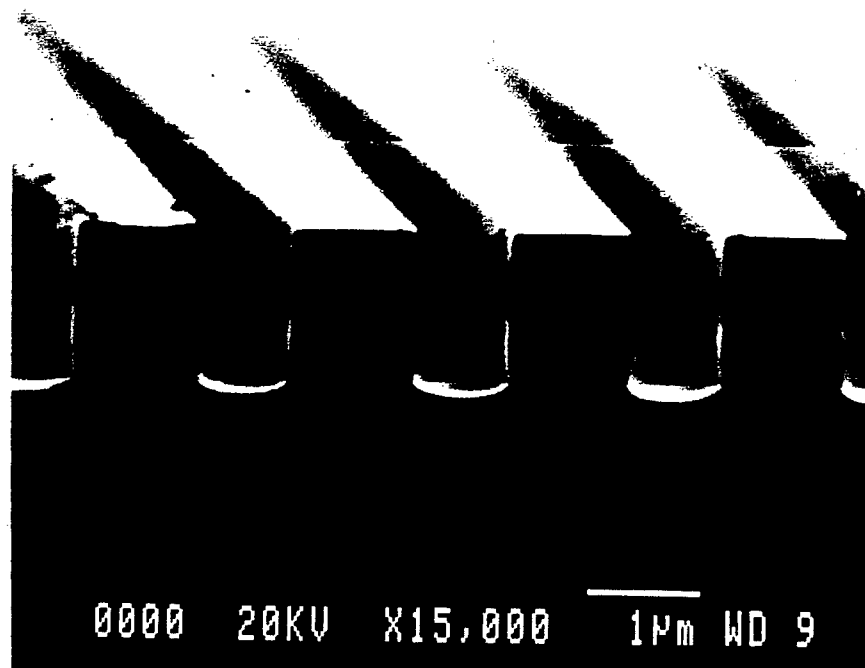


Figure 2.5 Scanning electron microscope photograph of etched grooves in a GaAs wafer

thickness. This step is dangerous to the wafer because GaAs is a very brittle and fragile material; as it gets thinner, its fragility increases and its toughness decreases. The substrate is also more sensitive, as it is lapped thinner and thinner, to being scratched by an errant large particle. If in the final stages of polishing, when the substrate is about $105\ \mu$ or so thick, a $5\ \mu$ particle used in the rough grinding gets in between the substrate and the grinding wheel, then it can scratch the substrate so deeply that smoothing it out will reduce the substrate to, say, $95\ \mu$. Also the grinding rate is not constant; it depends on the composition of the aluminum oxide and deionized water and Chlorox slurry. It is thus very easy to grind the wafer too thin. And if the wafer is not properly mounted to its supporting glass disk, parts of the wafer can fracture and flake

Table 2.5 Front metal lithography, metallization, and liftoff steps

Front Metal Lithography

Clean wafer with acetone, methanol, isopropyl 30 sec
Spin on PMGI at 4000 rpm 20 sec
Bake at 250°C for 5 min on hot plate
Spin on PMGI at 4000 rpm 20 sec
Bake at 250°C for 5 min on hot plate
Spin on PMGI at 4000 rpm 20 sec
Bake at 250°C for 5 min on hot plate
Spin on 1400-27 photoresist at 4000 rpm 30 sec
Bake at 100°C for 5 min on hot plate
Edge removal - expose 405 nm UV 10 sec
Develop 5:1 DI:351 at 500 rpm 30 sec
DI rinse 30 sec
Expose mask (lines) 320 nm UV at 12 mW/cm² for 42 sec
Develop 5:1 DI:351 at 500 rpm 27 sec
DI rinse 20 sec
DUV 10 mW/cm² 220 nm 900 sec
Develop SAL 101 at 500 rpm 60 sec
DI rinse 30 sec
Mask off structures (if needed) with 1400-27 photoresist
Bake at 100°C for 5 min on hot plate if structures masked

Front Metallization

HCl:DI 1:1 rinse 5 sec
DI rinse 30 sec
BOE:DI 1:1 rinse 5 sec
DI rinse 30 sec
Evaporate 200Å titanium sticking layer
Evaporate 2.5μ gold

Liftoff

Acetone soak approximately 15 min until liftoff begins
Acetone rinse on spinner until liftoff complete
Strip PMGI with 1165 at low boil 30 sec
DI rinse 10 sec
Clean wafer with acetone, methanol, isopropyl 30 sec
Bake at 150°C for 6 min on hot plate
Spin on wax at 2500 rpm for 30 sec and put glass disk on wafer

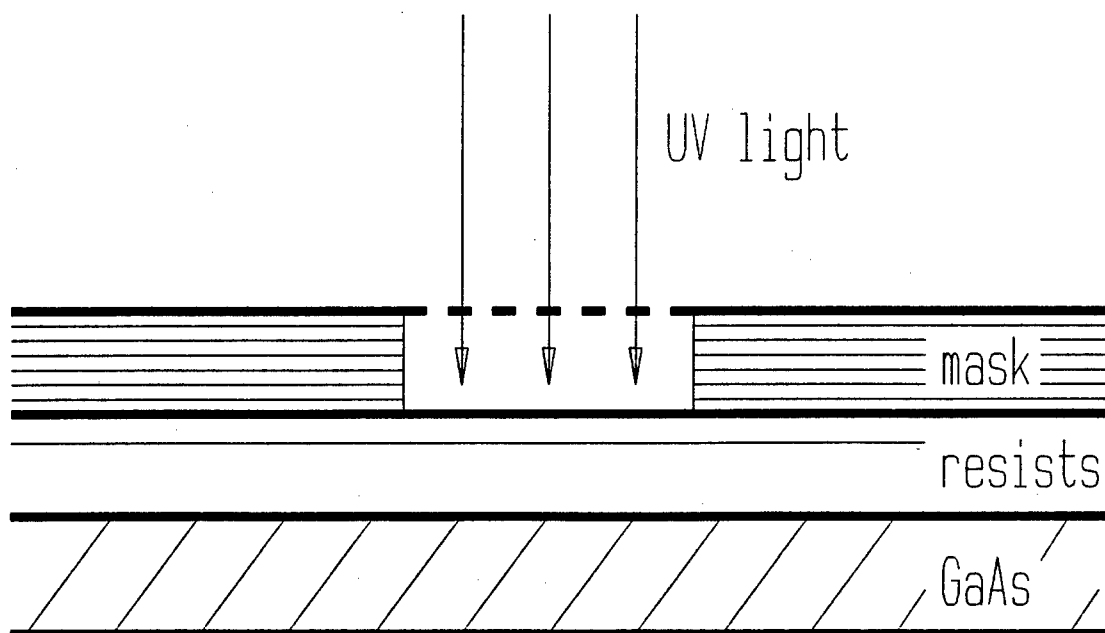


Figure 2.6 Expose mask to photoresist-covered GaAs substrate

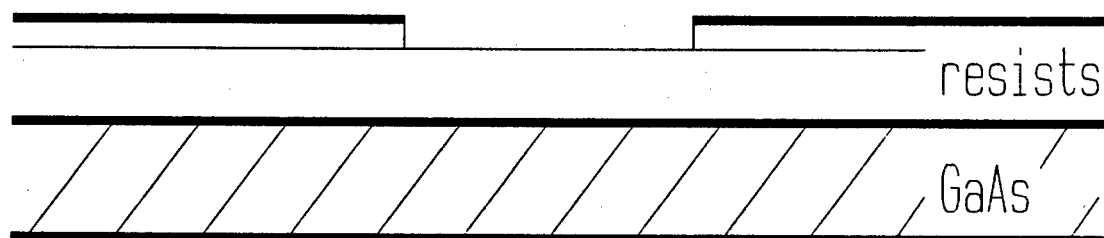


Figure 2.7 Develop first layer of photoresist

off during grinding or later in processing. The procedure is dangerous to the operator because small GaAs particles become mixed in with the slurry, and GaAs is carcinogenic. During grinding this slurry collects on various parts of the grinding machinery, dries, and becomes airborne dust. The airborne aluminum oxide powder is also hazardous. Extreme caution is required to avoid inhalation

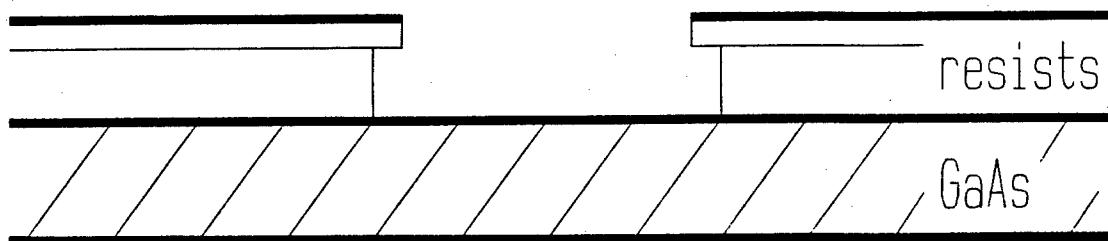


Figure 2.8 Develop second layer of photoresist

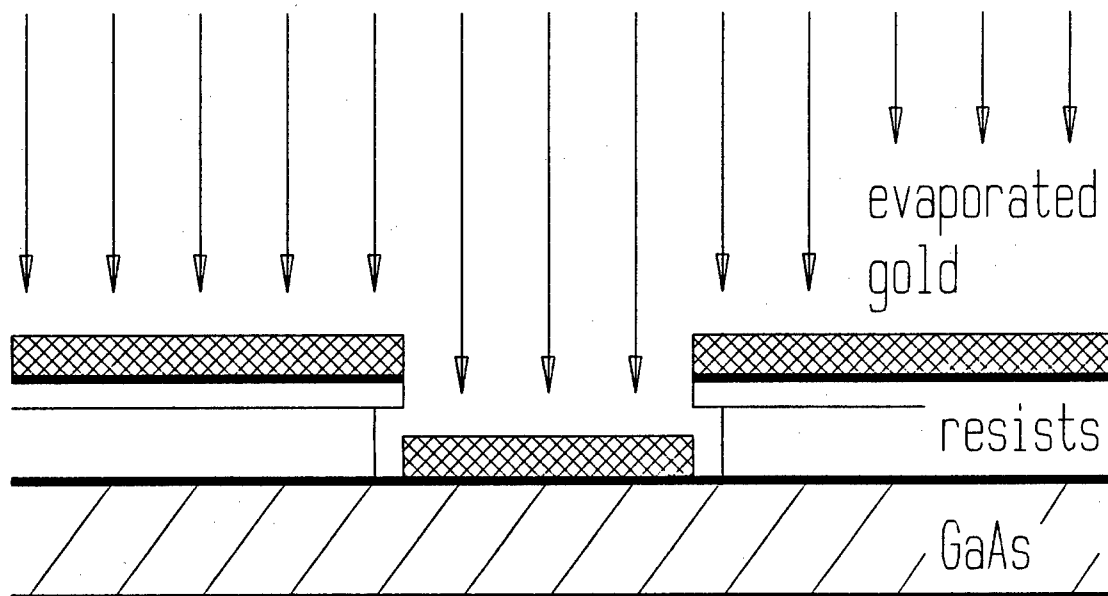


Figure 2.9 Evaporate titanium and gold metal layers

of this material. In short, this procedure is fraught with peril.

Table 2.6 gives the steps. Figure 2.13 and Table 2.7 show the measured thicknesses of the wafers which survived to this point.

2.3.5 Vias – third mask level

Vias are another fabrication step which is dangerous to the wafer;

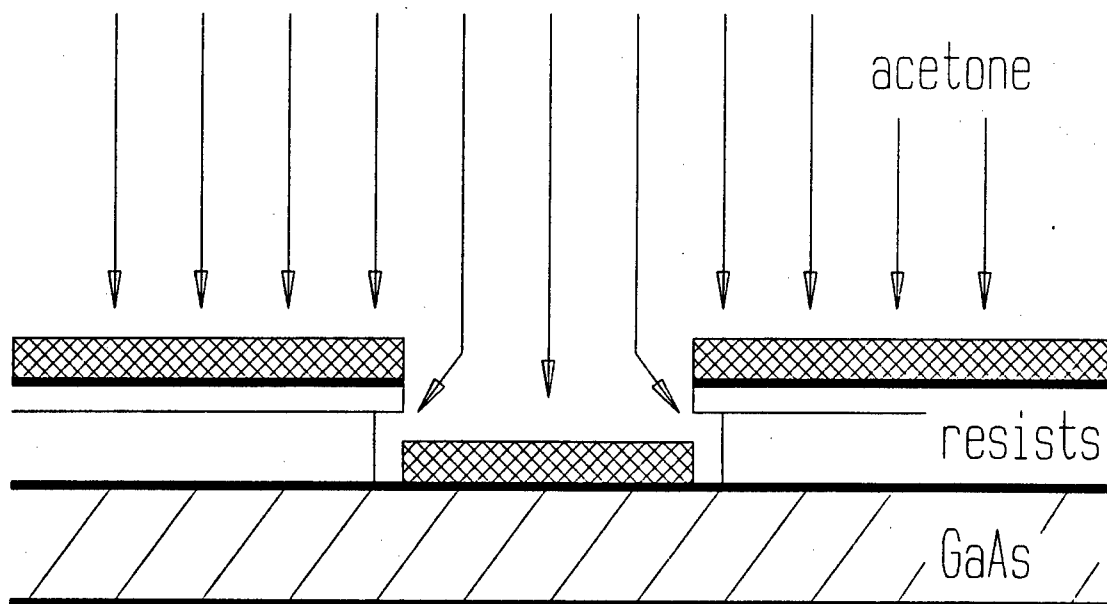


Figure 2.10 Liftoff unwanted metal with acetone

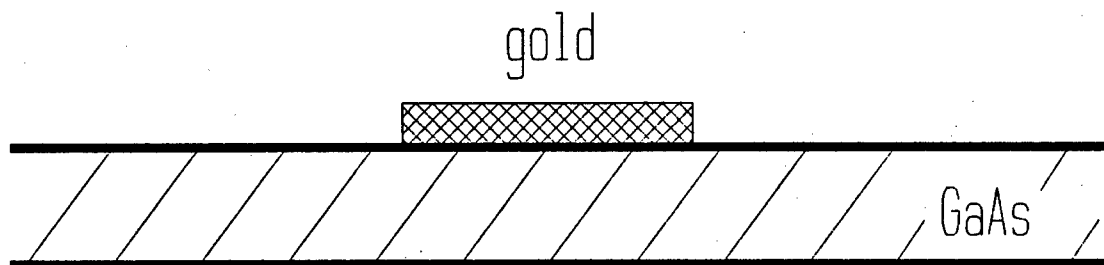


Figure 2.11 Finished structure with vertical edge

it is easy to misalign the via holes and coplanar transition pads, and it is easy to overetch. This step requires the handling of hot sulfuric acid, so it is dangerous to the operator as well. Table 2.7 lists the process steps, and Figures 2.14 through 2.17 show them in some detail. There are no alignment marks on these masks (in hindsight, there should have been) because alignment was

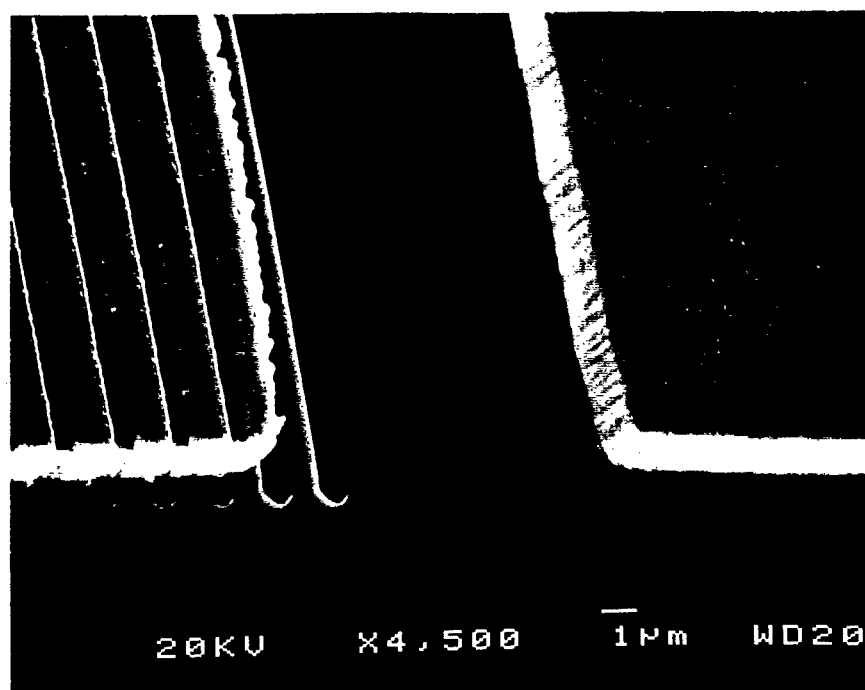


Figure 2.12 Vertical gold edge formed with lift-off process

Table 2.6 Wafer thinning steps

Lapping and Polishing

Complete wafer mounting with vacuum chuck

Lap wafer to $125\ \mu$ with $5\ \mu$ aluminum oxide/DI water slurry

Polish wafer to $100\ \mu \pm 3\ \mu$ tolerance with $0.3\ \mu$

aluminum oxide/DI water/Chlorox slurry

accomplished by centering holes within the transition pads. The use of a mask aligner with infrared capability was required so that alignment between the top and bottom of the wafer could be realized.

Figure 2.18 shows a pair of etched via holes underneath a coplanar transition. Figure 2.19 shows a pair of via holes from the bottom side after

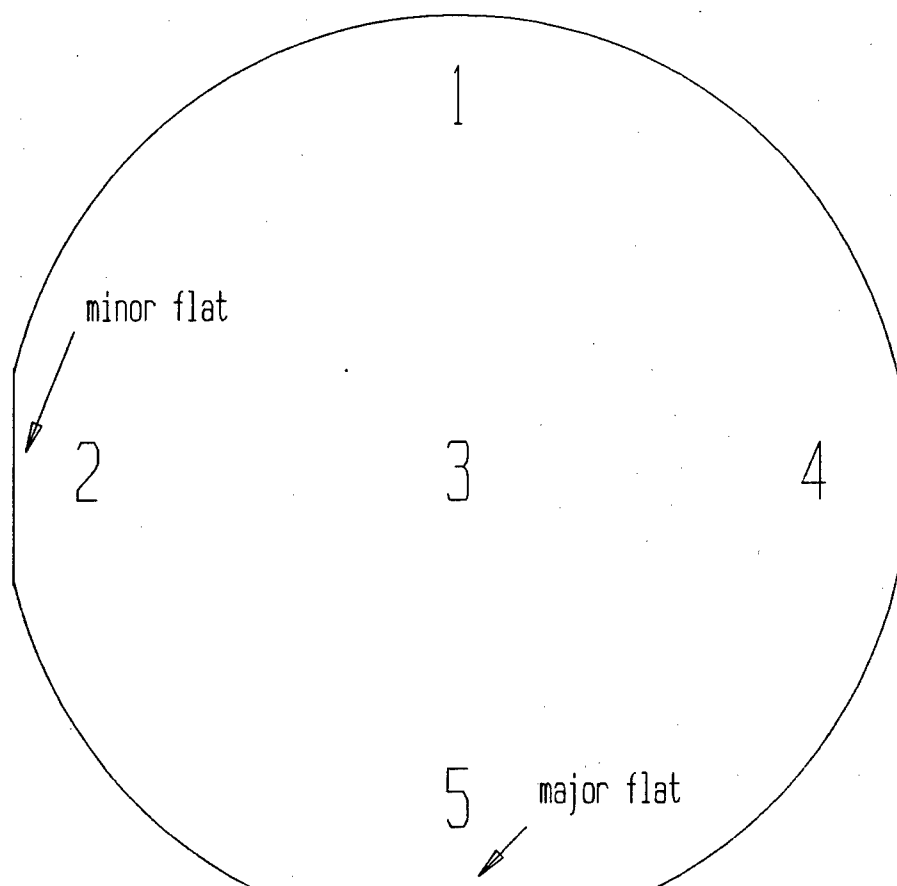


Figure 2.13 Locations for wafer thickness measurements

the thick gold ground plane has been electroplated on. Figure 2.2 earlier in this chapter shows the cross section of this transition, and it gives diameters for the tops and bottoms of the via holes. These numbers are very close to the numbers in the photograph; also the slightly convex cone shape of the vias shown in Figure 2.2 is characteristic of the chemical etch. If extreme care and close monitoring are exercised, very good and repeatable via holes are obtainable. This step, though, depends very much on the previous thinning step. If the wafer is not of a very uniform thickness (here, "very uniform" means that the wafer thickness h varies no more than about $\pm 3 \mu$), then the via hole diameters

Table 2.7 Measured wafer and ground plane thicknesses
(microns)

<u>Wafer</u>	<u>Site 1</u>	<u>Site 2</u>	<u>Site 3</u>	<u>Site 4</u>	<u>Site 5</u>	<u>Ground Plane</u>
1	108	104	114	105	101	5
3	115	109	117	113	111	-
4	106	107	111	102	107	7
5	112	108	116	101	105	7
6	103	104	112	105	099	5
7	097	097	110	103	099	5
8	095	095	101	093	095	7
9	094	092	103	100	100	6
10	112	113	116	103	106	6
12	103	106	112	108	104	5
13	103	104	112	098	104	4
14	108	105	115	110	110	6
15	105	100	107	103	097	6

will be very nonuniform across the wafer. When the etchant breaks through the last little bit of GaAs near the end of the etch, the hole diameter increases very rapidly. If the wafer is nonuniform, then some holes will have broken through and grown very large while others have not yet broken through. Thus if the wafer is very nonuniform, some holes can overetch and become larger than their transition pads, while others have not yet made a good enough breakthrough to ensure a good pad-to-ground plane contact when the back metal is put on.

The comments in Table 2.7 about keeping the wafer wet are very important. If the wafer dries out partially, air bubbles can form inside the

Table 2.8 Via hole lithography and etching steps

Via Hole Lithography

Clean wafer with acetone, methanol, isopropyl, DI 30 sec
 Bake at 100°C for 6 min on hot plate
 O₂ plasma etch 10 min
 Etch BOE:H₂O 1:1 for 30 sec
 DI rinse 30 sec
 Deposit 3000 Å Si₃N₄ at 100°C
 Clean wafer with acetone, methanol, isopropyl, DI 30 sec
 Bake at 100°C for 6 min on hot plate
 Spin on Waycoat Type 3IC negative resist at 3000 rpm for 30 sec
 Bake at 70°C for 20 min in convection oven
 Visually inspect photoresist
 Expose mask (vias) 405 nm UV 18 sec (align via holes
 to pad centers)
 Develop xylene 15 sec
 Rinse n-butyl acetate 10 sec
 Rinse isopropyl 20 sec; blow dry
 Visually inspect via pattern
 O₂ plasma etch 10 min (descum)
 Etch BOE:H₂O 1:1 for 30 sec
 DI rinse 30 sec
 Visually inspect etched windows in Si₃N₄
 Strip photoresist with Losolin remover at low boil
 DI rinse

Via Hole Etch

NOTE: etchant solution is 3:1:1 H₂SO₄ : H₂O₂ : H₂O

Pour water into beaker
 Slowly add sulfuric acid to same beaker
 Place beaker into circulating temperature bath: heat to 60°C
 Add peroxide to beaker
 Wait 15 min, then slowly place wafer into etchant with Teflon holder
 Check wafer every 30 min until holes are almost through. Keep the
 wafer wet throughout the process. Do this by lifting the
 wafer from the etchant, rinsing in a beaker of DI water,
 and putting the wafer into a petri dish of DI water.
 When holes are almost through, let the etchant sit in the bath for
 15 min to reduce its strength
 Resume etching. Check wafer every 5 min until finished

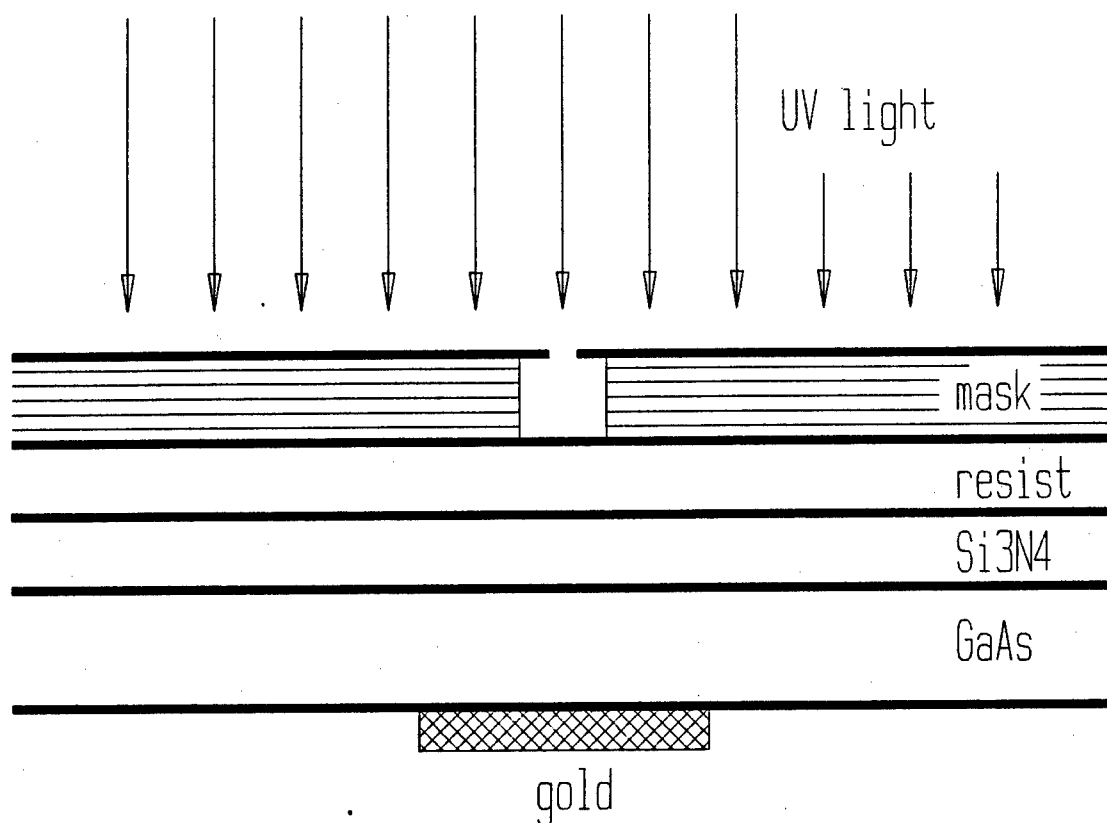


Figure 2.14 Expose via hole mask to photoresist layer on backside

etching via holes. The surface tension of these bubbles will keep the etchant from making contact with the GaAs surface, and the etch rate of such a via hole will drop drastically. Either the hole will become asymmetrical, or it will not be etched all the way through. Of course, during the etching process the silicon nitride is being etched also. Silicon nitride is resistant – not impervious – to the sulfuric acid etch, so lengthy periods in the etchant will tend to remove the silicon nitride mask and to make the via hole bases very large. Many variables, including concentration, temperature, and relative proportions of the etchant constituents, as well as the time history of the solution, affect the etch rate. Cleanliness of the wafer and the exposed surface area also affect etch rate. The etching process must be monitored very carefully.

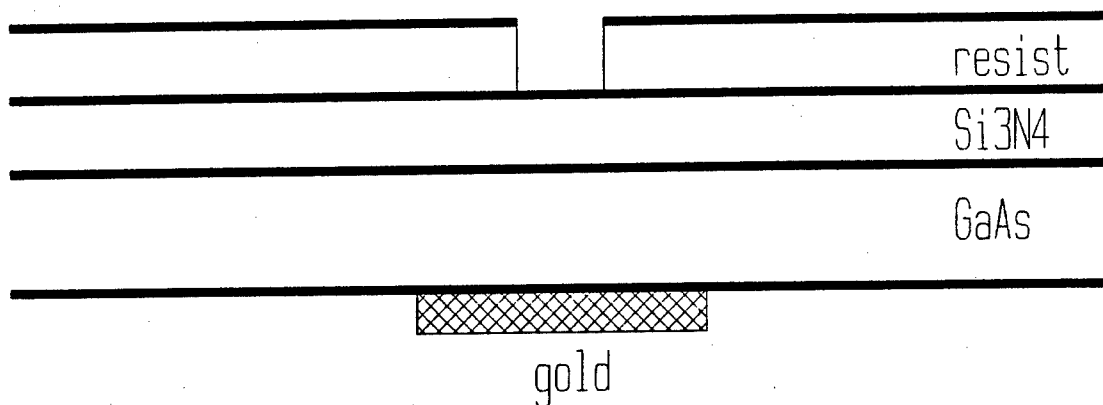


Figure 2.15 Develop photoresist

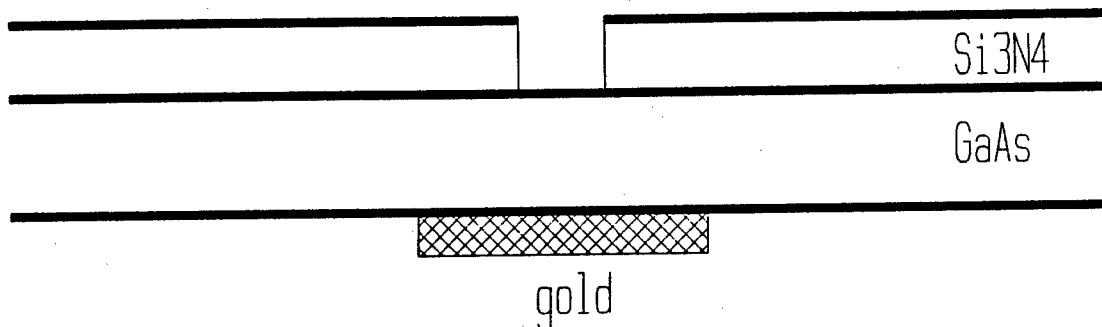


Figure 2.16 Etch silicon nitride "mask" layer and strip photoresist

2.3.6 Back metallization and demounting

These are the final processing steps. It is also dangerous to the wafer (actually, all processing is dangerous to GaAs because it is so fragile!). Care should be taken when electroplating the ground plane that sharp points on the alligator clip do not clamp too hard on the wafer. These sharp points can initiate cracks that propagate freely along the wafer's cleavage planes when the

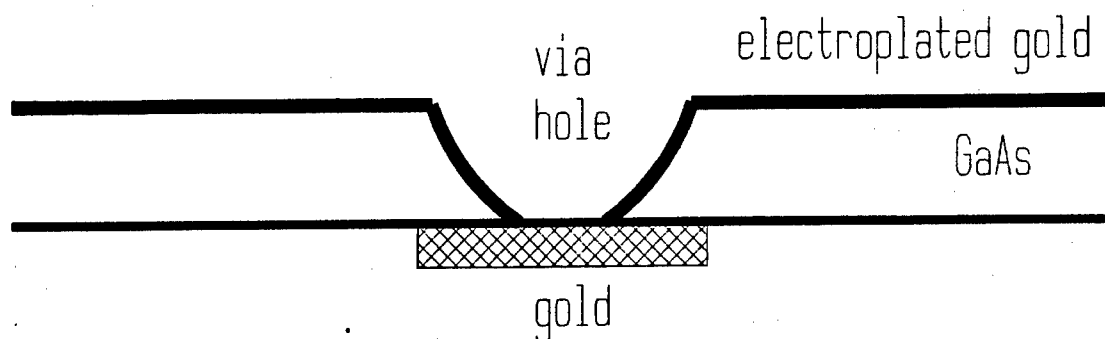


Figure 2.17 Etch via holes, evaporate gold seed layer, and electroplate gold ground plane

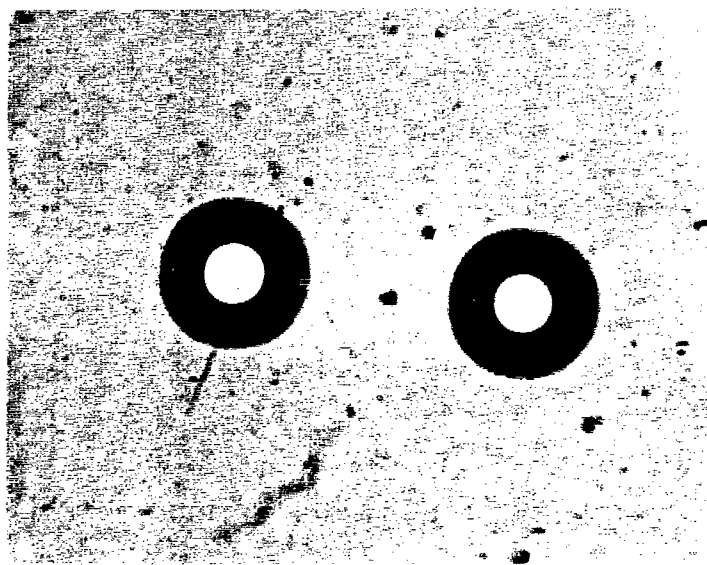


Figure 2.18 Freshly etched via holes

wafer is removed from the glass disk.

Demounting is perhaps the most stressful step of all. If the wafer is still whole at this point, then it has already been subjected to nontrivial stresses. It is at its thinnest and most fragile. If not for the relatively thick

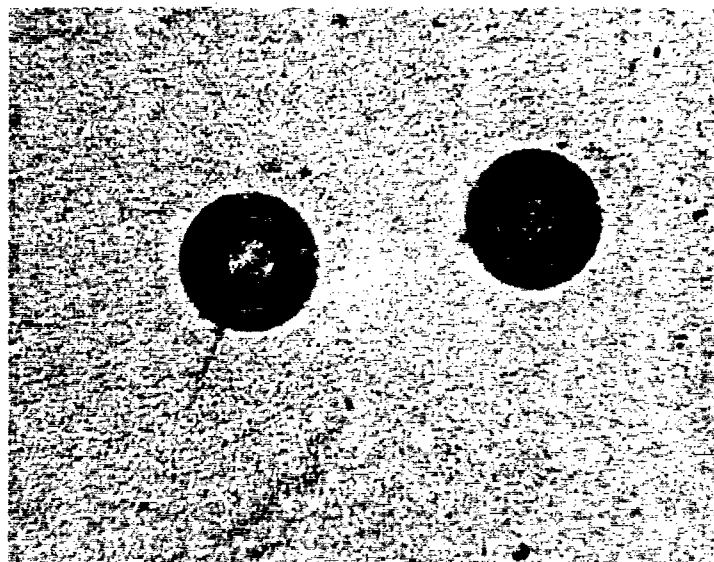


Figure 2.19 Via holes with electroplated ground plane

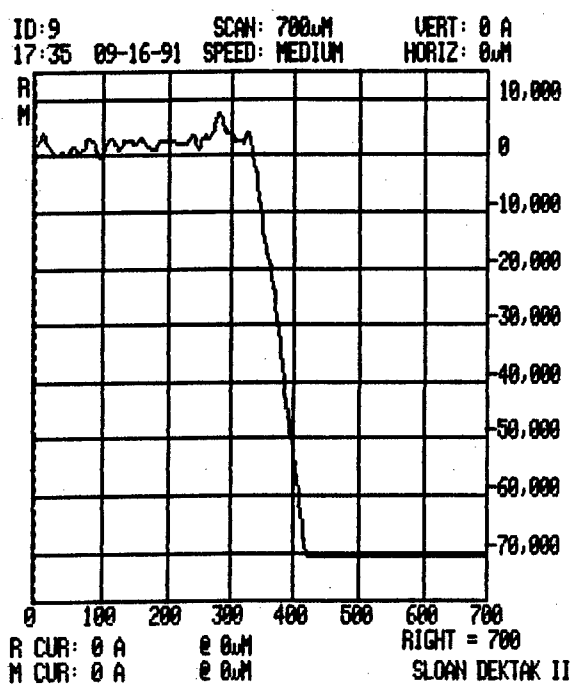


Figure 2.20 Dektak plot of electroplated gold ground plane thickness of 7μ for Wafer 8

gold ground plane to lend it support, the wafer would probably not survive being removed from the glass disk. The way this demounting is performed at Wright-Patterson is somewhat subject to individual preference and creativity, but the way I performed it was to place the wafer (glass disk side down) onto the hot plate and to have a towelette rated for clean room use nearby. As the wafer heated up and the wax softened (about fifteen seconds or so), I used a pair of forceps to push the wafer off the disk and onto the towelette, using another pair of forceps to keep the glass disk stationary. The difficulties with this process are that the wafer may break (the object is to apply all force parallel to the wafer, not normal to it) and that the wafer may adhere to the towelette if the wax is still soft by the time the wafer gets there. A safer, more reliable way to demount wafers definitely needs to be developed.

Table 2.8 lists the relatively simple, but difficult to perform, process steps. Figure 2.20 shows a Dektak plot verifying the thickness of one of the wafer's ground planes; this is Wafer 8 with a thickness of about 7μ . The left side of the plot is the gold ground plane, and the very flat area on the right is the GaAs wafer surface; this type of plot is made with the wafer upside down. This plot also discloses the magnitude and character of the surface roughness of electroplated gold. Note that the roughness, though, is on the side of the conductor away from the substrate. Since a seed layer of gold was evaporated onto an optically flat surface before electroplating, the substrate to ground plane interface is very smooth.

Table 2.9 Back metallization and demounting steps

Back Metallization

Coat visible portion of glass disk with 1400-27 photoresist

Evaporate 200Å titanium on back

Evaporate 1000Å gold on back

Electroplate 5 to 7 μ gold on back

Mounting

Heat wafer on hot plate at 200°C until wafer detaches from disk

Clean wafer in petri dishes with trichloroethylene, acetone, methanol, isopropyl, and DI water. Allow to air dry.

Spin on wax at 2500 rpm for 30 sec on silicon wafer

Put silicon wafer on hot plate at 200°C; place GaAs wafer on it

Clean any remaining residue from wafer on spinner

CHAPTER III

LOSS MEASUREMENT METHODOLOGY

There are two primary methods for measuring loss, and there are several sources of error associated with these two methods. But before loss measurements can be made, the measurement system (typically an automatic vector network analyzer such as the Hewlett-Packard 8510B) must be calibrated. In the chapter we explore calibration, loss measurement methods, potential sources of error, and relationships among these topics.

3.1 Thru-reflect-line (TRL) calibration

3.1.1 What is calibration?

Calibration is the technique of measuring standards whose behaviors are well known and using the system's responses to remove the effects of systematic errors in the measurement system [20-21].

Within the context of a vector network analyzer (VNA), a "perfect" network analyzer is assumed (Figure 3.1). The effects of the connectors or transitions, intervening cable, and differences among the two ports are lumped into the two-port networks labelled "error boxes" (all calibrations discussed here will be understood implicitly to be two-port calibrations). Not shown in the figure are two other important corrections: the switch terms and the leakage terms. Leakage (or isolation) is whatever signal gets from one port to the other when both ports are terminated in a matched load. The switch (or directivity) terms arise from the fact that within the "perfect network analyzer" box, there

are two reflectometers (one per port). These reflectometers are switched to measure forward and reflected power, but the switches are not matched exactly. The switch terms account for the mismatch between these switches. All these terms taken together (four for the S-parameters in each error box, two for the switching terms, and two for the leakage terms) constitute the twelve-term error model used in the HP 8510B VNA (also used in other models). The error box model can be reduced to the eight-term error model if the switch terms are "ratioed out", and isolation is either omitted or taken care of separately [20].

Calibrations differ in the types and number of standards used to deduce these error terms. The usual method used for coaxial media with the 8510 is OSLT (open-short-load-thru); this is an undesirable technique for microstrip because it is very difficult to make short circuits and accurate matched loads in microstrip. The calibration method used in this research is TRL (thru-reflect-line).

3.1.2 TRL calibration and standards

TRL calibration [20-33] is an attractive technique for microstrip media because the standards required are a thru (may be of nonzero length), a reflect (may be a short or an open), and a line (length depends on the frequency over which the calibration is to be performed). Moreover, the reflect standard does not have to be perfect. This is the traditional TRL calibration which is implemented in the HP 8510B VNA. For microstrip a thru, an open, and a line are ideal; these standards are easy to implement in this medium. Moreover, another advantage to this method is that the standards are in the same medium (that is, the standards have the same characteristic impedance Z_0 and propagation constant γ as the device under test (DUT)). Finally, a great convenience is that, since eight error terms are needed but ten are actually measured (four for the thru, four for the line, and two from the reflects), two more unknowns

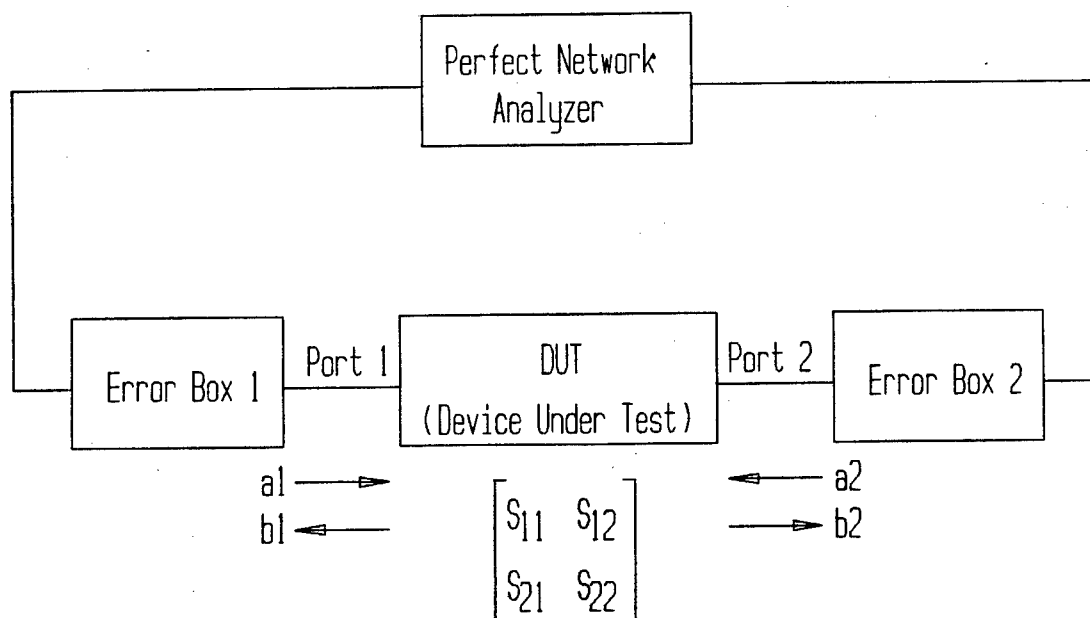


Figure 3.1 Partitioning of a real network analyzer system into a perfect network analyzer, error boxes, and the device under test (DUT)

can be determined. These two unknowns are taken to be the actual reflection coefficient Γ_L of the reflect (useful to determine the open-circuit fringing capacitance of a microstrip open circuit) and the actual propagation constant γ of the line (from which ϵ_{re} can be determined). Since the line's attenuation α is the desired parameter in this research, this approach is extremely attractive.

The general derivation of the TRL calibration will be presented here [26]. This treatment makes use of transmission matrices (also known as R matrices), which may be cascaded. First the S matrix $[S_{AB}]$ of the thru is measured; it is converted to the equivalent R matrix. If each connector's effects are isolated to their respective ports, then this thru can be thought of as two cascaded R matrices, A and B , each of which contain their respective connector

(transition) effects. Note that

$$[R_{AB}] = [R_A] \cdot [R_B] \quad (3.1)$$

since these are transmission matrices.

Next the line is connected and its S matrix $[S_{ALB}]$ is measured. This is the same as $[S_{AB}]$ above, with an added length of line between the A and B matrices. $[S_{ALB}]$ is converted to $[R_{ALB}]$, noting that

$$[R_{ALB}] = [R_A] \cdot [R_L] \cdot [R_B] \quad (3.2)$$

These two standards alone provide enough information to obtain the frequency- dependent propagation constant of the transmission line in which calibration is being performed. To do so, first consider the matrix

$$[T] = [R_{ALB}] \cdot [R_{AB}]^{-1} \quad (3.3)$$

T is fully known since it is calculated from the R matrices, and hence the measured S matrices, of the line and thru.

Equation (3.3) can be expanded into

$$[T] = [R_A] \cdot [R_L] \cdot [R_B] \cdot [R_B]^{-1} \cdot [R_A]^{-1} = [R_A] \cdot [R_L] \cdot [R_A]^{-1} \quad (3.4)$$

The transmission matrix of the added length L of the line can be written:

$$[R_L] = \begin{bmatrix} e^{-\gamma L} & 0 \\ 0 & e^{-\gamma L} \end{bmatrix} \quad (3.5)$$

since the line has propagation constant $\gamma = \alpha + j\beta$. Postmultiplying (3.4) by $[R_A]$ gives

$$[T] \cdot [R_A] = [R_A] \cdot [R_L] \quad (3.6)$$

which can be expanded to

$$\begin{bmatrix} T_1 & T_2 \\ T_3 & T_4 \end{bmatrix} \cdot \begin{bmatrix} R_{A1} & R_{A2} \\ R_{A3} & R_{A4} \end{bmatrix} = \begin{bmatrix} R_{A1} & R_{A2} \\ R_{A3} & R_{A4} \end{bmatrix} \cdot \begin{bmatrix} e^{-\gamma L} & 0 \\ 0 & e^{-\gamma L} \end{bmatrix} \quad (3.7)$$

Expanding these matrices gives four equations; eliminating some unknowns gives

$$\epsilon^{2\gamma L} - \epsilon^{\gamma L}(T_1 + T_4) + (T_1 T_4 - T_2 T_3) = 0; \quad (3.8)$$

this complex equation has 2 solutions. Setting $\epsilon^{\gamma L}$ equal to G ; we can write the solution to (3.8) as

$$G = B[1 \pm \sqrt{D}] \quad (3.9)$$

The two quantities represented by Equation (3.9) are $|G_1|e^{j \arg_1}$ and $|G_2|e^{j \arg_2}$; they are found from

$$G = \left(\frac{T_1 + T_4}{2} \right) \left[1 \pm \sqrt{1 - \frac{T_1 T_4 - T_2 T_3}{\left(\frac{T_1 + T_4}{2} \right)^2}} \right] \quad (3.10)$$

The proper solution is indicated by whichever \arg_i is negative. This insures that the phase constant has the proper sign.

Now the attenuation per unit length in dB/cm is

$$\alpha = \frac{20 \log_{10} |\epsilon^{\gamma L}|}{L(\text{cm})} \quad (3.11)$$

The effective dielectric constant ϵ_{re} is also determined from

$$\beta L = \arg = \frac{2\pi L f \sqrt{\epsilon_{re}}}{c} \quad (3.12)$$

so

$$\epsilon_{re} = \left[\frac{30 \arg}{2\pi L(\text{cm}) f(\text{GHz})} \right]^2 \quad (3.13)$$

The propagation constant of the line is the desired parameter in this research, so we will not discuss the derivation of the reflect standard's actual reflection coefficient Γ_L in detail. The procedure is to measure identical though unknown and possibly fairly poor reflections on ports 1 and 2. It is necessary to know if the reflect is an approximate open or an approximate short circuit; this resolves the ambiguity in finding the correct phase angle of the measured

reflection standard's Γ_L .

Also, if so desired, depending upon the length of line in which the DUT is embedded from the reference plane, be it positive (extra line) or negative (shorter line), the DUT's measured S-parameters may be de-embedded [26]. This simply means that the effects of the extra (positive or negative) length of line are removed from the DUT's measured S-parameters, and this is possible because we know both the physical length of line in which the DUT is embedded, as well as the propagation constant of said line. This additional effort was not required in this research, but is fairly simple to accomplish.

Now that we have the calibration method in hand, we need to examine standard selection. First, though, a word about the reference plane. The wafer probe is an intrusive device which perturbs the quasi-TEM mode fields near the transition; for that matter, the transition itself is a perturbation. For this reason it is recommended that the reference plane be located far enough away from the probe tips or transition (whichever is nearer the reference plane) that the evanescent fields have died out. Numerical experiments [34] indicate that about $200\ \mu$ should be sufficient; this is about 2 substrate heights. The setup on these wafers puts the reference plane $500\ \mu$ ($5h$) away from the transition; this is half the physical length of the non-zero-length thru ($1000\ \mu$).

Either the thru or the reflect can be used to determine the reference plane, but I have found it more convenient to use the thru. It is slightly more intuitive, and it is easier to keep track of when probing to look at the thru standard and note that the reference plane is half of its length. The reflect can extend past the reference plane, but if it extends a quarter-wavelength, then the open looks like a short, so it is usually better to let the open be at or very slightly past the reference plane. It is also useful to have a pair of reflects facing each other so that their measurement can be made simultaneously on

both ports. MMIC fabrication technology is sufficiently advanced that the two reflects will be essentially identical; more attention should, in fact, be focussed on making identical microwave wafer probe contacts.

With the thru and reflect seen to, only the line remains. It is here that confusion is most likely to arise, though the only parameter left to vary is the line length. TRL requires that the difference in line length between the thru and line be nearly an odd multiple of a quarter-wavelength, with an exact quarter-wave being optimal. This points out perhaps the strongest disadvantage to using TRL: that is, it is an inherently narrowband technique. OSLT can be made to cover the entire 100 MHz to 40 GHz band, but TRL suffers from a bandwidth limitation. If the line length difference approaches a multiple of a half-wavelength, then there is an ambiguity that cannot be resolved. It is known from transmission line theory that adding an additional half-wavelength of line to a transmission line (with the same Z_o , of course) does not change the line any, except for the additional loss. Therefore the measurement of the thru and the line appear identical (except for the aforementioned additional loss), and an additional standard will still be required. The normal criterion for selecting the line standard's length is that the difference in electrical length between the line and the thru must not approach within 20° of a multiple of a half-wavelength. That is, the difference in phase must remain between 20° and 160° , or between 200° and 340° , and so on. Of course, very long lines get unwieldy in terms of substrate area required and maintainability of uniformity. The two equations used for calculating the standard's electrical length are:

$$\Delta\phi(\text{deg}) = \frac{360^\circ \cdot f \cdot \Delta l}{c \sqrt{\epsilon_{re}}} \quad (3.14)$$

and

$$\text{delay (sec)} = \frac{\Delta l}{c} \sqrt{\epsilon_{re}} \quad (3.15)$$

where f is the frequency at the upper or lower end of the band. Δl is the difference in physical length, and c is the speed of light. Equation (3.14) is necessary, of course, to check that the electrical length difference requirement is not violated, and this requirement must hold across the entire frequency band. This means that TRL is restricted to an 8:1 bandwidth, unless several lines are used and then the areas joined after calibration. This method is notorious, however, for producing jump discontinuities at the joined band ends, and is not used in this research. The 6 GHz to 40 GHz band is less than 8:1. Equation (3.15) is required because the HP 8510B expects the standard definitions to be given in terms of electrical delay rather than electrical phase difference. Note that specifying a TRL line standard requires that a fairly accurate calculation of that line's effective relative dielectric constant be performed. After all, there is no other way to determine a line's electrical length beforehand.

Before we progress, I must note that single-thru TRL calibration gives a fairly noisy measurement of α ; after all, "good" transmission lines are low-loss. In addition, I needed to resolve fairly small changes in α due to the addition of grooves of different orientations. If the noise in the extraction of α were greater than the desired changes in α , it would be exceedingly difficult to make good, meaningful measurements without, perhaps, resorting to sophisticated statistical methods based on the characteristics of the desired measurements and the noise. But a solution exists.

3.1.3 NIST multi-line TRL calibration

Dylan Williams and Roger Marks at the National Institute of Standards and Technology (NIST) have developed a very valuable extension to the TRL calibration method; it is referred to as multi-line TRL [35-37]. It allows the use of multiple lines to improve calibration accuracy and bandwidth. Using a linearized error analysis of the TRL calibration method, they arrived at

optimal, minimum-variance estimates of the calibration constants. This statistical treatment allows great increase in the accuracy of the extraction of the line's propagation constant. It is interesting that, in their method, using lossy lines *improves* the calibration accuracy. Normally, as the difference in length between the thru and line approaches a multiple of a half-wavelength, the linear error term becomes infinite for a lossless line as its denominator becomes infinite. The denominator is the magnitude of the sine of the phase difference. If the line is lossy, the error term is less because the denominator is the sine of a complex number, and it is never zero; thus its inverse is never infinite. This effect is examined quantitatively in [36].

A noteworthy requirement is that one of the extra lines be very long, say an order of magnitude longer than the others. This greatly increases the effects of the line's loss. After performing several on-wafer calibration experiments with different combinations of lines (up to four short ones and one very long one), that using all lines provided an order of magnitude less noisy extraction of α than the normal, single-line TRL calibration. Leaving out a single of the short lines degraded the noise slightly; leaving out two degraded it much more noticeably. Using the four short lines but leaving out the long line was almost as bad as the single-line method. Therefore I can confirm their claim that more lines give better calibration, and that it is desirable to have one very long line.

I must state here that I (along with the rest of the microwave measurement community) am greatly indebted to their extension of the TRL calibration technique, and that I do not think I could have made these measurements without it. Certainly they would be much more noisy, the standard deviations for several averaged sets of measurements would be much larger, and the noted increases in loss due to surface roughness would be much more uncertain.

3.1.4 Sources of error

The following are widely recognized sources of error in on-wafer measurements [38]:

1. Degraded Probes and Standards
2. Deviations in Standards
 - Substrate thickness
 - Via hole size
3. Repeatability
 - Position (x and y)
 - Pressure (z)
 - Angle (rotation of probe in xy plane)

These items will now be addressed individually.

Degraded probes and standards result after repeated contacts by the wafer probes. The gold on the transitions gets rubbed off and even smeared; it is a very ductile metal. The gold on the wafer probe tips also gets worn. This wear results in slight differences among individual connections to the same standard (or DUT, for that matter).

There will almost certainly be deviations in the standards; even with careful, individual attention to fabrication, there will be differences from wafer to wafer and even across the same wafer. The most noticeable difference is in substrate thickness, and this is most of the cause of the difference in via hole size. Due to the imperfect nature of the mechanical grinding and polishing process, there will almost always be a variation of height h across the two-inch-diameter wafer. Usually this will be about $\pm 5 \mu$; sometimes it is a little better, and sometimes worse. At least it was measured, if not controlled; little can be done to control this variation. It is directly dependent on the quality of grinding that can be accomplished with the equipment used. This variation in

h will affect the diameter of the via holes; as they break through to the top side, the diameter etch rate increases dramatically. This is because the acid has ceased to go through the wafer and can now begin removing the thin material at the edge of the newly-formed hole. If the via holes are drastically different from standard to standard, then the condition of identical connectors is violated. Fortunately there can be a moderate amount of difference in via hole diameter without changing via hole inductance very much. But the more serious effect is the change in the propagation constant. If h varies, then all the lines are not identical anymore. Furthermore, h can vary by 5% or so down the length of a very long line; it is not clear what effect using a nonuniform transmission line as a standard has on TRL or multiline TRL calibration: this topic should be investigated further.

Assuming that probe tip and transition erosion and substrate thickness variation can be controlled, then repeatability is the remaining factor, and it is operator dependent. Due to the nature of the chuck and 3-axis probe head micrometer, there can be placement errors in planar (xy) placement, vertical z placement, and rotational θ alignment. It is fairly easy to repeatably place the probe tips in x , y , and θ , but z is a bit more difficult; Appendix B deals with this issue in more detail. One uses relative positioning of the probe tips on the transition for x , y , and θ , but z requires judging the degree of focus of the probe tip and transition, and the amount of lateral movement due to the probe tip contacting the substrate. Errors in z affect the measured $|S_{21}|$; increased contact pressure reduces the apparent loss because a "better" contact is made. It is possible to crudely repeat contacts in z by interactively using $|S_{11}|$ and $|S_{22}|$ to get about the same level of reflection for each contact. We are measuring lines, which are supposedly matched; therefore small changes in the quality of contact show up very well as changes in the small reflection coefficients.

3.2 Extraction of loss from $|S_{21}|$ measurements on long lines

After carefully calibrating the measurement system on-wafer as described in the last section, α can be measured directly. Nothing more is involved than measuring $|S_{21}|$, changing the sign, and dividing by the line length; this gives loss in dB/cm (assuming $|S_{21}|$ is in dB). This result is true because, for a lossless line, $|S_{21}| = 0$ dB. On the logarithmic scale, any loss will show up as a negative transmission coefficient. This number is, by definition, the loss of the line. All of the data labelled as loss from direct measurement of lines in this dissertation was treated this way. Also, since most of the lines were measured several times, a sample standard deviation could be calculated for these lines as a function of frequency.

3.3 Extraction of loss from two-port gap-coupled resonator measurement

3.3.1 Extraction of loss from resonator parameters

The classic extraction of attenuation constant from measurements of two-port gap-coupled resonators is widely [5] used to measure loss of microstrip transmission lines. Beginning with the definition of resonator Q as $\frac{\omega_0 U}{W}$, where U is the stored energy and W is the power lost per cycle, and taking a distributed circuit model of the transmission line composing the resonator, it can be shown [5] that

$$Q = \frac{\beta}{2\alpha}, \quad (3.16)$$

where β is the phase constant of the line and α is the attenuation constant. Since β is also equal to $2\pi/\lambda_g$, we see that

$$\alpha = \frac{\pi}{Q\lambda_g} \text{ N/m} = \frac{8.686\pi}{Q\lambda_g} \text{ dB/m} \quad (3.17)$$

where $\lambda_g = \frac{c}{f\sqrt{\epsilon_{re}}}$ is the guide wavelength. This equation lumps all the losses

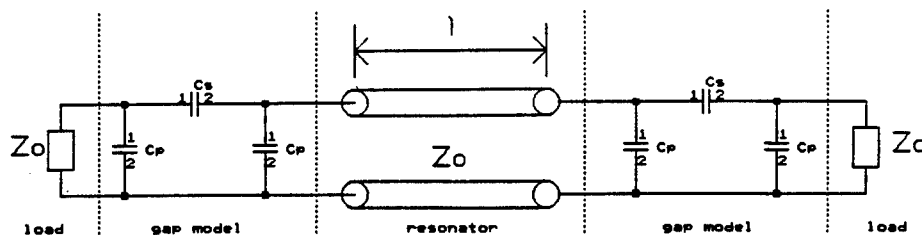


Figure 3.2 Standard transmission line model of a two-port gap-coupled resonator

together for the resonator, including the dielectric and radiation losses. We stated that the substrates used in this research are "good" dielectrics; just how good are they? We invoke the often-used expression for the portion of the attenuation constant due to the lossy dielectric [5]:

$$\alpha_d = 27.3 \frac{\epsilon_r (\epsilon_r - 1)}{\epsilon_{re} (\epsilon_r - 1) \lambda_o} \tan \delta \quad \text{dB/unit length} \quad (3.18)$$

where $\tan \delta$ is the loss tangent for the substrate material. GaAs has a loss tangent of about 0.0006 [12]. Since λ_o is in the denominator of Equation (3.18), α_d will be maximized when λ_o is minimized, or f_o is maximized. So, for the dielectric used in this research, the portion of the attenuation constant due to the dielectric at (say) 35 GHz will be about 0.053 dB/cm. Looking ahead, we see that at 35 GHz, the measured loss of a smooth strip is about 0.8 dB/cm. So about 6.5% or so of the measured loss of a smooth resonator will be due to the dielectric loss. At 8 GHz, the dielectric attenuation is about 0.012 dB/cm, whereas the strip loss is 0.37 dB/cm; therefore at lower frequencies only about 3.3% of the resonator loss is due to the dielectric. These percentages are reasonable small. The best approach would have been to independently measure $\tan \delta$, but accurately making this measurement was not possible.

Figure 3.2 is the standard transmission line model of a two-port gap-coupled resonator. The gaps are represented here by equivalent capacitive pi-networks. It is necessary to maintain sufficient coupling to excite the resonator and to measure its response, but light enough coupling that the fifty-ohm loads presented by the network analyzer's ports do not unduly perturb the resonator. It is possible to use design formulas to compute the shunt and series capacitances for this network and to calculate losses from that, but it is much easier and also sufficient to use the very simple standard RLC resonant circuit model in Figure 3.3. The response of this circuit may be shown to be

$$|S_{21}(f)| = \frac{|S_{21}|_{max}}{\sqrt{1 + 4Q_o^2 \left(\frac{f_o - f}{f_o} \right)^2}} \quad (3.19)$$

where, as usual, f_o is the resonant frequency ($1/2\pi\sqrt{LC}$ in the circuit model) and Q_o is the unloaded Q . In practice, what is measured is the loaded Q , designated Q_l ; these two are related by the coupling coefficient k via

$$Q_o = Q_l(1 + k) \quad (3.20)$$

where the coupling coefficient is computed from

$$k = \frac{|S_{21}|_{max}}{1 - |S_{21}|_{max}} \quad (3.21)$$

These equations [39] were used to calculate the resonator losses given in Chapter 4.

3.3.2 Nonlinear curve fit to standard circuit model

Let us discuss the fit of the previously presented circuit model to the measured data. If there are too many second-order effects in the constructed resonators, then this is not a good model; we hope it is sufficient. To that end, let us quickly investigate the behaviors of the three parameters that can be

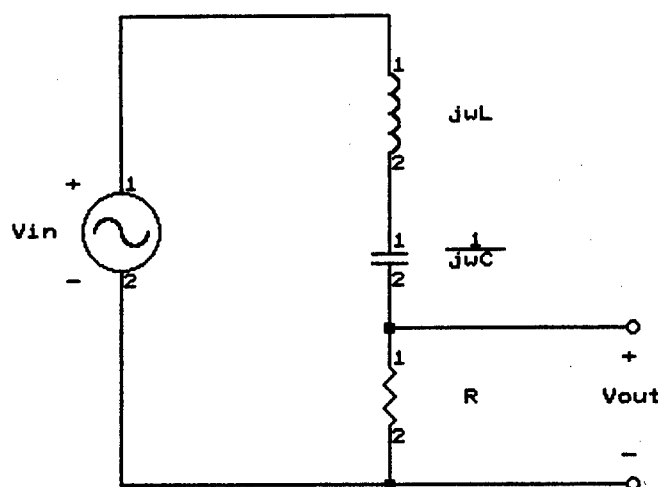


Figure 3.3 Standard series RLC circuit model for resonator

varied to fit the model to the data.

Figure 3.4 shows the effect of varying $|S_{21}|_{max}$ on the model's response; as expected, the curve is shifted vertically. Figure 3.5 shows the result of changing the resonant frequency f_0 ; again, as expected, the curve shifts horizontally. Finally, Figure 3.6 shows the effect of varying the parameter Q . This narrows or widens the graph, as one would surmise with f_0 and the maximum amplitude held constant.

Knowing that the standard RLC circuit model is a good model for resonators, the question is how well it models the behavior of the actual resonators measured in this research. Figures 3.7 and 3.8 are actual fitted data and the accompanying curves for what are qualitatively termed "poor" and "good" fits, respectively.

The "poor" fit is representative of the worst fit set of data taken, and the "good" fit is representative of the best fit set of data taken. As is usually

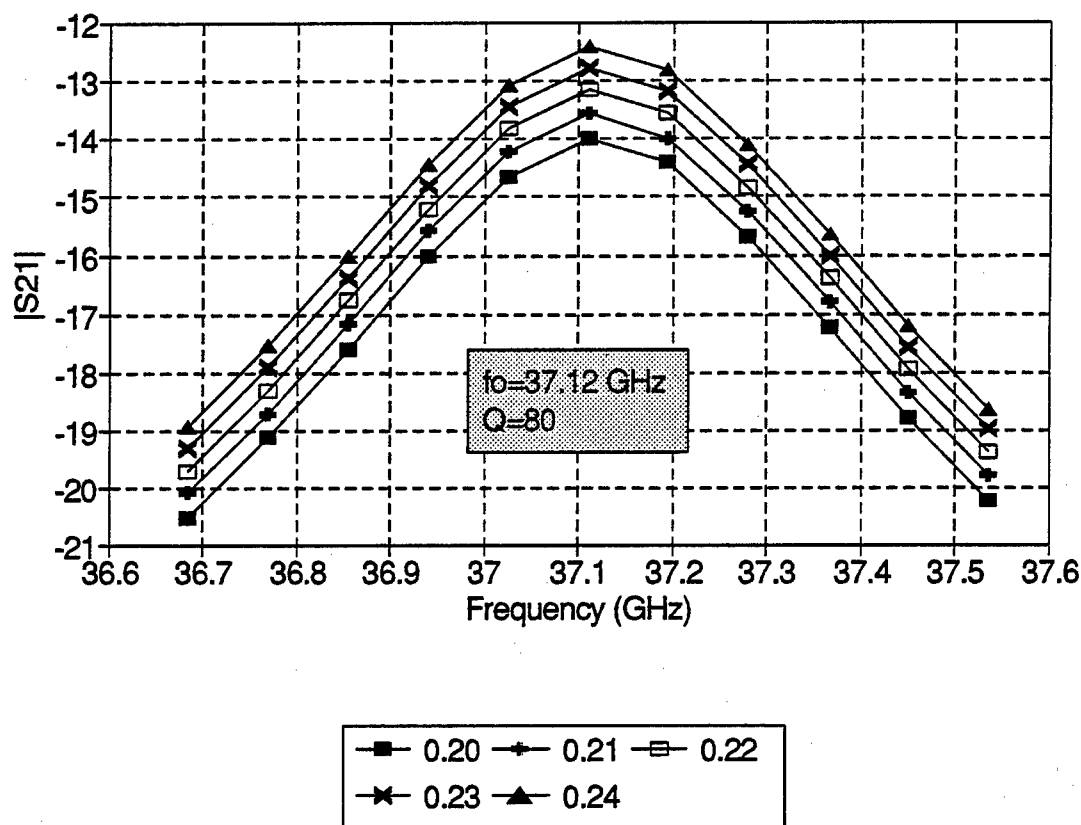


Figure 3.4 Effect of varying $|S_{21}|_{max}$ on the nonlinear curve fit

the case with this type of measurement, the “average” fit was somewhat in between these two extremes. Tables of the fitted parameters, along with their residuals, are presented in Chapter 4. One observation: for the “poor” fits, one side of the model was below the data, while the other side was above the data. This behavior was fairly consistent when the fit was “poor,” but the cause is unknown at this time. Also the term “poor” fit is relative. Very good agreement between the fitted model and the actual data was observed in every case but two out of 84. When the standard deviations were calculated, these two α 's were more than one standard deviation from the mean, so they were discarded and the means were calculated again without them, as is standard statistical

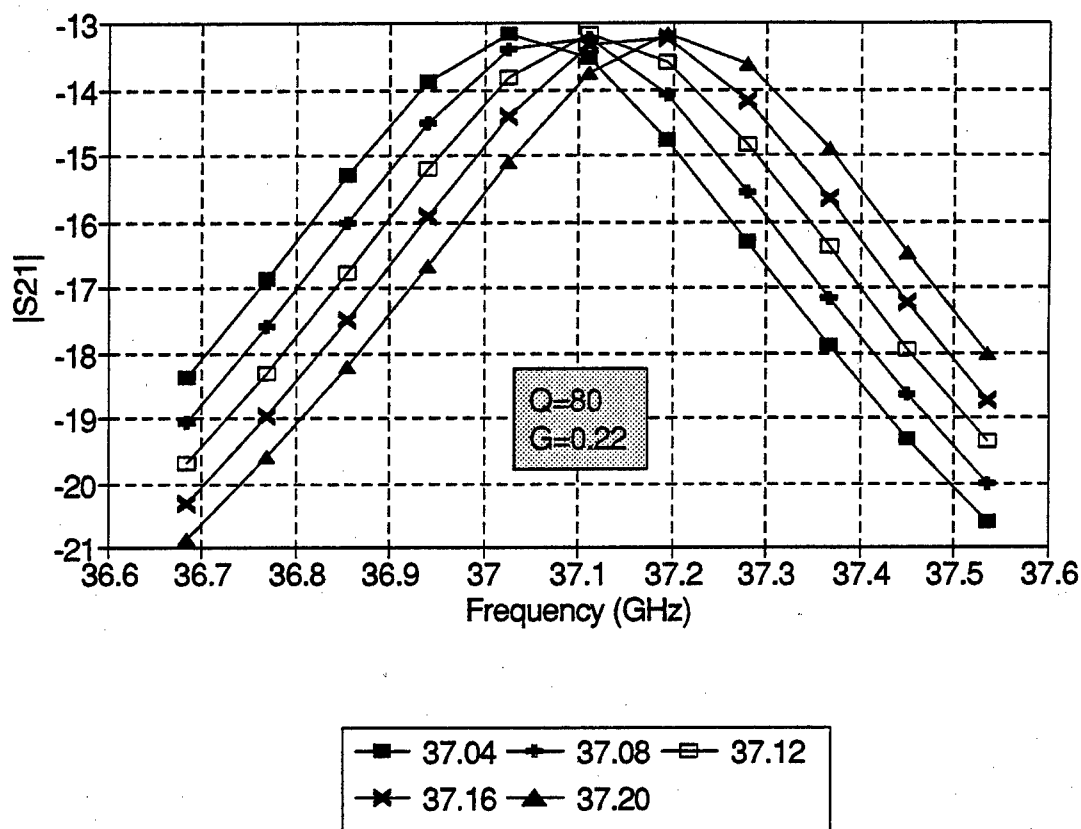


Figure 3.5 Effect of varying f_o on the nonlinear curve fit

practice.

Other investigators have examined fitting this kind of model to their data [40]. The model was fit in this case by minimizing the sum of the squared errors given by the following equation:

$$E = \sum_{i=1}^N \left[|S_{21}|_i - \frac{|S_{21}|_{max}}{\sqrt{1 + 4Q_l^2 \left(\frac{f_o - f_i}{f_o} \right)^2}} \right]^2 \quad (3.21)$$

By the way, this is obviously a nonlinear curve fit. To do a standard least-squares curve fit would involve finding the values of the three parameters for which the following are true:

$$\frac{\partial E}{\partial |S_{21}|_{max}} = 0, \quad \frac{\partial E}{\partial Q_l} = 0, \quad \text{and} \quad \frac{\partial E}{\partial f_o} = 0 \quad (3.22)$$

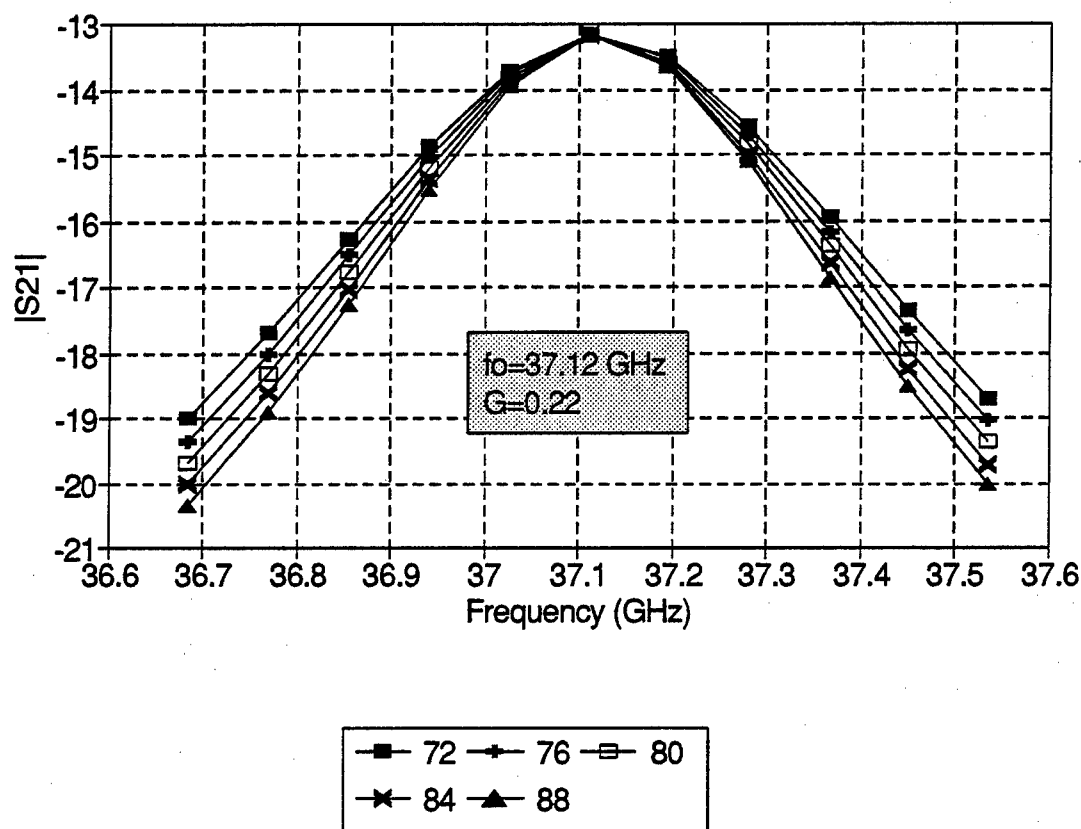


Figure 3.6 Effect of varying Q_l on the nonlinear curve fit

As the conditions in (3.22) give rise to some very nasty-looking equations (which are not reproduced here to show mercy to the reader), these fits were done pseudo-manually. That means that the data were imported into Borland's QuattroTM Pro 4.0 and the nonlinear optimizer therein was used to minimize Equation (3.21). But the optimizer had a hard time finding the minimum; in fact, it was reluctant to vary Q_l much at all. Therefore manual tweaking—varying a parameter and noting its effect on the sum of squared errors—was used, first on the resonant frequency and maximum amplitude, and then on the Q_l , with some going back and forth. Generally it was easy to find f_o , and the optimizer had no problem with that. Maximum amplitude was somewhat harder to find, but the optimizer seemed to handle that all right, also. The

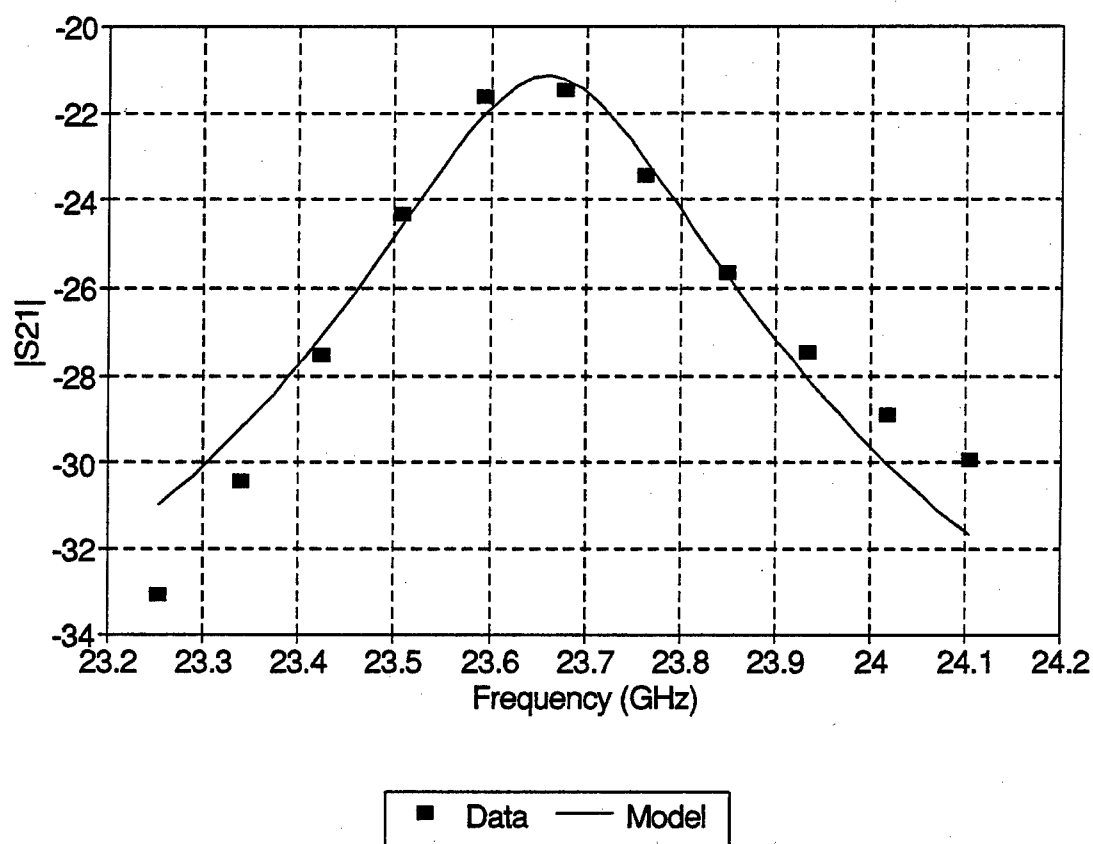


Figure 3.7 Example of a "poor" fit

loaded quality factor required frequent human intervention. It should be said that all this fitting was necessary because the data were very sparse. If the data were very dense, then the resonant frequency and maximum amplitude could have been read right off the graph, along with the -3 dB points, and Q_l could have been calculated the old-fashioned way, as resonant frequency divided by bandwidth. However, a broadband calibration was performed, and the resonators were used in several modes; thus data were sparse. Only about five data points per resonance were above the -3 dB points; for each peak eleven data points were used in the final parameter extractions. Beyond this point noise dominates the data, and the model should only be very accurate in the vicinity of the resonance anyway.

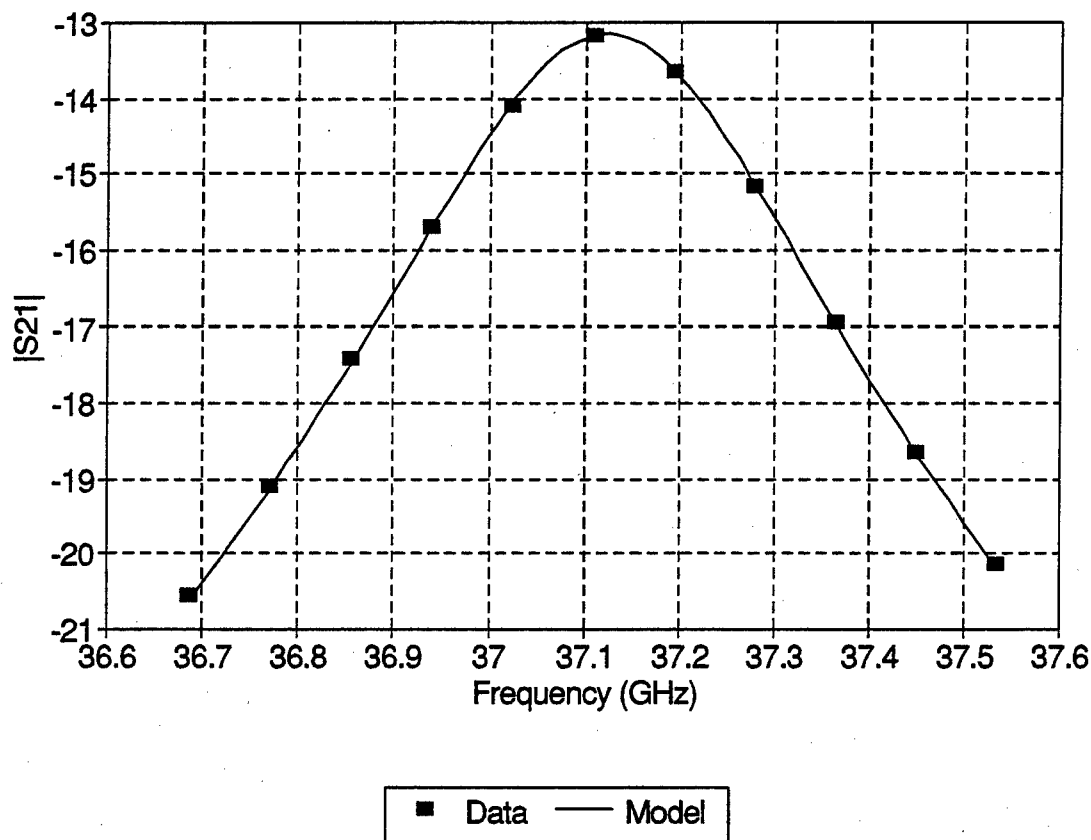


Figure 3.8 Example of a “good” fit

3.4 Consideration of ground plane loss

Holloway [4] gives in his PhD dissertation an expression for the attenuation constant due to the loss in the ground plane of a microstrip of width w and height h :

$$\alpha_{GP} = \frac{R_S}{2Z_0} \left(\frac{1}{w\pi} \right)^2 \int_{-\infty}^{\infty} \left[\tan^{-1} \left(\frac{w-2x}{2h} \right) + \tan^{-1} \left(\frac{w+2x}{2h} \right) \right]^2 dx \quad (3.23)$$

where

$$R_S = \frac{1}{\sigma\delta} = \sqrt{\frac{\pi f \mu}{\sigma}} \quad (3.24)$$

is the usual surface resistance in ohms/square. μ and σ are the permeability and conductivity of the ground plane metal, respectively. This expression assumes a

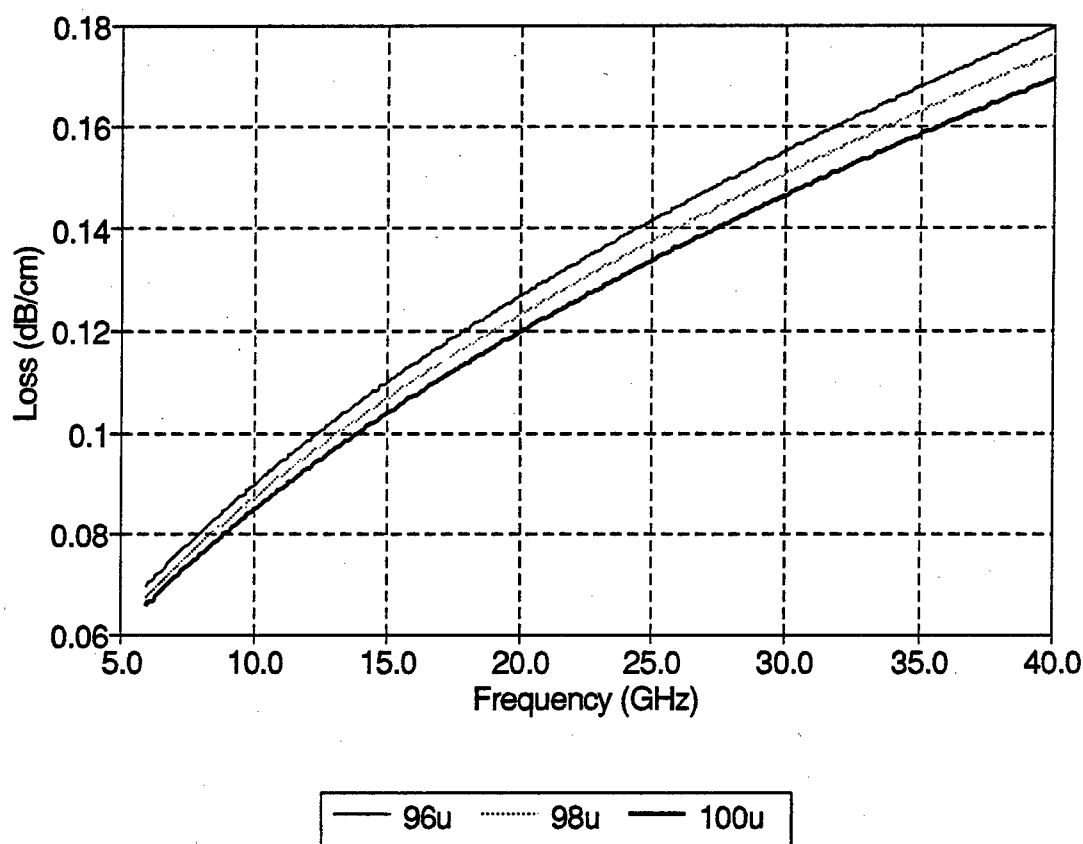


Figure 3.9 Numerically computed ground plane loss

constant strip current distribution (current density equals the total strip current divided by the strip width). Holloway used a standard wall loss perturbation analysis; he also neglected the transverse component of the current and worked only with z -directed magnetic vector potential.

The expression in (3.23) is integrated numerically to obtain ground plane losses which are extracted from total losses (in direct S_{21} measurements) in order to give the total loss of the strip and that added by the surface roughnesses. Figure 3.9 shows this ground plane loss for a gold ground plane with 73μ -wide strips on GaAs substrates of varying height h .

CHAPTER IV

LOSS MEASUREMENT RESULTS AND COMPARISONS

The measurement results are summarized and presented in this chapter. Not all fifteen wafers survived, of course, so less data were gathered than was desired. Nevertheless, a large amount of information was amassed, and enough was taken to perform some statistical analysis and to make some conclusions. It should be noted at this point that whenever reference is made in this chapter to the mean or standard deviation, that it is the sample mean and sample standard deviation which are being mentioned. The practical consequence of this distinction is that the denominator of the calculation of the standard variance s^2 is $N - 1$ instead of N . Since the mean is calculated from a limited number of observations and is not known *a priori*, using N would underestimate the standard deviation s [41-42].

4.1 TRL extraction results

We have seen that effective dielectric constant and loss can be extracted from the TRL calibration process. The only such data presented here, though, are for the smooth lines. No standards were made with parallel or transverse grooves (in retrospect, a regrettable omission). Of course, with zero-length thru and reflect standards, only the lines would need grooves. The long lines obviously are grooved, but none of the short lines are. This smooth line data, though, can be compared with $|S_{21}|$ measurements and resonator data for smooth lines.

Figure 4.1 is a graph of the effective relative dielectric constant ϵ_{re}

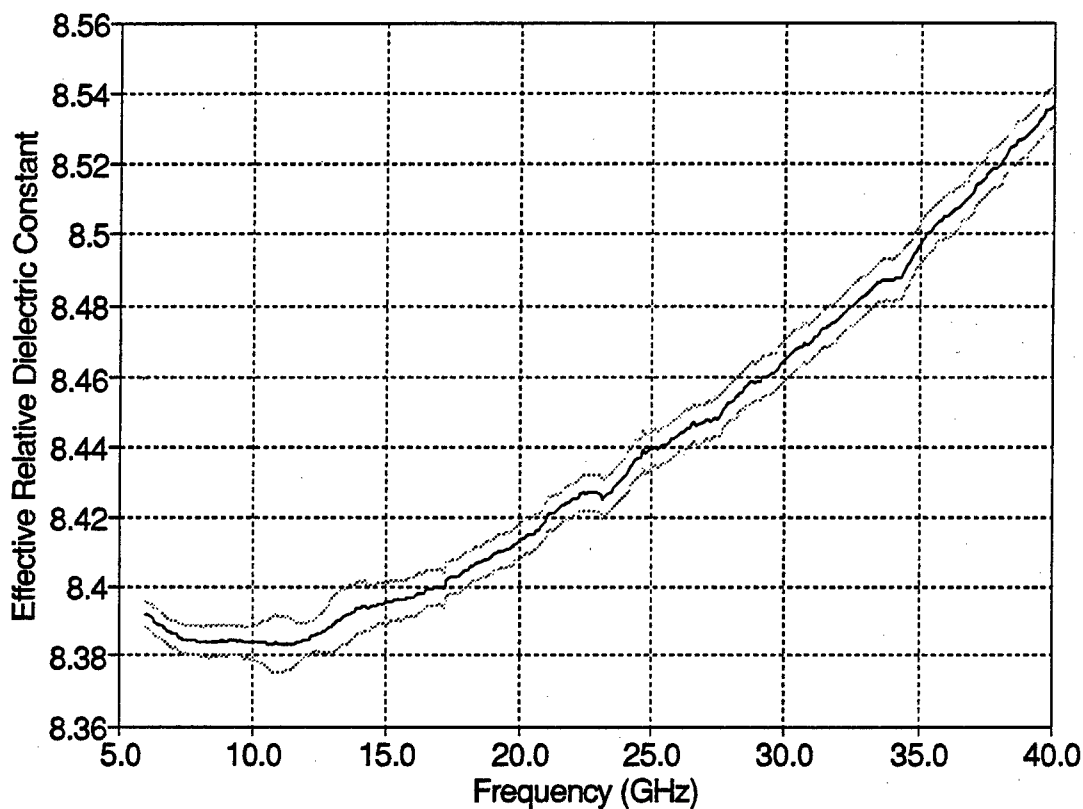


Figure 4.1 Effective relative dielectric constant extracted from TRL calibration on wafer 6

of the lines on wafer 6. The solid line is an average of the ten measurements; the dashed lines are $\epsilon_{re} \pm s$. Note that ϵ_{re} increases with frequency as theory predicts: as frequency increases, more of the electric field lines are confined underneath the strip conductor and thus in the dielectric. Therefore ϵ_{re} rises. Note also that the standard deviation s of these measurements is roughly 0.004 across the band, indicating a high degree of certainty in the measured values of ϵ_{re} .

Figure 4.2 is a graph of the loss in dB/cm from the same ten measurements on wafer 6. Like Figure 4.1, the solid line is the mean and the dashed lines are one standard deviation on each side of the mean. For graphs of single

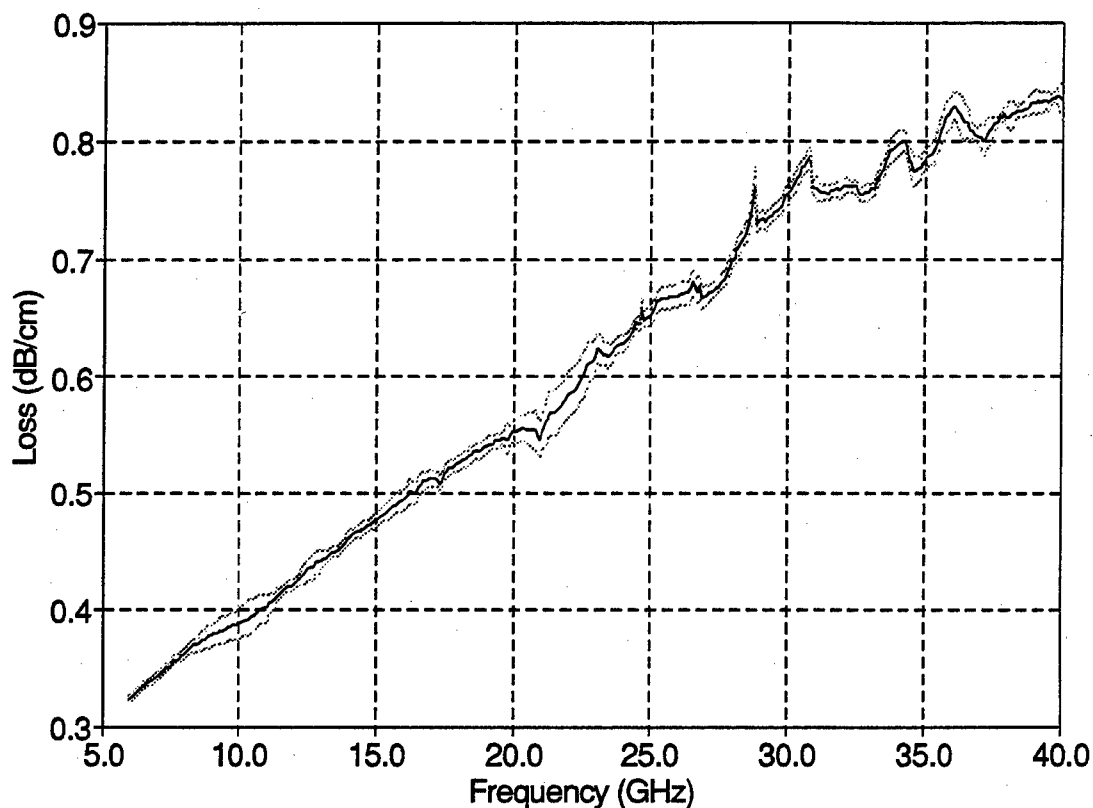


Figure 4.2 Loss extracted from TRL calibration on wafer 6

parameters with one solid and two dashed lines in the rest of this dissertation, the same meaning will apply (solid line is computed or measured value and dashed lines are value plus or minus one standard deviation). As expected the loss increases with frequency.

4.2 Direct $|S_{21}|$ results from long lines

Here we examine comparisons between lines with different surface roughnesses. The comparisons are somewhat misleading at first, because these next several graphs have not had the ground plane loss extracted yet. Therefore they show the effects of a rough surface, but only the strip is rough. Of course, the strip dimensions were chosen so that most of the loss would be contributed

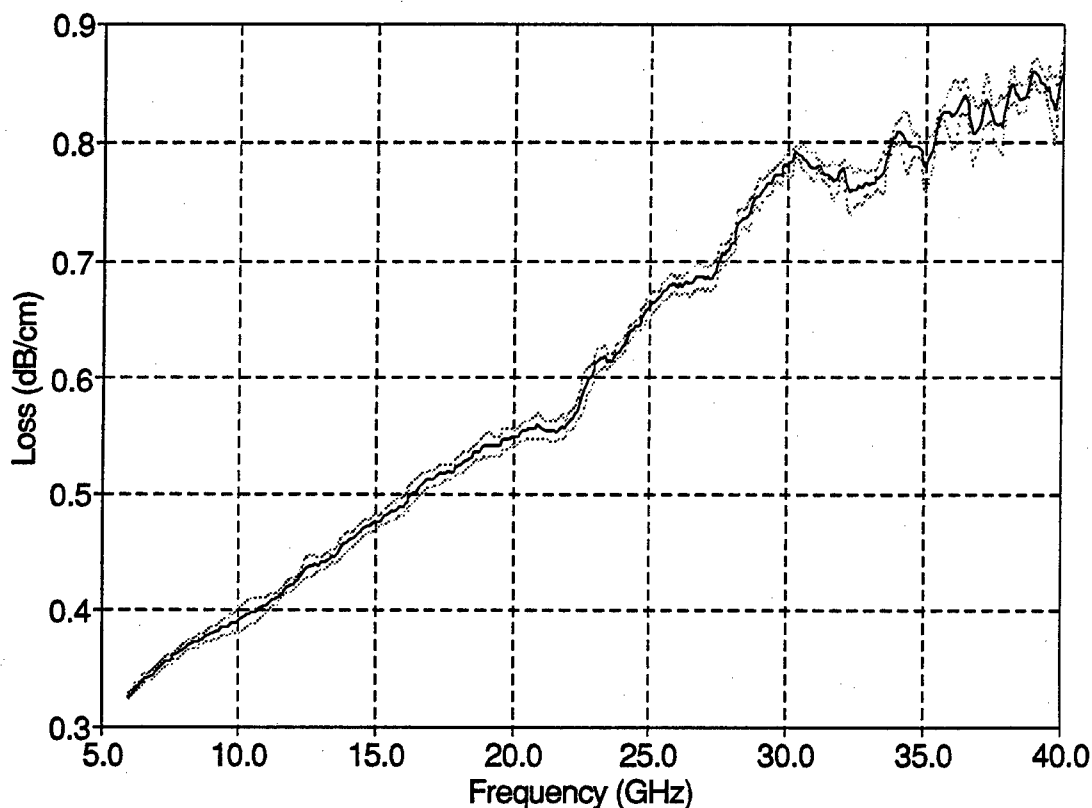


Figure 4.3 Smooth loss extracted from line 2 $|S_{21}|$ on wafer 6

by it, anyway.

Figures 4.3, 4.4, and 4.5 show the total loss due to lines with no grooves, parallel grooves, and transverse grooves, respectively. As before, these are means of ten sets of measurements, with standard deviations indicated by dotted lines. Figure 4.6 shows the means all on the same graph so that they may be compared. Figure 4.7 is the same graph as Figure 4.6 but is strip loss only (ground plane losses have been subtracted).

4.3 Two-port gap-coupled resonator results

Resonator data exist from wafers 5 and 6. Smooth, parallel, and transverse resonator data exist from wafer 5, and these data are presented in Figure

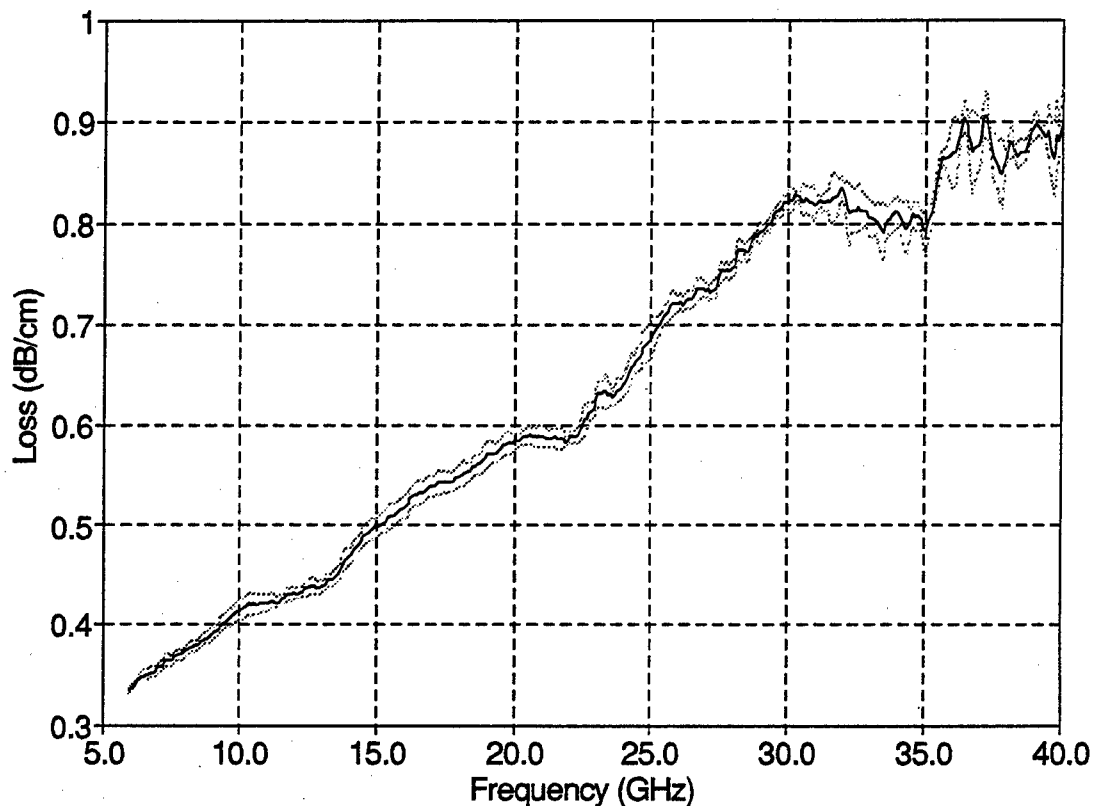


Figure 4.4 Parallel loss extracted from line 3 $|S_{21}|$ on wafer 6

4.8. Only four frequencies are given because only one (length) resonator is on this wafer, and it has four resonances in the six-to-forty gigahertz band. The lower two resonances give losses that fall on top of each other for smooth and parallel losses. The losses in Figure 4.9 are from wafer 6, but no smooth resonator survived; also different resonator lengths are on board. This means that some loss points are not directly comparable because they are at different frequencies.

All of the resonator nonlinear curve fit statistics are in Tables 4.1 through 4.3. Only one set of measurements of R1P was taken; this particular structure may be partially damaged. Only two sets of measurements of R3S,

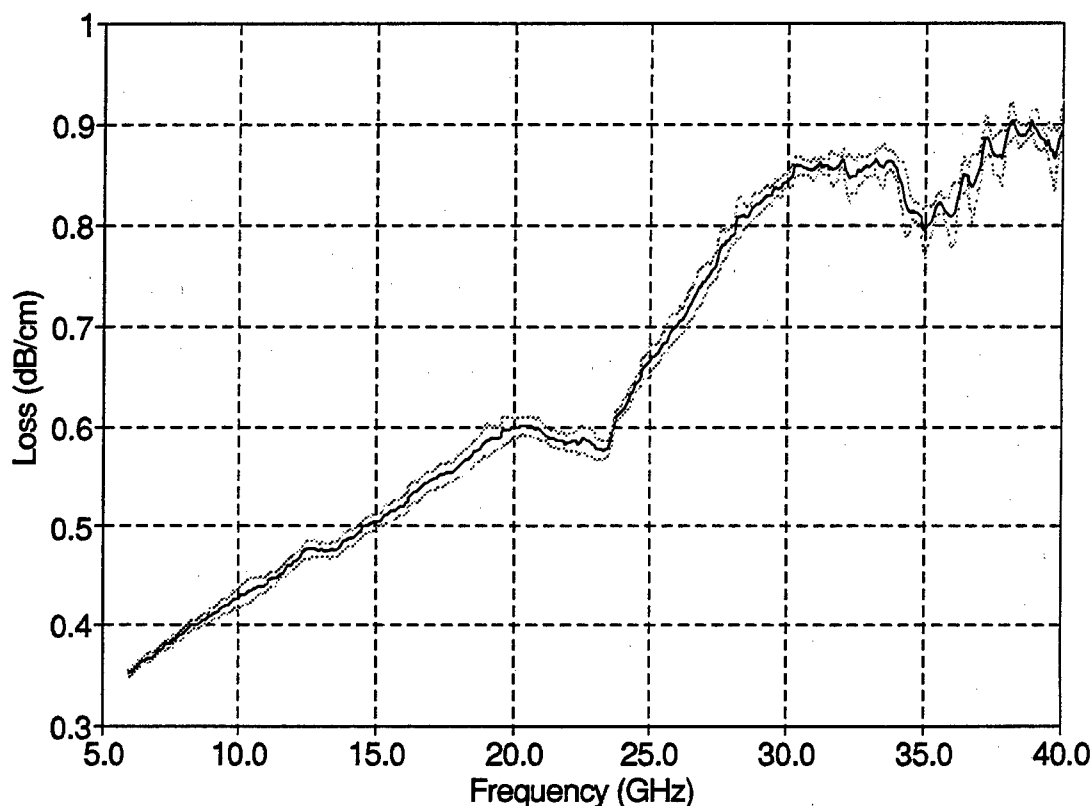


Figure 4.5 Transverse loss extracted from line 2 $|S_{21}|$ on wafer 6

R3P, and R3T from Wafer 5 were taken due to the need of the probe station for other measurements.

4.4 Data from other methods and sources

Other data are now presented. The following numbers are those arrived at by other, more (but sometimes less) traditional methods. The more traditional methods include approximate calculations by design equations empirically arrived at, and numerical results from commercial simulation software.

4.4.1 Approximate calculations

One of the latest refinements of the standard approximate design for-

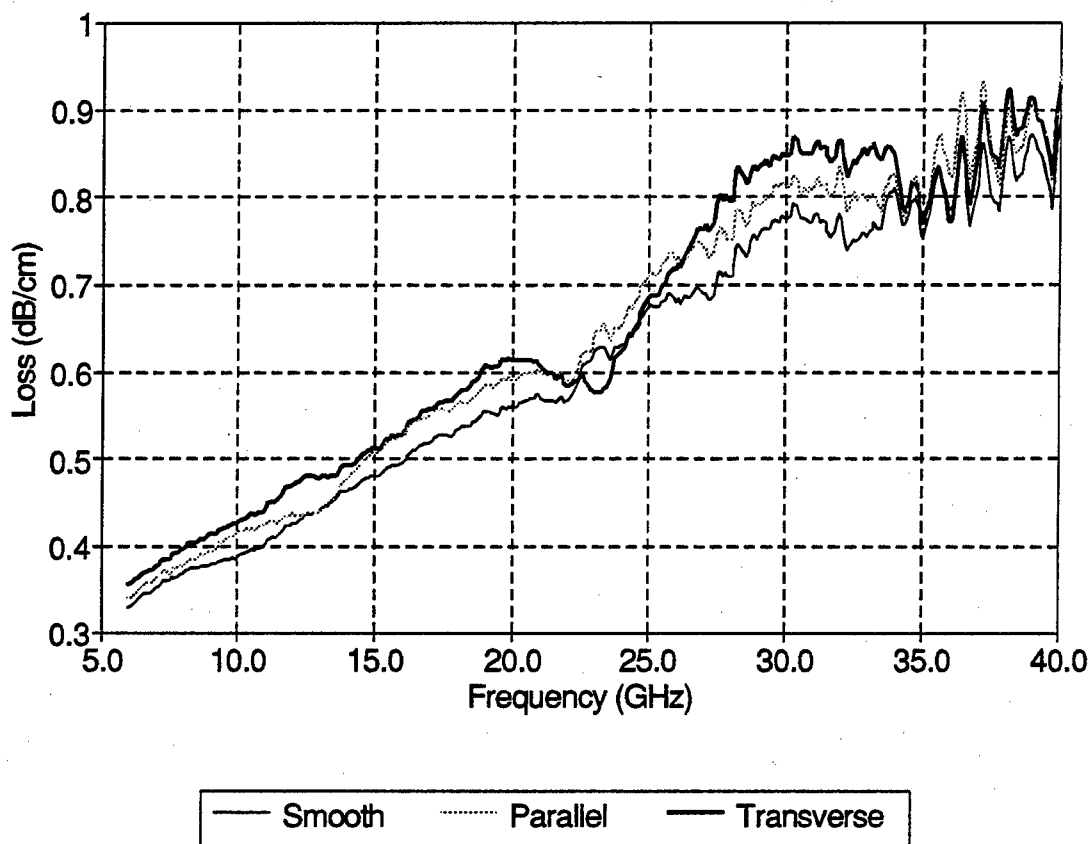


Figure 4.6 Comparison of smooth, parallel, and transverse total losses

mulas is presented below. These equations are garnered from other sources and presented verbatim so that they do not have to be looked up, and to show what equations were actually used. These equations (or similar forms) also seem to be undergoing constant revision to improve their accuracies over desired ranges of parameters.

Two numbers made use of in these formulas are the surface resistivity

R_s

$$R_s = \frac{1}{\sigma \delta} = \sqrt{\frac{\pi f \mu}{\sigma}} \quad (\Omega/\text{square}) \quad (4.1)$$

where σ is the conductivity of the metal and δ is the familiar skin depth

$$\delta = \frac{1}{\sqrt{\omega \mu \sigma}} \quad (4.2)$$

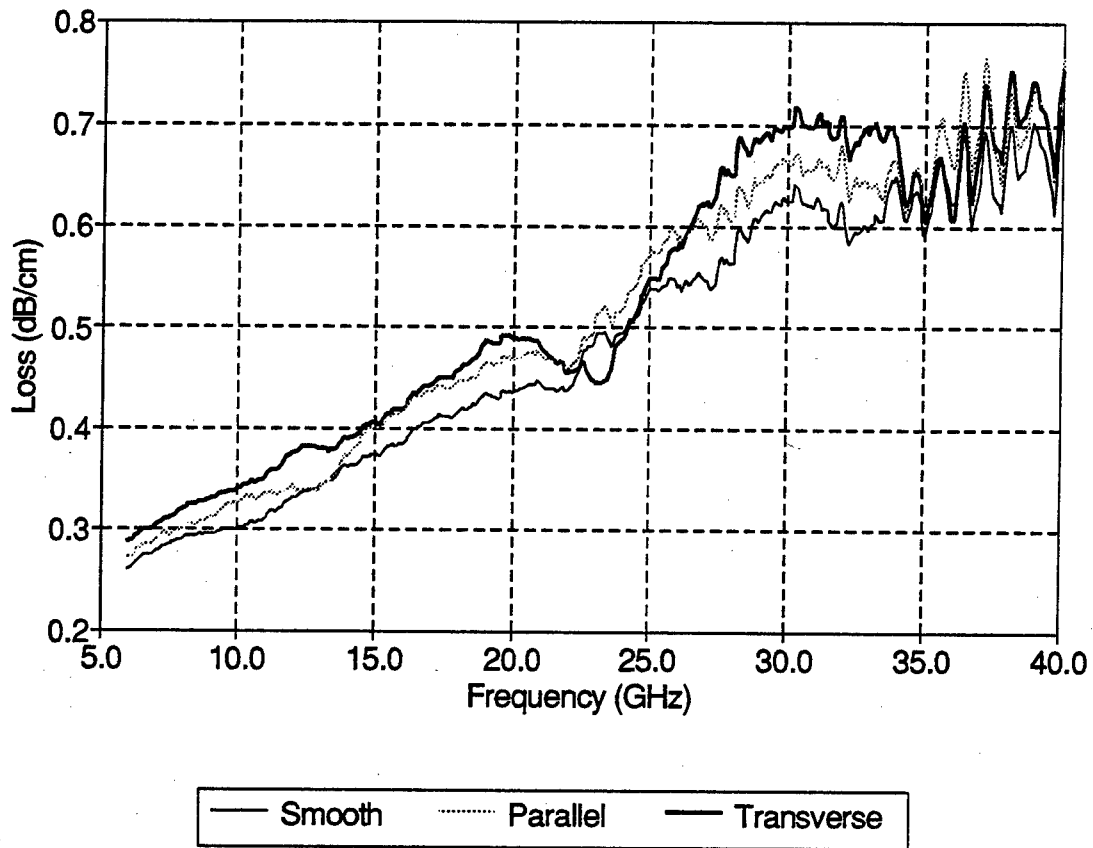


Figure 4.7 Comparison of smooth, parallel, and transverse losses of strip

where ω is the radian frequency of operation and μ is the permeability of the metal. In this dissertation μ is taken to be equal to μ_0 since only nonferrous metals (i.e., gold) are considered.

The effective dielectric constant ϵ_{re} is given by

$$\epsilon_{re} = \frac{\epsilon_r + 1}{2} + \frac{\epsilon_r - 1}{2} \left(1 + \frac{12h}{w}\right)^{-0.5} \quad \left(\frac{w}{h} \geq 1\right) \quad (4.3)$$

and

$$\epsilon_{re} = \frac{\epsilon_r + 1}{2} + \frac{\epsilon_r - 1}{2} \left[\left(1 + \frac{12h}{w}\right)^{-0.5} + 0.04 \left(1 - \frac{w}{h}\right)^2 \right] \quad \left(\frac{w}{h} \leq 1\right), \quad (4.4)$$

where ϵ_r , w , and h are as previously defined (substrate relative dielectric con-

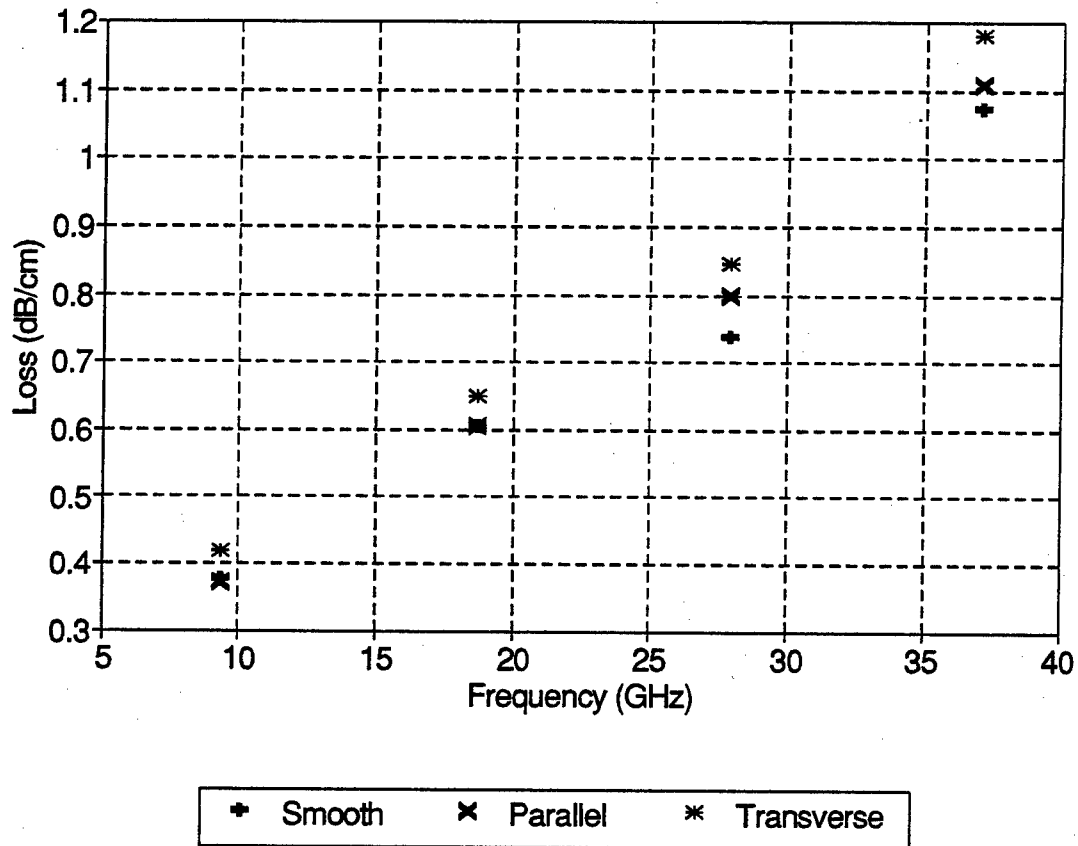


Figure 4.8 Comparison of smooth, parallel, and transverse resonator losses on Wafer 5

stant, strip width, and substrate height, respectively).

The characteristic impedance Z_o is found from

$$Z_o = \frac{\eta_o}{2\sqrt{2}\pi\sqrt{\epsilon_r + 1}} \ln \left\{ 1 + \frac{4h}{w} \left[\frac{14 + \frac{8}{\epsilon_r}}{11} \frac{4h}{w} + \sqrt{\left(\frac{14 + \frac{8}{\epsilon_r}}{11} \right)^2 \left(\frac{4h}{w} \right)^2 + \frac{1 + \frac{1}{\epsilon_r}}{2} \pi^2} \right] \right\} \quad (4.5)$$

in which $\eta_o = \sqrt{\frac{\mu_o}{\epsilon_o}}$ is the characteristic impedance of free space.

All these are quasistatic ($f = 0$) quantities for zero-thickness ($t = 0$) microstrip. There exist corrections for nonzero-thickness strips and for dis-

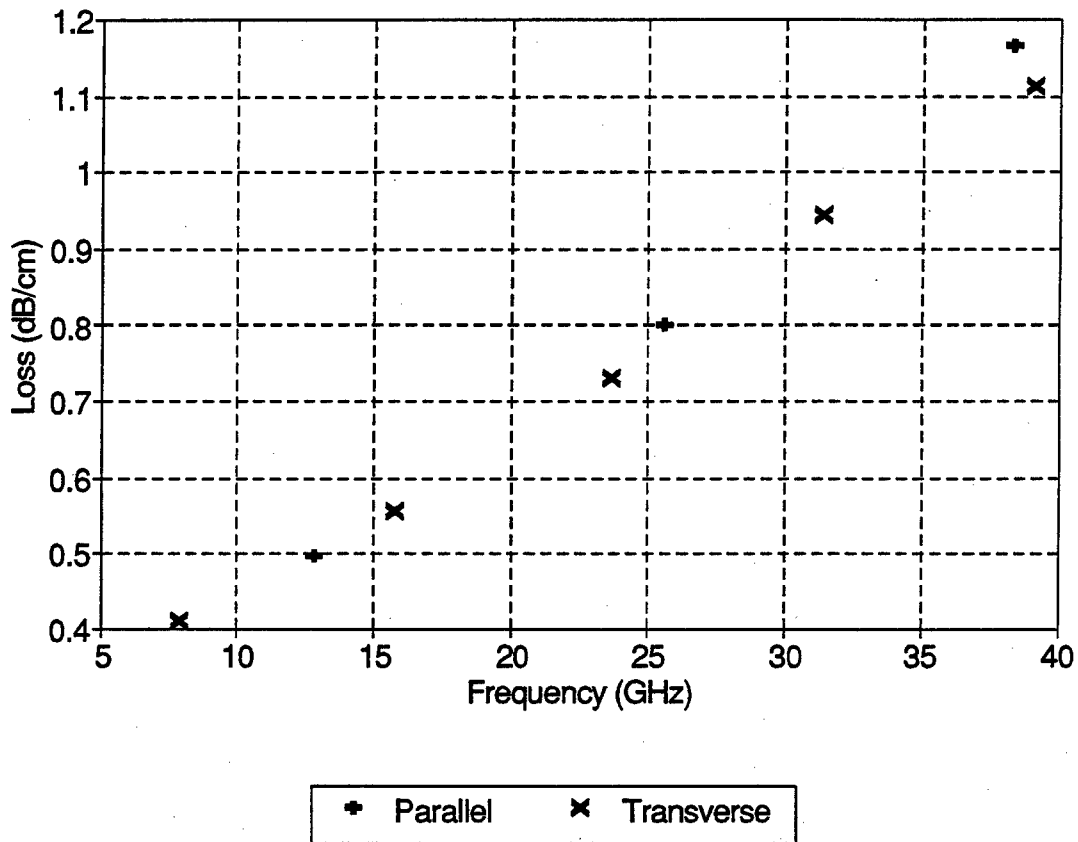


Figure 4.9 Comparison of parallel and transverse resonator losses on Wafer 6

persion (frequency dependence of ϵ_{re}). The usual nonzero-thickness correction approach is to modify the value of the strip width w by adding an additional incremental width Δw to arrive at a corrected width w' as follows:

$$\Delta w = \frac{t}{\pi} \ln \left[\frac{4e}{\sqrt{\left(\frac{t}{h}\right)^2 + \left(\frac{1/\pi}{w/t+1.1}\right)^2}} \right] \quad (4.6)$$

$$\Delta w' = \Delta w \left(\frac{1 + 1/\epsilon_r}{2} \right) \quad (4.7)$$

$$w' = w + \Delta w' \quad (4.8)$$

Table 4.1 Wafer 6 R5P and R1P Curve Fit Statistics

Peak Number	Frequency (GHz)	Q_0	Residual	α (dB/cm)
R5P				
1	12.8184	67.7785	3.11E-6	0.4980
1	12.8171	68.2594	3.97E-6	0.4947
1	12.8168	67.9720	3.69E-6	0.4968
1	12.8173	67.9426	2.88E-6	0.4970
1	12.8193	67.9534	3.65E-6	0.4967
1	12.8177	67.9577	3.74E-6	0.4969
1	12.8177	67.9740	4.44E-6	0.4967
1	12.8154	67.9490	1.63E-6	0.4967
avg	12.8175	-	-	0.4967
std	00.0011	-	-	0.0009
2	25.6001	84.2145	1.07E-6	0.8030
2	25.5969	83.6461	3.82E-6	0.8088
2	25.5967	84.6621	2.78E-6	0.7991
2	25.5987	84.7382	2.68E-6	0.7985
2	25.6015	84.5925	1.59E-6	0.7995
2	25.5984	84.5951	2.49E-6	0.7999
2	25.5980	84.6033	3.37E-6	0.7997
2	25.5951	84.4161	7.27E-6	0.8013
avg	25.5984	-	-	0.8001
std	00.0019	-	-	0.0014
3	38.3189	87.3254	5.53E-6	1.1647
3	38.3135	89.4877	1.55E-5	1.1370
3	38.3082	87.1952	5.12E-6	1.1668
3	38.3101	87.2507	9.26E-6	1.1661
3	38.3141	87.3270	6.13E-6	1.1646
3	38.3095	87.3416	1.40E-5	1.1650
3	38.3093	87.3979	1.50E-5	1.1640
3	38.3073	87.1123	6.81E-6	1.1678
avg	38.3113	-	-	1.1657
std	00.0040	-	-	0.0013
R1P				
1	06.9232	52.8352	1.29E-6	0.3450
2	13.8371	72.2057	7.49E-6	0.5047
3	20.7052	87.6662	2.12E-6	0.6229
4	27.5638	90.1732	3.94E-5	0.8079
5	34.3611	98.6639	5.00E-5	0.9226

Table 4.2 Wafer 6 R2T Curve Fit Statistics

Peak Number	Frequency (GHz)	Q_0	Residual	α (dB/cm)
1	07.9054	52.0458	1.92E-6	0.3998
1	07.9054	52.0390	2.02E-6	0.4001
1	07.9033	51.0160	2.10E-6	0.4080
1	07.9033	51.0228	1.53E-6	0.4080
1	07.9033	51.0186	1.90E-6	0.4078
1	07.9034	51.0118	2.19E-6	0.4082
1	07.9034	51.0179	2.32E-6	0.4080
1	07.9034	51.0000	1.84E-6	0.4083
avg	07.9034	-	-	0.4081
std	5E-5	-	-	0.0002
2	15.7946	75.1066	1.11E-5	0.5540
2	15.7921	75.0424	1.22E-5	0.5546
2	15.7913	75.1256	1.28E-5	0.5540
2	15.7930	75.0975	1.19E-5	0.5543
2	15.7948	75.1144	1.33E-5	0.5539
2	15.7915	75.1134	1.23E-5	0.5542
2	15.7921	75.1118	1.24E-5	0.5541
2	15.7921	75.1550	1.14E-5	0.5539
avg	15.7927	-	-	0.5541
std	00.0013	-	-	0.0002
3	23.6545	80.9783	3.58E-5	0.7711
3	23.6448	84.1463	7.22E-5	0.7421
3	23.6473	85.4495	8.13E-5	0.7309
3	23.6527	86.4273	9.02E-5	0.7228
3	23.6489	85.3974	2.24E-5	0.7310
3	23.6463	85.3704	2.79E-5	0.7317
3	23.6476	85.4406	2.22E-5	0.7310
3	23.6310	85.4213	5.20E-5	0.7304
avg	23.6442	-	-	0.7310
std	00.0067	-	-	0.0004
4	31.4163	88.2848	1.08E-5	0.9418
4	31.4114	88.2899	1.90E-5	0.9421
4	31.4098	88.1432	1.02E-5	0.9437
4	31.4105	88.1154	8.15E-6	0.9440
4	31.4157	88.1831	8.19E-6	0.9429
4	31.4099	88.1779	1.21E-5	0.9433
4	31.4099	88.1278	8.47E-6	0.9437
4	31.4099	76.7000	9.60E-6	0.9447
avg	31.4110	-	-	0.9435
std	00.0020	-	-	0.0008
5	39.1577	93.3466	2.26E-5	1.1139
5	39.1497	91.3018	1.19E-5	1.1391
5	39.1476	93.4342	2.48E-5	1.1131
5	39.1510	93.5007	1.97E-5	1.1124
5	39.1554	93.5223	2.22E-5	1.1117
5	39.1502	93.4578	2.54E-5	1.1130
5	39.1484	93.4946	7.08E-5	1.1123
5	39.1473	93.6408	1.38E-5	1.1106
avg	39.1511	-	-	1.1124
std	00.0037	-	-	0.0010

Table 4.3 Wafer 5 R3S, R3P, R3T (Resonator 3: Smooth, Parallel, Transverse) Curve Fit Statistics

Peak Number	Frequency (GHz)	Q_o	Residual	α (dB/cm)
R3S				
1	09.3879	67.4902	9.86E-6	0.3651
1	09.3898	63.2882	7.46E-6	0.3891
avg	09.3889	-	-	0.3771
2	18.7351	81.2699	1.56E-5	0.6062
2	18.7369	81.2633	1.64E-5	0.6060
avg	18.7360	-	-	0.6061
3	28.0024	94.8330	4.01E-6	0.7787
3	28.0053	93.6806	1.82E-5	0.7879
avg	28.0039	-	-	0.7833
4	37.1780	93.8788	6.53E-6	1.0489
4	37.1841	89.4470	1.65E-5	1.1005
avg	37.1811	-	-	1.0747
R3T				
1	09.3573	68.7296	1.36E-5	0.3573
1	09.3587	63.4497	9.19E-6	0.3869
avg	09.3580	-	-	0.3721
2	18.6921	81.0044	9.04E-6	0.6068
2	18.6951	80.9543	6.06E-6	0.6069
avg	18.6936	-	-	0.6069
3	27.9491	92.5263	4.18E-6	0.7965
3	27.9550	92.4895	5.80E-6	0.7966
avg	27.9521	-	-	0.7966
4	37.1230	90.9298	4.62E-6	1.0813
4	37.1303	86.6546	5.69E-6	1.1343
avg	37.1267	-	-	1.1078
R3T				
1	09.3346	62.0335	9.74E-6	0.3949
1	09.3339	55.7489	7.55E-6	0.4391
avg	09.3343	-	-	0.4170
2	18.6208	76.5255	2.34E-5	0.6398
2	18.6230	74.2342	1.18E-5	0.6593
avg	18.6219	-	-	0.6496
3	27.8535	87.0046	2.30E-5	0.8442
3	27.8587	86.9485	1.73E-5	0.8444
avg	27.8561	-	-	0.8443
4	36.9835	82.4678	1.74E-5	1.1878
4	36.9800	83.6923	1.03E-2	1.1696
avg	36.9818	-	-	1.1787

This w' is then substituted back into the previous equations in place of w to arrive at the new values of ϵ_{re} and Z_o for $t \neq 0$.

The dispersion correction is incorporated as follows, with f in GHz and h in cm:

$$\epsilon_{re}(f) = \epsilon_r - \frac{\epsilon_r - \epsilon_{re}(f=0)}{1 + P(f)} \quad (4.9)$$

$$P(f) = P_1 P_2 [(0.1844 + P_3 P_4)(10 f h)] \quad (4.10)$$

$$P_1 = 0.27488 + \left[0.6315 + \frac{0.525}{(1 + 0.157 f h)^{20}} \right] \frac{w}{h} - 0.065683 e^{-8.7513 w/h} \quad (4.11)$$

$$P_2 = 0.33622 [1 - e^{-0.03442 \epsilon_r}] \quad (4.12)$$

$$P_3 = 0.0363 e^{-4.6 w/h} [1 - e^{-(f h / 3.87)^{4.97}}] \quad (4.13)$$

$$P_4 = 1 + 2.751 [1 - e^{-(\epsilon_r / 15.916)^8}] \quad (4.14)$$

The accuracy of this dispersion correction is given as better than 0.6% for

$$0.1 \leq w/h \leq 100$$

$$1 \leq \epsilon_r \leq 20$$

$$0 \leq h/\lambda \leq 0.13$$

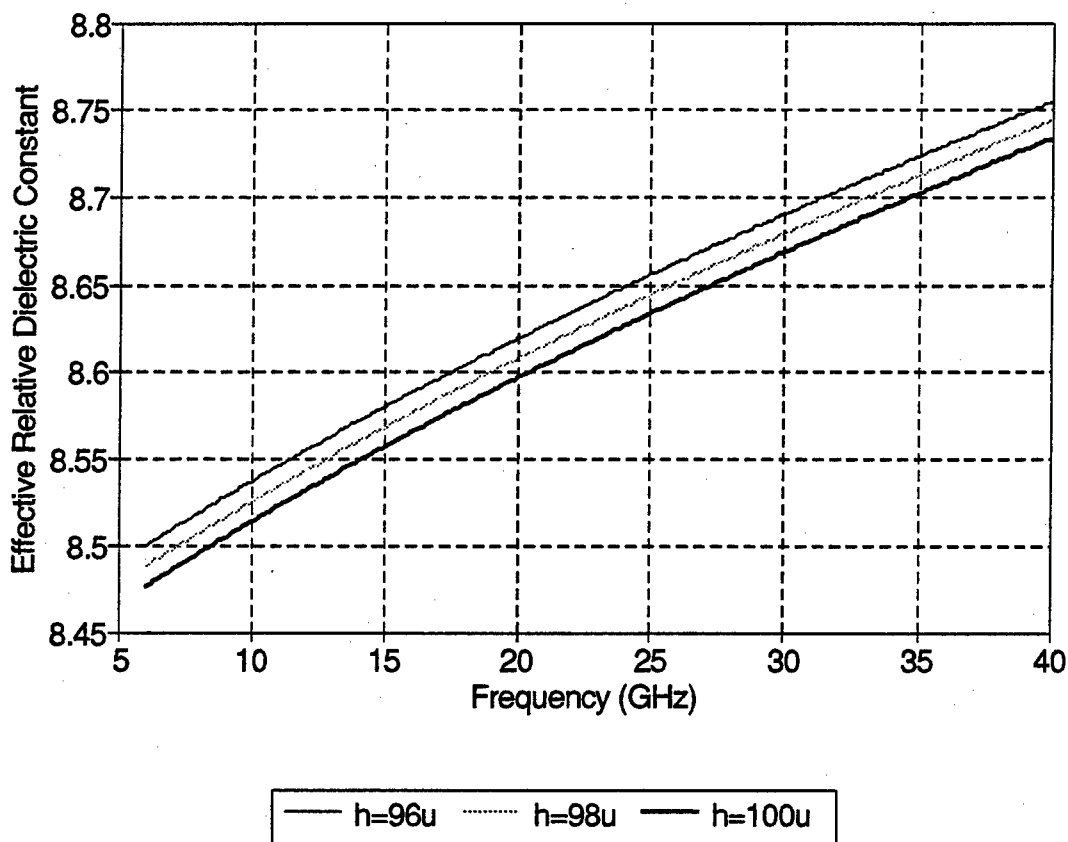


Figure 4.10 $\epsilon_{re}(f)$ calculated from design formulas

One set of equations given for calculating conductor losses due to the skin effect and finite conductivity is cited by Wadell [3]. For $w/h \leq 1$,

$$\alpha_c = \frac{10 R_S}{\pi \ln 10} \frac{\left(\frac{8h}{w} - \frac{w}{4h}\right) \left(1 + \frac{h}{w} + \frac{h}{w} \frac{\partial w}{\partial t}\right)}{h Z_o e^{Z_o/60}} \quad (4.15)$$

For $w/h \geq 1$,

$$\alpha_c = \frac{Z_o R_S}{720 \pi^2 h \ln 10} \left[1 + \left(\frac{0.44 h^2}{w^2} \right) + \frac{6 h^2}{w^2} \left(1 - \frac{h}{w} \right)^5 \right] \times \left(1 + \frac{w}{h} + \frac{\partial w}{\partial t} \right) \quad (4.16)$$

These values of α_c are in dB/unit length, and $\frac{\partial w}{\partial t}$ is defined as follows:

$$\frac{\partial w}{\partial t} = \left(\frac{1}{\pi} \right) \ln \frac{4 \pi w}{t} \quad \text{for} \quad \frac{w}{h} \leq \frac{1}{2 \pi} \quad (4.17)$$

noindent and

$$\frac{\partial w}{\partial t} = \left(\frac{1}{\pi}\right) \ln \frac{2h}{t} \quad \text{for} \quad \frac{w}{h} \geq \frac{1}{2\pi} \quad (4.18)$$

These equations are claimed valid for

$$t \ll h,$$

$$t < h/2, \text{ and}$$

$$\frac{\partial w}{\partial t} > 1.$$

For the surface roughness correction, one source cites the equation

$$\alpha_c = \alpha_{c,0} \left\{ 1 + \frac{2}{\pi} \tan^{-1} \left[1.40 \left(\frac{\Delta}{\delta} \right)^2 \right] \right\} \quad (4.19)$$

in which $\alpha_{c,0}$ is the smooth loss calculated from Equations (4.16) through (4.19), Δ is the rms surface roughness, and δ is the skin depth.

These equations were used to calculate microstrip parameters for the real lines on the wafers fabricated for this research. Figure 4.10 is the dispersive effective relative dielectric constant. Figures 4.11 through 4.14 show the different variations of the line loss. Figure 4.11 plots α for $h = 96\mu$ with rms surface roughnesses of 0μ , 0.125μ , and 0.25μ (no grooves, 0.25μ -deep grooves, and 0.5μ -deep grooves, respectively). Figure 4.12 is the same for $h = 98\mu$, and Figure 4.13 lets $h = 100\mu$. These different data are presented because, as noted in Chapter 2, h varies across the wafer. Figure 4.14 shows how α varies with respect to h for an rms surface roughness of 0.125μ (the most likely value of surface roughness for Wafer 6, based on scanning electron microscope measurements). Note that Figure 4.14 only shows the 35-40 GHz range; this is because the approximate formula given actually has a very small roughness correction factor. Only a small frequency range was presented so that the change in α with respect to rms surface roughness could be seen.

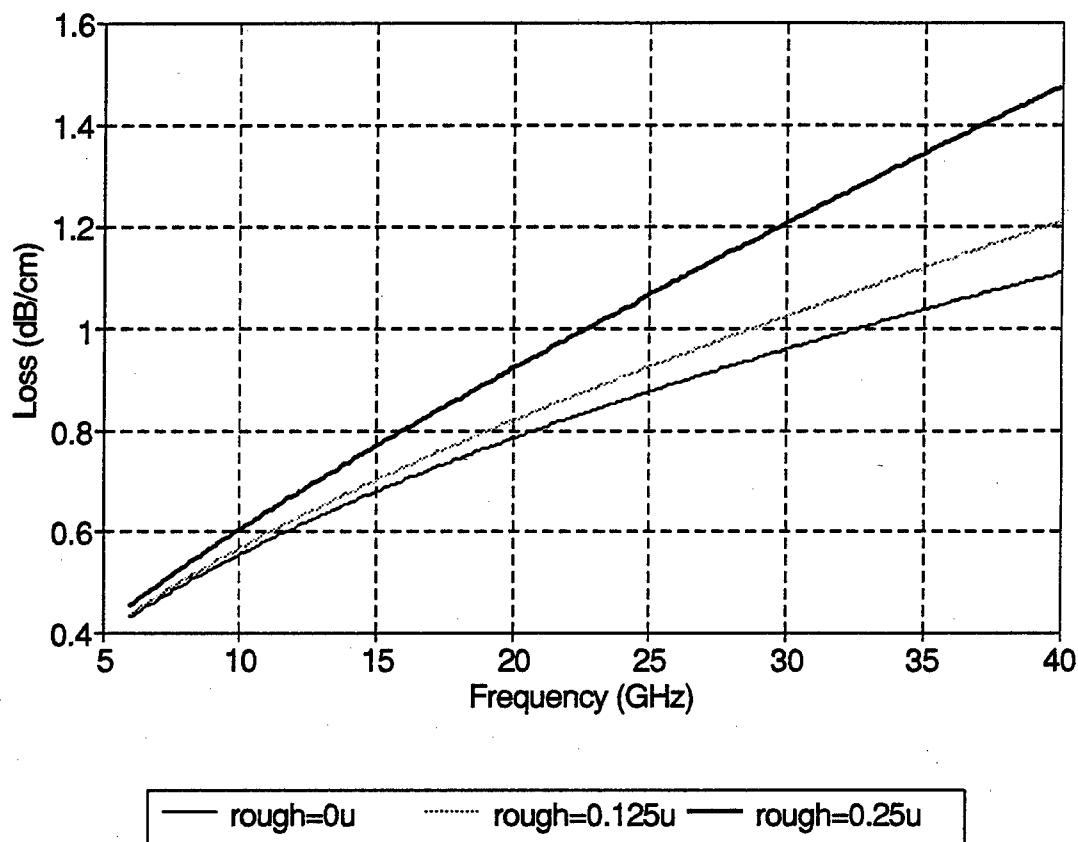


Figure 4.11 Loss calculated from design formulas for $h = 96\mu$, variable roughness

4.4.2 Hewlett-Packard Microwave Design System (MDS)

The commercially available program Microwave Design System (MDS) by Hewlett-Packard accounts for microstrip loss due to lossy dielectric (not considered in this work), finite conductivity, and surface roughness. MDS essentially incorporates the phenomenological loss model as described by Itoh [50]. The surface roughness is implemented empirically from experimental data in a very simple fashion.

MDS was used to model the lines as fabricated on the real wafers. Nonuniform wafer thickness is not supported in MDS, so the simulations were run for several values of h and rms surface roughness as for the approximate

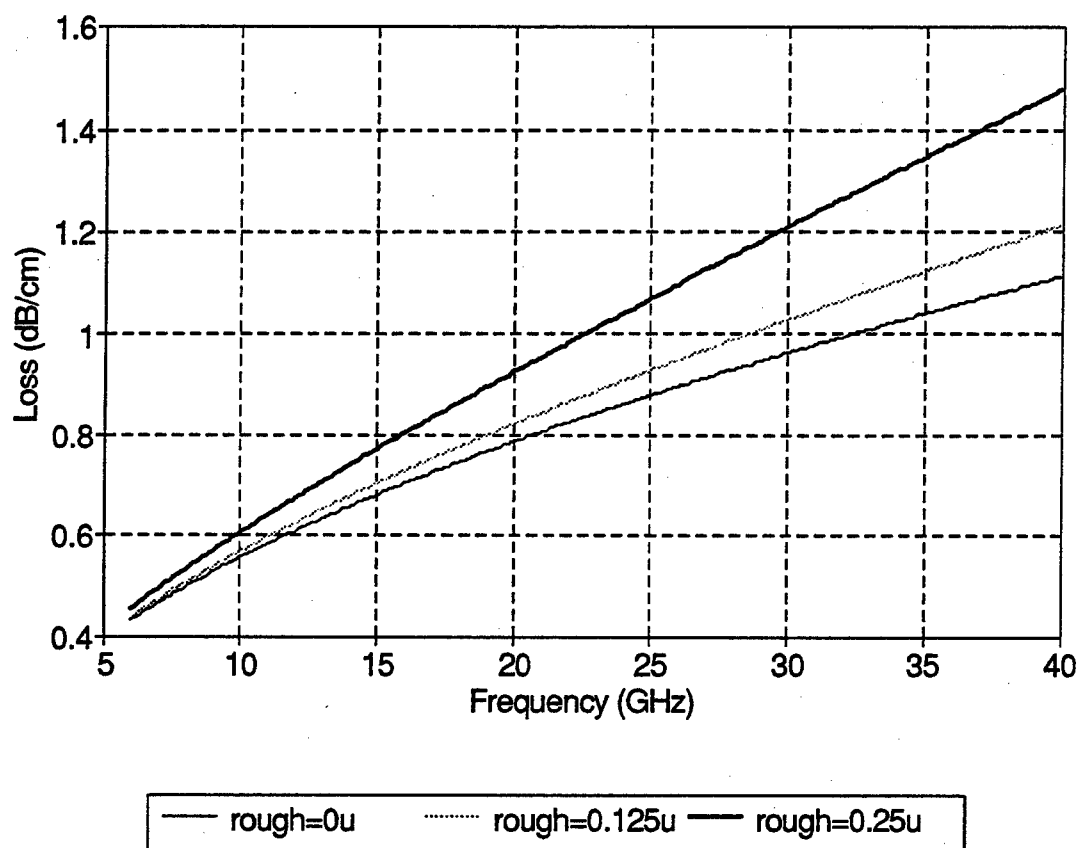


Figure 4.12 Loss calculated from design formulas for $h = 98\mu$, variable roughness

formulas; this makes comparisons relatively easy. Results for $h = 98\mu$ and $\sigma = 0.125\mu$ are presented, as for the approximate formulas, since those dimensions most closely match what was actually fabricated.

Figure 4.15 shows α for $h = 96\mu$ with rms surface roughnesses of 0μ , 0.125μ , and 0.25μ (no grooves, 0.25μ -deep grooves, and 0.5μ -deep grooves, respectively). Figure 4.16 is the same for $h = 98\mu$, and Figure 4.17 has $h = 100\mu$. noted in Chapter 2, h varies across the wafer. Figure 4.14 shows how α varies with respect to h for an rms surface roughness of 0.125μ (again, the most likely value of surface roughness for Wafer 6) Note that, like Figure 4.14, Figure 4.18 only shows the 35-40 GHz range due to the small variation in the

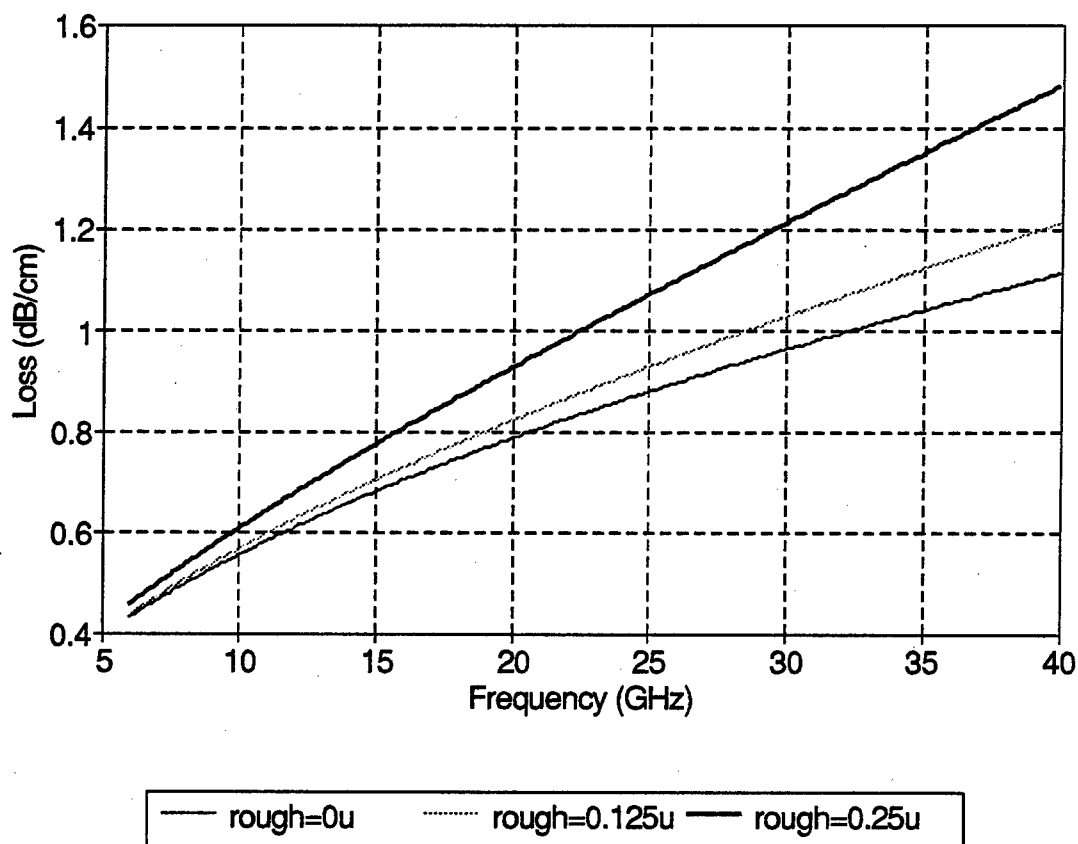


Figure 4.13 Loss calculated from design formulas for $h = 100\mu$, variable roughness

roughness correction at this small value of surface roughness.

4.4.3 Other experimental data

One set of experimental data available (and often quoted) in the literature is Goldfarb's and Platzker's [30] resonator data. They made careful loss measurements on microstrip resonators of varying widths on a nominal 100μ thick GaAs substrate. These structures have no roughness; at least none is mentioned. The nearest similar structure in their work is a 70μ wide line. All the lines in this research are 73μ wide, so the results are similar, but not directly comparable. In fact, their lines should be slightly more lossy since they are narrower. These data have been read off of a graph in Goldfarb's and

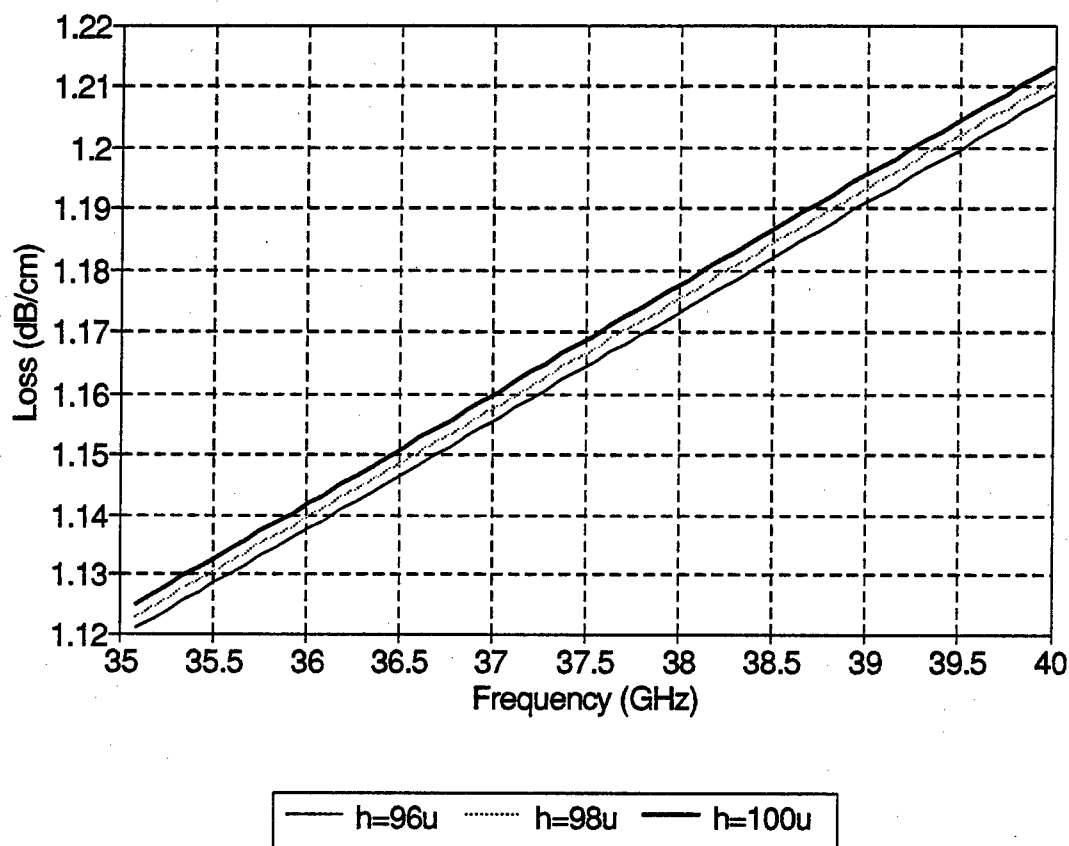


Figure 4.14 Loss calculated from design formulas for rms roughness = 0.125μ , variable h

Platzker's paper, so the numbers may differ slightly from their actual values; however, they are close enough for rough comparisons. The data are presented in tabular form here and are included on some of the graphs presented later. Note that the error bars are not plotted, but are tabulated.

4.5 Comparisons

Finally, all the losses are brought together. First of all, though, Figure 4.19 is a comparison of α extracted from the TRL measurement and α from S-parameter measurements; as before, these are actually the means of ten sets of measurements.

The next three figures capture, essentially, the essence of Chapters 2, 3,

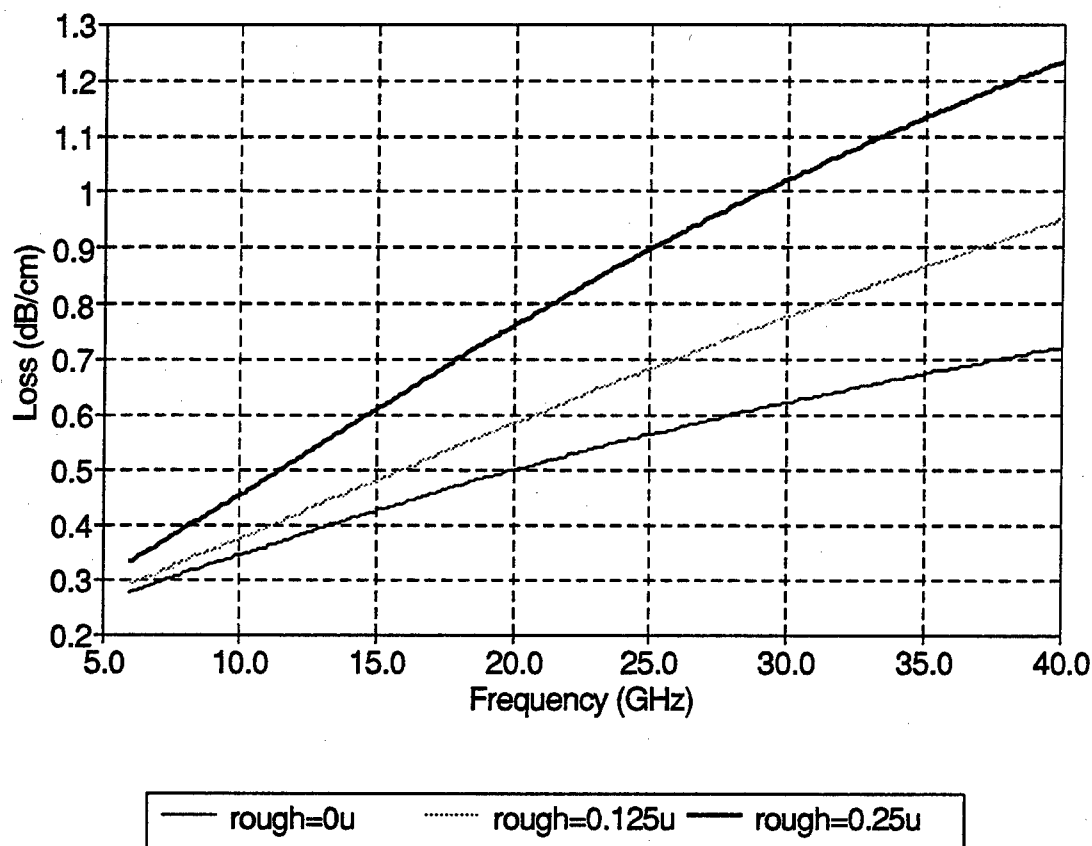


Figure 4.15 Loss calculated with MDS for $h = 96\mu$, variable roughness

and 4, and indeed all of the experimental work. Figures 4.20 through 4.22 bring together the losses as measured and calculated in different ways together for comparison. Figure 4.20 is the data for smooth (unroughened) microstrip. On this graph are S-parameter measurements, approximate formula calculations, MDS calculations, smooth resonator data from a Wafer 5 (the line data are from Wafer 6), and Goldfarb's resonator data. As mentioned before, Goldfarb's data are for slightly narrower lines.

Figure 4.21 is contains the same information, except that Goldfarb did not make measurements on roughened surfaces; therefore his data are only on Figure 4.20. Instead resonator data from Wafer 6 are included. Note that

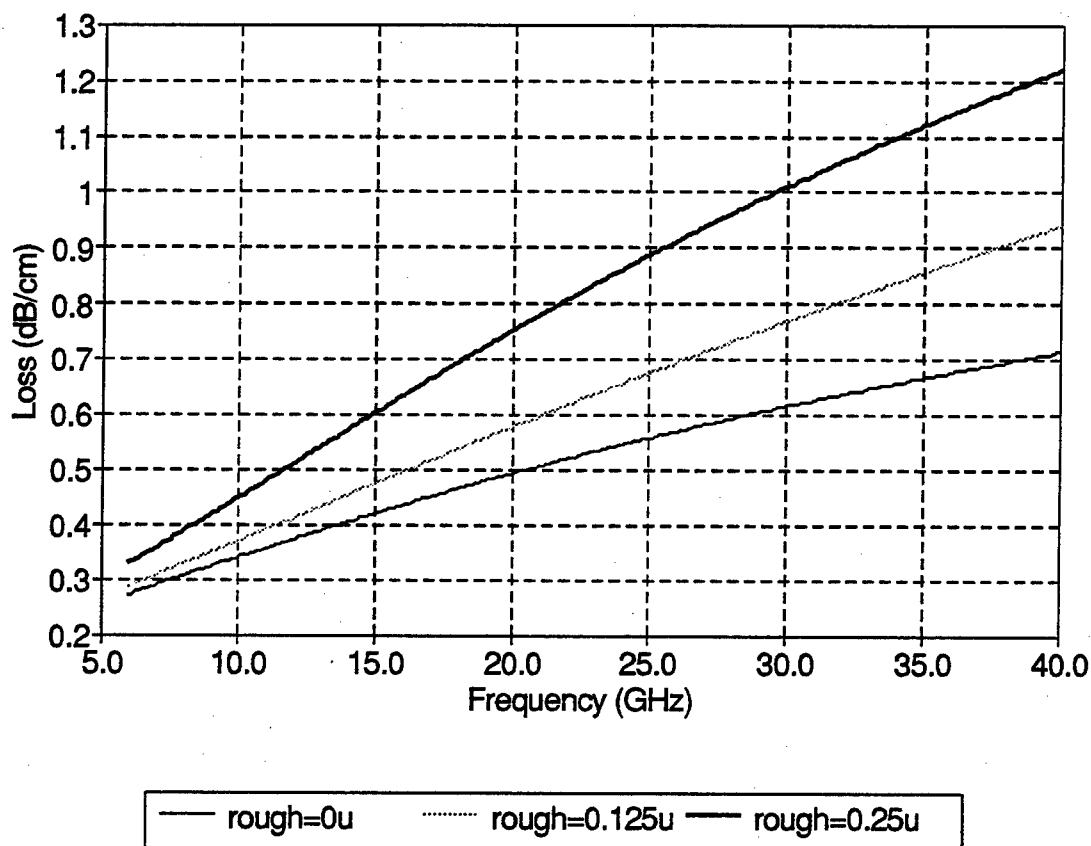


Figure 4.16 Loss calculated with MDS for $h = 98\mu$, variable roughness

MDS and the approximate formulas do not distinguish between parallel and transverse grooves, so these data are the same as those presented in Figure 4.22. That figure contains the same information, except the resonator data and S-parameter data are from structures with transverse grooves. Only this work provides the measurements on roughnesses of different “polarization.”

A few generalities can be seen. First, the approximate formulas seem to form an upper bound, while MDS seems to give a lower bound on the loss. Line measurements coincide with MDS or lie between the extremes, whereas most of the resonator data seems to be scattered within these two bounds.

More specifically, in Figure 4.20 Goldfarb's data lie between the MDS

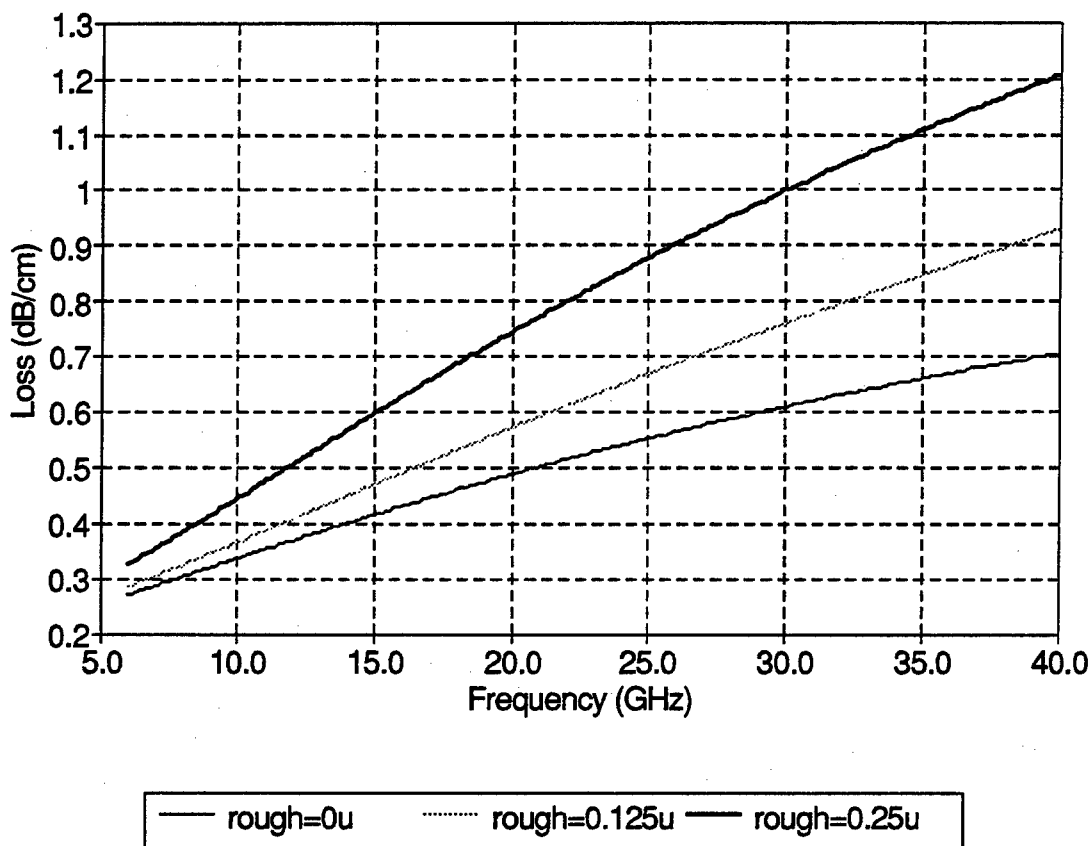


Figure 4.17 Loss calculated with MDS for $h = 100\mu$, variable roughness

and measured $|S_{21}|$ data, corresponding sometimes to one, sometimes to the other, and sometimes in between. The R3S resonator data agree more or less with the $|S_{21}|$ data, but the high-frequency point is much higher; in fact, it agrees with the approximate calculations. Perhaps the resonator loss at that point receives a higher contribution from dielectric loss.

Figure 4.21, comparing the parallel data along with MDS and the approximate formulas, is even more interesting. The measured data agrees very well with the MDS numbers. The parallel resonator data agree very well with the $|S_{21}|$ data, again except at the higher frequencies. R3P measurements, though from a different wafer than the line measurements, seem to agree par-

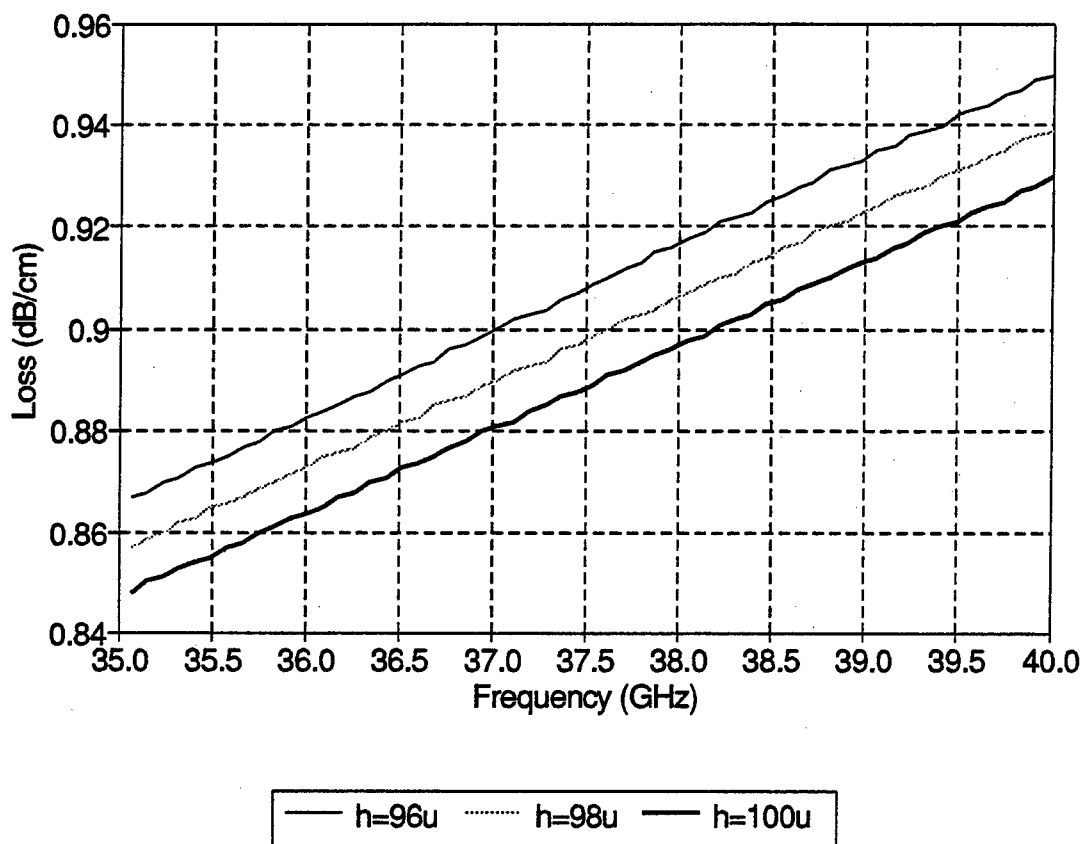


Figure 4.18 Loss calculated with MDS for rms roughness 0.125μ , variable h

ticularly well. R5P data, from the same wafer as the line measurements, agree almost as well. Not just one set of resonator points, but both sets, diverge from MDS and line measurements at the high end and approach the approximate formulas.

Finally, several items emerge after scrutinizing Figure 4.22, especially keeping in mind the previous figure. Except for the conspicuous dip in the 21-25 GHz or so range, $|S_{21}|$ measurements are slightly above the MDS predictions; this is the same as saying that they are generally greater than the parallel groove measurements. This is expected. What is not expected is the dip. Once more, resonator measurements display similar behavior to those in Figure 4.21;

Table 4.4 Goldfarb and Platzker Resonator Data

Frequency (GHz)	α (dB/cm)	Error Bar (dB/cm)
07.5	0.315	0.05
11.0	0.390	0.05
15.0	0.475	0.05
22.5	0.575	0.06
30.0	0.665	0.06
37.5	0.745	0.07

namely, they agree fairly well with the line measurements, although they are slightly higher. R3T measurements from a different wafer, again, agree well with those of R2T and the line data. Still the ones at the higher frequencies are more near the approximate formula calculations than the other measured and MDS data.

One solid conclusion that can be drawn here, at least for relatively thick gold conductors on GaAs substrates which are typical of MMIC's, is that some of the approximate formulas available will overestimate the loss by almost a factor of two at the lower frequencies. Also, MDS will slightly underestimate the loss for smooth conductors and be very good for rough conductors. Of course, GaAs MMIC's will typically have very smooth surfaces, so the smooth behavior of MDS is of more interest in this case.

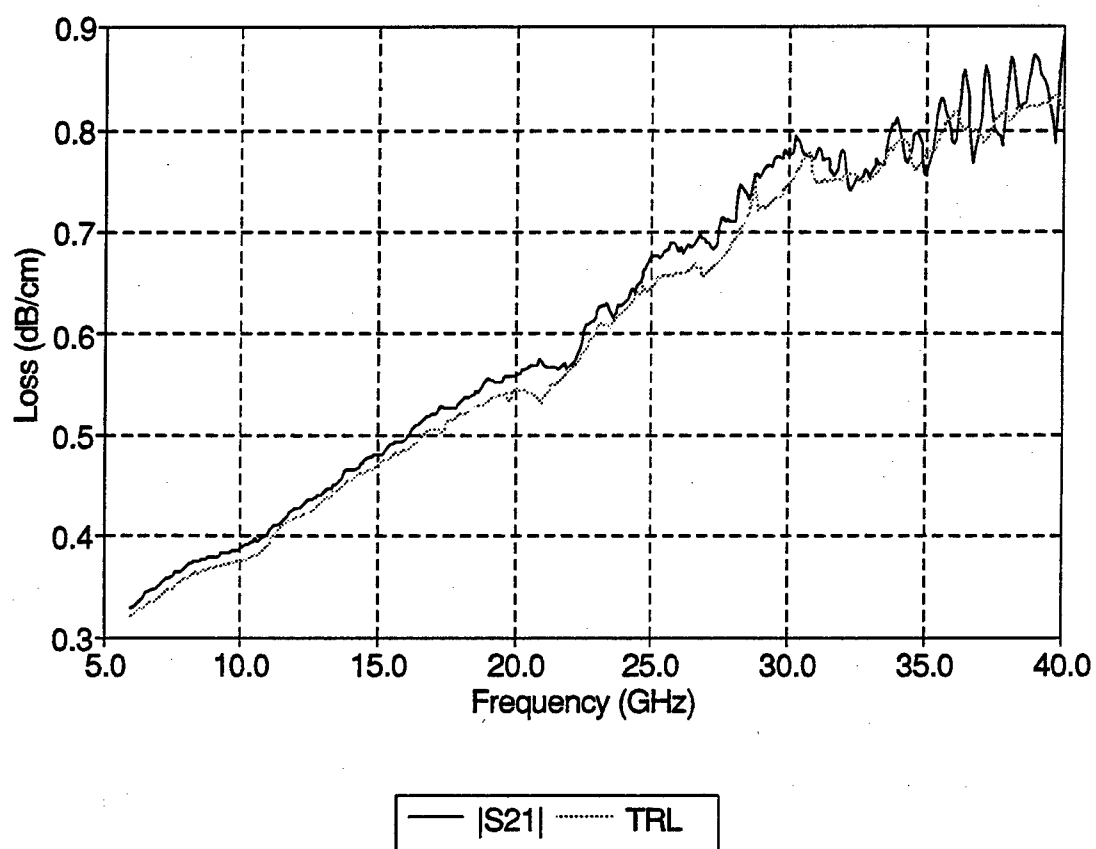


Figure 4.19 Comparison of TRL and S-parameter measured smooth losses

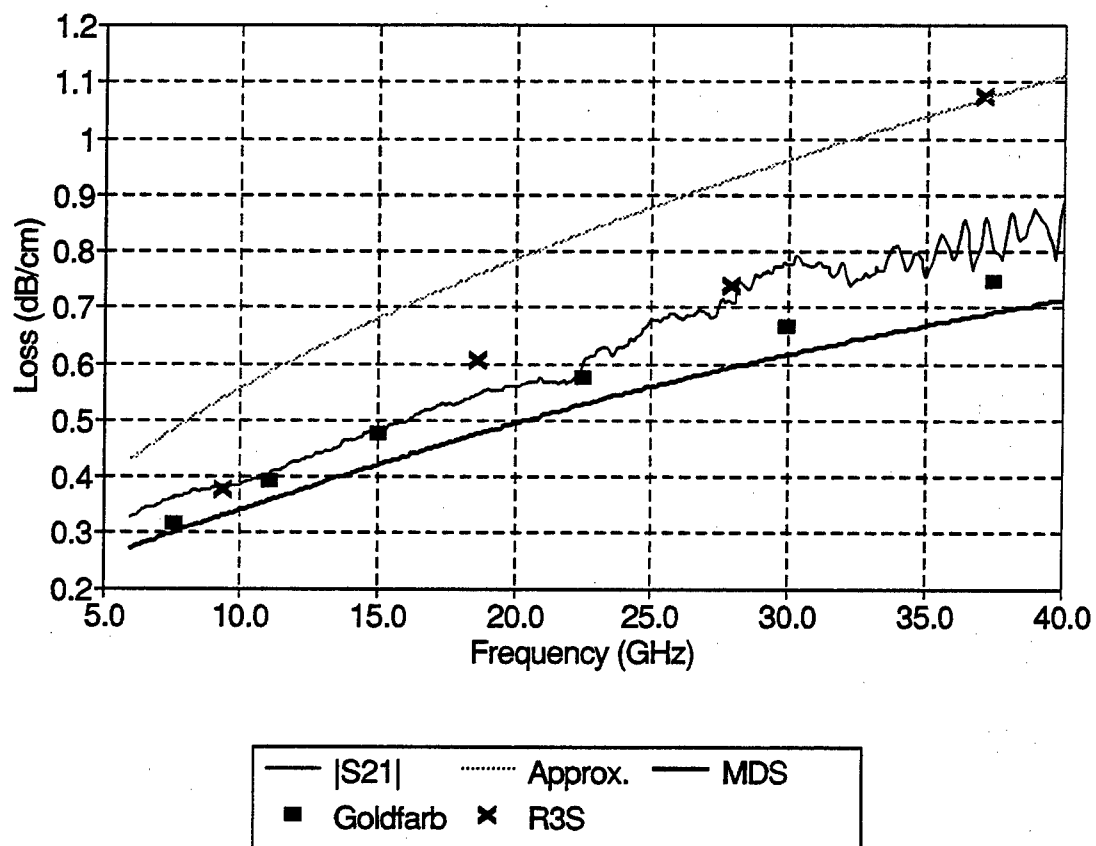


Figure 4.20 Comparison of the measured and calculated smooth losses

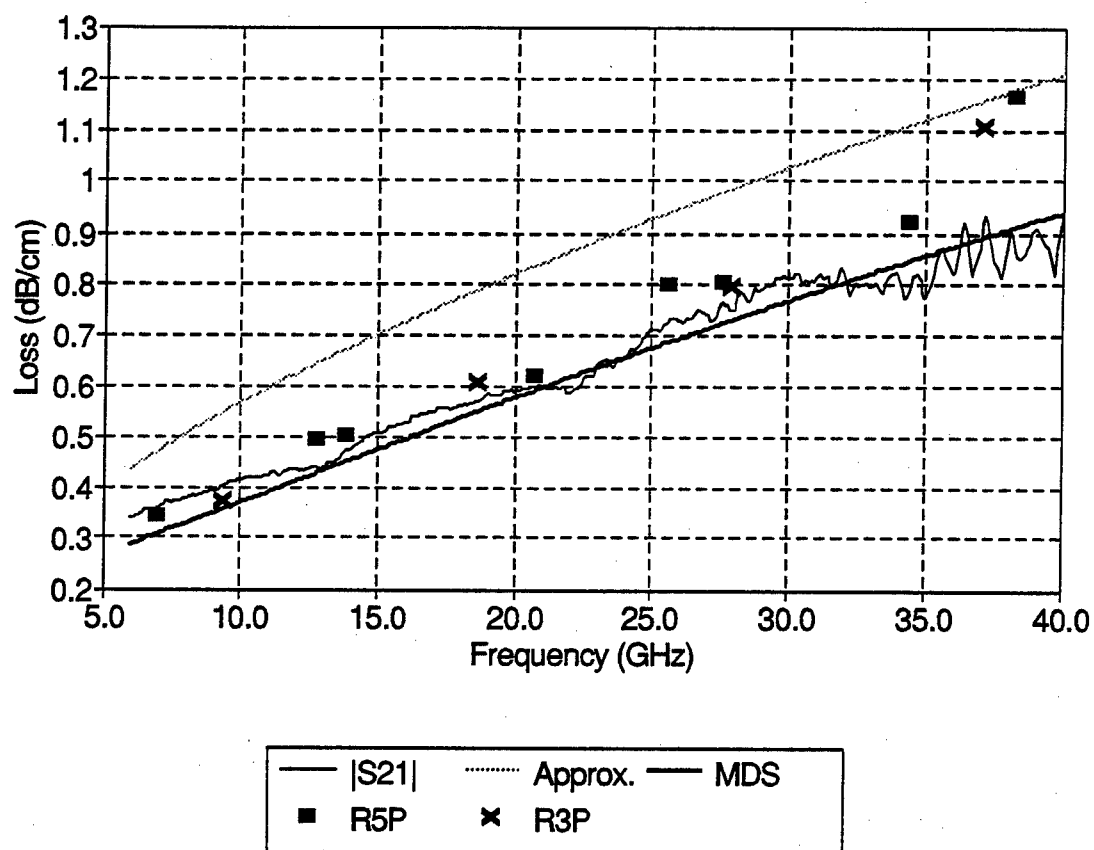


Figure 4.21 Comparison of the measured and calculated parallel losses

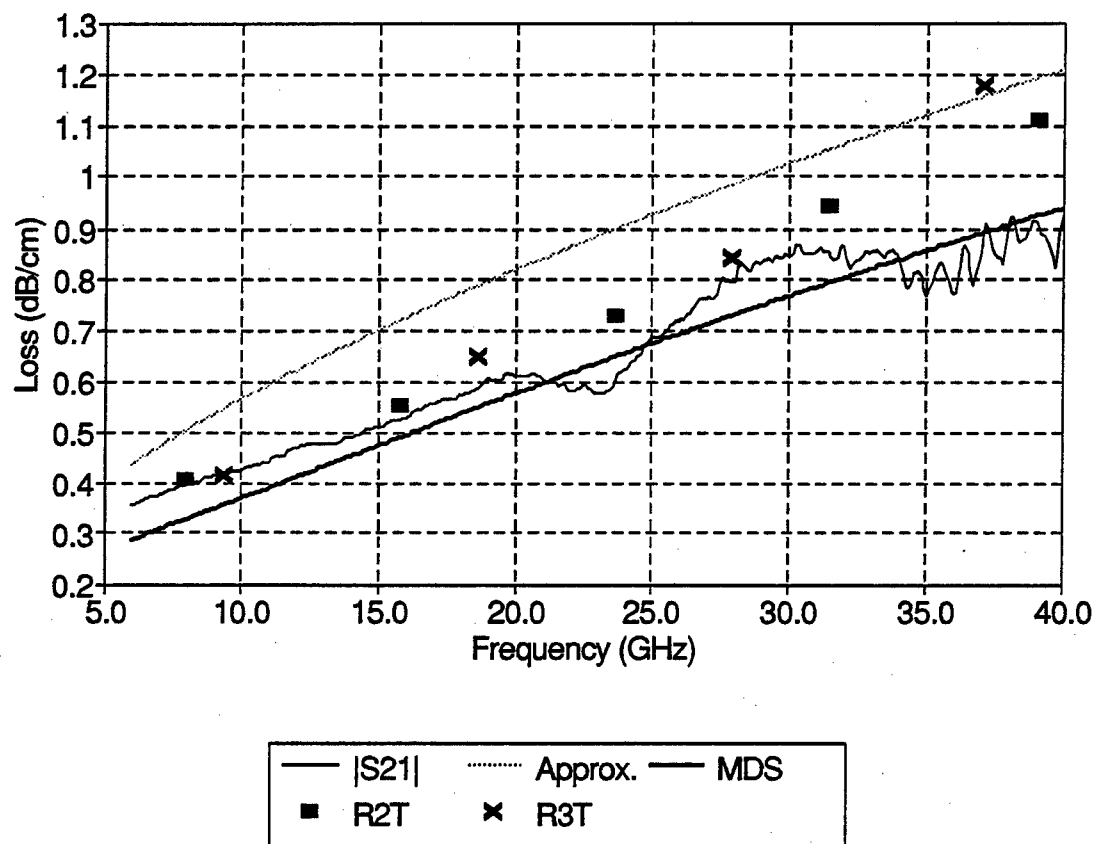


Figure 4.22 Comparison of the measured and calculated transverse losses

CHAPTER V

SOLUTION OF THE INTEGRAL EQUATION FOR THE CURRENT DISTRIBUTION IN A STRIP CONDUCTOR

5.1 Basic integral equation solution technique [44]

Given a homogeneous eigenvalue equation of the form

$$L(f) = \lambda M(f) \quad (5.1)$$

where L and M are operators, allowable λ 's are eigenvalues, and the corresponding solutions f are eigenfunctions, the method of moments can be used to reduce this functional equation to a matrix equation. An inner product definition (f, g) is also required; this inner product is defined to be commutative, associative, and positive definite. The equation (5.1) often arises in physical problems; the eigenvalues correspond to characteristic parameters (such as propagation constants) of these problems.

The general approach to solving (5.1) with a moment method is to choose a set of basis or expansion functions f_1, f_2, f_3, \dots , in the domain of L and M , and expand f in a linear combination of these basis functions:

$$f = \sum_n \alpha_n f_n \quad (5.2)$$

where the α_n are constants. This expansion is substituted into (5.1) and yields

$$\sum_n \alpha_n L(f_n) = \lambda \sum_n \alpha_n M(f_n) \quad (5.3)$$

We take the inner product definition mentioned previously and choose a set of

testing or weighting functions w_1, w_2, w_3, \dots in the range of L and M . If the w_m 's are the same functions as the f_m 's, then this is referred to as Galerkin's method. The inner product of (5.3) is taken with each w_m , giving

$$\sum_n \alpha_n(w_m, Lf_n) = \lambda \sum_n \alpha_n(w_m, Mf_n), \quad \forall m. \quad (5.4)$$

This can be rewritten in matrix form as

$$[l_{mn}][a_n] = \lambda[m_{mn}][a_n] \quad (5.5)$$

The equation (5.5) only has solutions if

$$\det[l_{mn} - \lambda m_{mn}] = 0. \quad (5.6)$$

The determinant is a polynomial in λ whose roots are the eigenvalues of the matrix equation (5.5) and the approximate eigenvalues of the functional equation (5.1).

The operators, of course, can be integral or integro-differential; furthermore, the resulting matrix equation may be a nonlinear eigenvalue equation that only has solutions (which are often difficult to find, [47]) when

$$\det[F(\lambda)] = 0. \quad (5.7)$$

This is the case for the integral equation presented here.

5.2 Problem statement

Figure 5.1 shows the arrangement and coordinate system to which the moment method will be applied. An integral equation which is applicable to this geometry is available [45]. The unknown in this equation is the current distribution in the imperfectly conducting non-zero thickness strip of arbitrary cross section on a perfect dielectric above a perfect ground plane. The objective is to solve for the attenuation constant α for this structure. To simplify matters, the solution will first be carried out for the case of $\epsilon_r = 1$ (air dielectric). Payt [46] has carried out similar work for dielectric waveguide.

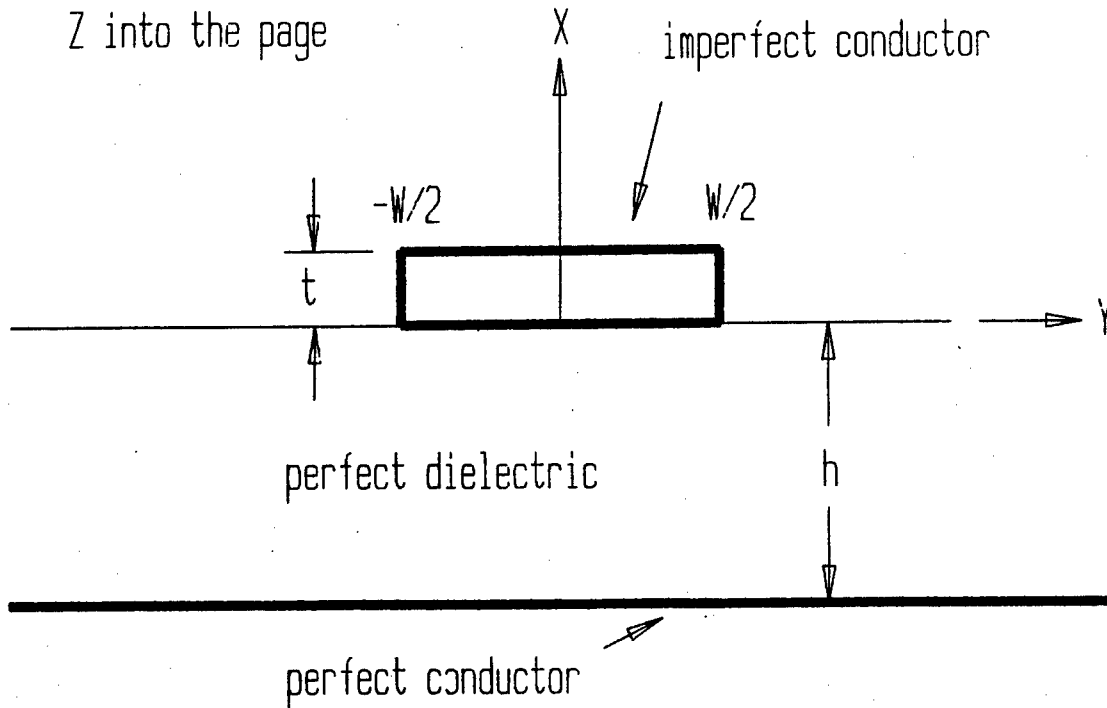


Figure 5.1 Geometry of the microstrip problem

5.3 Air dielectric case (substrate $\epsilon_r = 1$)

5.3.1 Discretization and application of Galerkin's method

The fundamental mode for this structure with air dielectric is given by

$$\bar{E} = \bar{E}(x, y)e^{-\gamma z} \quad \bar{H} = \bar{H}(x, y)e^{-\gamma z}. \quad (5.8)$$

where $\gamma = \alpha + j\beta$ is the propagation constant. This is a TEM mode propagating in the $+z$ direction with phase constant β and attenuation constant α . An integral equation appropriate for this structure is [45]

$$\bar{E} = \frac{1}{j\omega\hat{\epsilon}} (\nabla\nabla \cdot + k_o^2) \int_S [G\bar{J}(x', y') + G_i\bar{J}_i(x', y')] dx' dy' \quad (5.9)$$

where $\bar{E} = \frac{\bar{J}(x, y)}{j\omega(\epsilon_c - \epsilon_o) + \sigma_c}$, ϵ_c and σ_c are the permittivity and conductivity of the conductor, $\hat{\epsilon} = \epsilon_c - j\frac{\sigma_c}{\omega}$, and subscript i indicates imaged quantities. The kernel

is a modified Bessel function of the second kind, such that

$$\begin{aligned}\bar{E} &= (\nabla \nabla \cdot + k_o^2) \frac{1}{2\pi} \int_S (\hat{\epsilon}_r - 1) \bar{E}(\bar{\rho}') K_o(u|\bar{\rho} - \bar{\rho}'|) dS' \\ &+ (\nabla \nabla \cdot + k_o^2) \frac{1}{2\pi} \int_{S_i} (\hat{\epsilon}_r - 1) \bar{E}_i(\bar{\rho}'_i) K_o(u|\bar{\rho} - \bar{\rho}'_i|) dS'\end{aligned}\quad (5.10)$$

where $\hat{\epsilon}_r = \frac{\epsilon_c}{\epsilon_o} - j \frac{\sigma_o}{\omega \epsilon_o}$, $\bar{\rho}' = (x', y')$, $\bar{\rho}'_i = (-x', y')$, $\bar{\rho}' \in S$, and $\bar{\rho}'_i \in S_i$. We have set u equal to $\sqrt{k_o^2 + \gamma^2}$ for convenience.

To solve the integral equation (5.8) we grid the strip conductor of Figure 5.1 into rectangular cells and expand \bar{E} and \bar{E}_i in a finite set of subdomain basis functions where the \bar{f}_m are rectangular pulses which are nonzero only in their respective cells:

$$\bar{E} \cong \sum_{m=1}^M a_m \bar{f}_m(\bar{\rho}); \quad \bar{E}_i \cong \sum_{m=1}^M a_{m_i} \bar{f}_m(\bar{\rho}) \quad (5.11)$$

and let the testing functions also be $\bar{f}_m(\bar{\rho})$. This is therefore a Galerkin technique. Defining the symmetric products

$$(\bar{f}, \bar{g})_S \equiv \int_S \bar{f} \cdot \bar{g} dS; \quad (\bar{f}, \phi)_S \equiv \int_S \bar{f} \phi dS \quad (5.12)$$

and adopting the notation

$$\int_S (\hat{\epsilon}_r - 1) \bar{E} K_o(\quad) dS' = (\bar{E}, (\hat{\epsilon}_r - 1) K_o(\quad))_{S'}, \quad (5.13)$$

we can take the dot product of $\bar{f}_n(\bar{\rho})$ with the equation (5.3) and integrate over S . This yields

$$\begin{aligned}\sum_{m=1}^M a_m (\bar{f}_m, \bar{f}_n)_S &= \frac{1}{2\pi} \sum_{m=1}^M a_m \left\{ (\bar{f}_n, [\nabla \nabla \cdot + k_o^2] [(\hat{\epsilon}_r - 1) \bar{f}_m, K_o(\quad)]_{S'})_S \right\} \\ &+ \frac{1}{2\pi} \sum_{m=1}^M a_{m_i} \left\{ (\bar{f}_n, [\nabla \nabla \cdot + k_o^2] [(\hat{\epsilon}_r - 1) \bar{f}_m, K_o(\quad)]_{S'})_S \right\} \\ \forall \quad n &= 1, \dots, M.\end{aligned}\quad (5.14)$$

For the rectangular basis functions \bar{f}_m and \bar{f}_n , it is obvious that

$$(\bar{f}_m, \bar{f}_n)_S = \delta_{mn} \cdot \text{area of rectangular cell} \equiv \delta_{mn} A_p. \quad (5.15)$$

The double surface integrals in (5.14) are now converted into double contour integrals. For brevity we will examine the nonimaged (subscript m) portion only. We begin with

$$\int_S \bar{f}_n \cdot \left\{ (\nabla \nabla \cdot + k_o^2) \int_S (\hat{\epsilon}_r - 1) \bar{f}_m K_o(u|\bar{\rho} - \bar{\rho}'|) dS' \right\} dS \quad (5.16)$$

and let $K \equiv (\hat{\epsilon}_r - 1) K_o(u|\bar{\rho} - \bar{\rho}'|)$. Then we can write

$$\begin{aligned} & \int_S \bar{f}_n \cdot \left\{ (\nabla \nabla \cdot + k_o^2) \int_S K \bar{f}_m dS' \right\} dS \\ &= \int_S \left[\nabla \nabla \cdot \int_S K_o() f_m dS' \right] \cdot \bar{f}_n dS + \int_S \left[k_o^2 \int_S K_o() f_m dS' \right] \cdot \bar{f}_n dS \\ &\equiv A + B. \end{aligned} \quad (5.17)$$

Now

$$A = \int_S \nabla \left[\int_S \nabla \cdot K \bar{f}_m dS' \right] \cdot \bar{f}_n dS = \int_S \nabla \left[\oint_C K(\bar{f}_m \cdot \bar{n}') dl' \right] \cdot \bar{f}_n dS \quad (5.18)$$

by direct application of Stokes' Theorem to the integral inside the brackets.

Consider next the vector identity

$$\nabla \cdot (\phi \bar{D}) = \bar{D} \cdot \nabla \phi + \phi \nabla \cdot \bar{D} \quad (5.19)$$

and let

$$\phi = \oint_C K \bar{f}_m \cdot \bar{n}' dl'. \quad (5.20)$$

Here $\nabla \cdot \bar{D} = \nabla \cdot \bar{f}_n$, but \bar{f}_n is a rectangular pulse. In the sense of generalized functions, $\nabla \cdot \bar{f}_n$ is a delta function at the left side of the pulse and a negative delta function at the right side; as this is inside a surface integral, we can (inside the integral) let $\bar{D} \cdot \nabla \phi = \nabla \cdot (\phi \bar{D})$ (since the integral of the delta functions is

zero) or

$$\begin{aligned}
 A &= \int_S \nabla \left[\oint_C K(\bar{f}_m \cdot \bar{n}') dl' \right] \cdot \bar{f}_n dS \\
 &= \int_S \nabla \cdot \left[\bar{f}_n \oint_C K(\bar{f}_m \cdot \bar{n}') dl' \right] dS \\
 &= \oint_C \left[\bar{f}_n \oint_C K(\bar{f}_m \cdot \bar{n}') dl' \right] \cdot \bar{n} dl \\
 &= \oint_C \oint_C K(\bar{f}_m \cdot \bar{n}') (\bar{f}_n \cdot \bar{n}) dl' dl. \tag{5.21}
 \end{aligned}$$

Now for the B portion of the integral. Since K is a Green's function, it satisfies the Helmholtz equation and we have

$$\begin{aligned}
 (\nabla^2 + k_o^2)K_o(u|\bar{\rho} - \bar{\rho}'|) &= (\nabla_t^2 + k_o^2 + \gamma^2)K_o(u|\bar{\rho} - \bar{\rho}'|) \\
 &= (\nabla_t^2 + u^2)K_o(u|\bar{\rho} - \bar{\rho}'|) \\
 &= -2\pi \delta(\bar{\rho} - \bar{\rho}'); \tag{5.22}
 \end{aligned}$$

therefore

$$\begin{aligned}
 u^2 K_o(u|\bar{\rho} - \bar{\rho}'|) &= -2\pi \delta(\bar{\rho} - \bar{\rho}') - \nabla_t^2 K_o(u|\bar{\rho} - \bar{\rho}'|) \Rightarrow \\
 k_o^2 K_o(u|\bar{\rho} - \bar{\rho}'|) &= -\frac{k_o^2}{u^2} [+2\pi \delta(\bar{\rho} - \bar{\rho}') + \nabla_t^2 K_o(u|\bar{\rho} - \bar{\rho}'|)] \tag{5.23}
 \end{aligned}$$

Then

$$B = -\frac{k_o^2}{u^2} \int_S \left[\int_S (2\pi \delta(\bar{\rho} - \bar{\rho}') + \nabla_t^2 K) \bar{f}_m dS' \right] \cdot \bar{f}_n dS. \tag{5.24}$$

The delta function portion of this integral is straightforward:

$$\int_S \left[\int_S 2\pi \delta(\bar{\rho} - \bar{\rho}') \bar{f}_m dS' \right] \cdot \bar{f}_n dS = 2\pi \bar{f}_m \cdot \bar{f}_n|_{\rho=\rho'} = 2\pi \delta_{mn} \tag{5.25}$$

where δ_{mn} is the Kronecker delta. The second part of this integral is

$$\begin{aligned}
 \int_S \left[\int_S (\nabla_t^2 K) \bar{f}_m dS' \right] \cdot \bar{f}_n dS &= \int_S \nabla_t \cdot \left[\int_S (\nabla_t K) \cdot \bar{f}_m dS' \right] \bar{f}_n dS \\
 &= \oint_C \left[\int_S (\nabla_t K) \cdot \bar{f}_m dS' \right] (\bar{f}_n \cdot \bar{n}) dl. \tag{5.26}
 \end{aligned}$$

We make use of the vector identity

$$(\nabla_t K) \cdot \bar{f}_m = \nabla_t \cdot K \bar{f}_m - K \nabla \cdot \bar{f}_m \quad (5.27)$$

as before, so that within the integral $\nabla \cdot \bar{f}_m$ vanishes. We rewrite the integral as

$$\begin{aligned} \oint_C \left[\int_S \nabla_t \cdot K \bar{f}_m dS' \right] (\bar{f}_n \cdot \bar{n}) dl &= \oint_C \left[\oint_C K \bar{f}_m \cdot \bar{n}' dl' \right] (\bar{f}_n \cdot \bar{n}) dl \\ &= \oint_C \oint_C K (\bar{f}_m \cdot \bar{n}') (\bar{f}_n \cdot \bar{n}) dl' dl. \end{aligned} \quad (5.28)$$

Finally,

$$B = -\frac{k_o^2}{u^2} \left[2\pi \delta_{mn} + \oint_C \oint_C K (\bar{f}_m \cdot \bar{n}') (\bar{f}_n \cdot \bar{n}) dl' dl \right] \quad (5.29)$$

Therefore

$$A + B = -\frac{k_o^2}{u^2} 2\pi \delta_{mn} + \frac{\gamma^2}{u^2} \oint_C \oint_C (\hat{\epsilon}_r - 1) K_o(u|\bar{\rho} - \bar{\rho}'|) (\bar{f}_m \cdot \bar{n}') (\bar{f}_n \cdot \bar{n}) dl' dl \quad (5.30)$$

We can now write the whole equation as

$$\begin{aligned} \sum_{m=1}^M &-a_m A_p \delta_{mn} + (a_m + a_{mi}) \left(-\frac{k_o^2}{u^2} \delta_{mn} \right) \\ &+ a_m \frac{\gamma^2}{2\pi u^2} \oint_C \oint_C (\hat{\epsilon}_r - 1) K_o(u|\bar{\rho} - \bar{\rho}'|) (\bar{f}_m \cdot \bar{n}') (\bar{f}_n \cdot \bar{n}) dl' dl \\ &- a_{mi} \frac{\gamma^2}{2\pi u^2} \oint_C \oint_C (\hat{\epsilon}_r - 1) K_o(u|\bar{\rho} - \bar{\rho}'_i|) (\bar{f}_m \cdot \bar{n}') (\bar{f}_n \cdot \bar{n}) dl' dl \\ &= 0 \quad \forall n = 1, \dots, M \end{aligned} \quad (5.31)$$

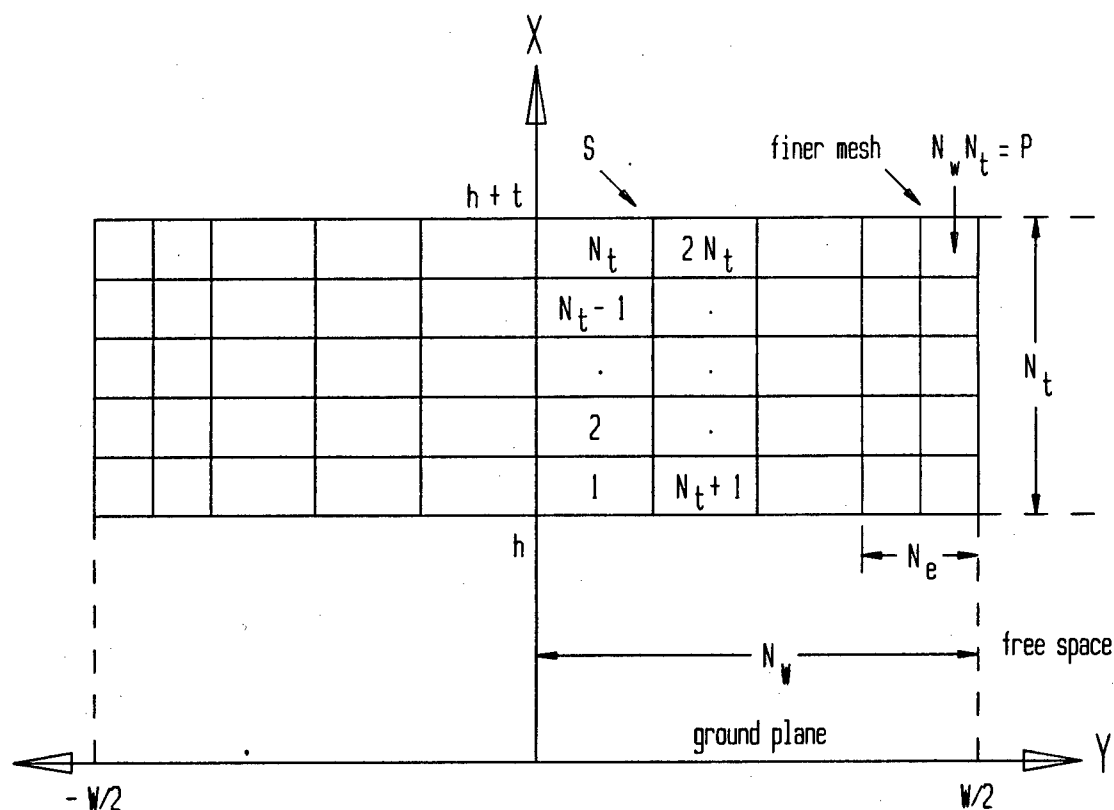


Figure 5.2 Discretization of the strip into a mesh of rectangular cells

5.3.2 Computer implementation

Figure 5.2 shows how the strip-conductor was gridded up into a mesh of rectangular cells. The cells at the extreme edges of the conductor are square; this allows more precise representation of the current singularity at the edges. Table 5.1 lists the basis function definitions, while Table 5.2 contains the dot product evaluations for the contours shown in Figure 5.3. These dot products are the $(\bar{f}_m \cdot \bar{n}')$ and $(\bar{f}_n \cdot \bar{n})$ terms from Equation (5.31). Restricting the cells to being rectangular keeps the dot product terms simple; one only needs to know the relative directions to know the sign, whereas only parallel edges give

Table 5.1 Basis function definitions

-
- There are P rectangular, nonuniform cells
 - $P = N_w \cdot N_t$
 - There are $M = 3P$ basis functions (3 per cell: x, y, z parts).
 - The rectangular basis functions are defined as follows:

$$\bar{f}_{3p-2} = \hat{a}_x, \quad \bar{\rho} \in \text{cell } p$$

$$\bar{f}_{3p-1} = \hat{a}_y, \quad \bar{\rho} \in \text{cell } p$$

$$\bar{f}_{3p} = \hat{a}_z, \quad \bar{\rho} \in \text{cell } p$$

$$\bar{f}_m = 0, \quad \text{otherwise}$$

nonzero contributions

The image plane (Y axis) gives the following symmetry relations:

$$E_{x_i}|_{(-x',y')} = E_x|_{(x',y')}$$

$$E_{y_i}|_{(-x',y')} = -E_y|_{(x',y')}$$

$$E_{z_i}|_{(-x',y')} = -E_z|_{(x',y')}$$

These relations let us convert the a_{m_i} terms in Equation (5.31) to their corresponding a_m terms, thus rendering the unknown current (or electric field) distribution vector in a_m entirely.

It is important to note that when the primed and unprimed coordinates are a common cell, edge, or vertex, special measures must be taken. In these cases the arguments of the modified Bessel functions can be zero over part of the range of integration, and K_0 has a singularity for zero argument. In fact,

Table 5.2 Dot product evaluations

$$\bar{f}_m \cdot \bar{n}' = 0 \text{ when } \bar{f}_m \text{ or } \bar{n}' = \hat{z}$$

$$\bar{f}_n \cdot \bar{n} = 0 \text{ when } \bar{f}_n \text{ or } \bar{n} = \hat{z}$$

$$\text{When } \bar{f}_m = \hat{x} \Rightarrow \text{MOD}(m, 3) = 1$$

$$\bar{f}_m \cdot \bar{n}' = \begin{cases} 1, & \text{if } dl' = -dy' \Rightarrow dl'_{3-4} \\ -1, & \text{if } dl' = dy' \Rightarrow dl'_{1-2} \\ 0, & \text{other two sides.} \end{cases}$$

$$\bar{f}_n \cdot \bar{n} = \begin{cases} 1, & \text{if } dl = -dy \Rightarrow dl_{3-4} \\ -1, & \text{if } dl = dy \Rightarrow dl_{1-2} \\ 0, & \text{other two sides.} \end{cases}$$

$$\text{When } \bar{f}_m = \hat{y} \Rightarrow \text{MOD}(m, 3) = 2$$

$$\bar{f}_m \cdot \bar{n}' = \begin{cases} 1, & \text{if } dl' = dx' \Rightarrow dl'_{2-3} \\ -1, & \text{if } dl' = -dx' \Rightarrow dl'_{4-1} \\ 0, & \text{other two sides.} \end{cases}$$

$$\bar{f}_n \cdot \bar{n} = \begin{cases} 1, & \text{if } dl = dx \Rightarrow dl_{2-3} \\ -1, & \text{if } dl = -dx \Rightarrow dl_{4-1} \\ 0, & \text{other two sides.} \end{cases}$$

$$\text{When } \bar{f}_m = \hat{z} \Rightarrow \text{MOD}(m, 3) = 3$$

$$\bar{f}_m \cdot \bar{n}' = 0$$

$$\bar{f}_n \cdot \bar{n} = 0$$

Note: dl' runs over the entire conductor, whereas dl runs over the current cell.

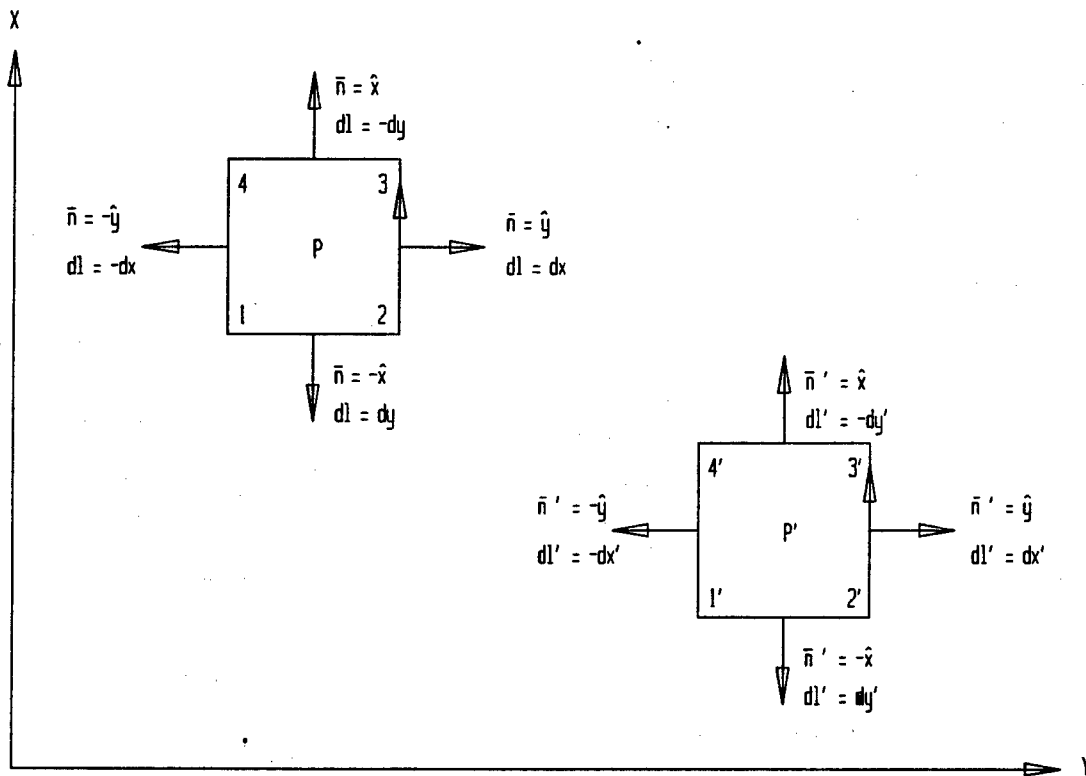


Figure 5.3 Nomenclature for evaluation of the contour integrals for primed and unprimed cells

the small argument form of this function is

$$K_0(z) \rightarrow -\ln\left(\frac{z}{2}\right) - \gamma \quad \text{as} \quad z \rightarrow 0 \quad (5.32)$$

where this γ is Euler's constant. Any numerical integration scheme which tries to evaluate this function with a zero argument will fail; however, this is an integrable singularity [48, 49]. All of the special cases (shared edges and shared vertices for various integration directions) were performed, and the results are all various combinations of logarithmic functions of various cell dimensions. For the case in which an edge is shared and integration for both segments is in the

same direction, the following integral results:

$$\int_a^b \int_a^b \ln |x - x'| dx dx' = (b - a)^2 \left[\ln |b - a| - \frac{3}{2} \right]. \quad (5.33)$$

For the case of a shared vertex (and colinear segments) and integration in the same direction, this integral is required:

$$\begin{aligned} \int_a^b \int_b^c \ln |x - x'| dx dx' = & -\frac{1}{2}(b - a)^2 \ln |b - a| - \frac{1}{2}(c - b)^2 \ln |c - b| \\ & + \frac{1}{2}(c - a)^2 \ln |c - a| + \frac{3}{2}(c - b)(b - a). \end{aligned} \quad (5.34)$$

When one of the segments is integrated in the opposite direction, the resulting integrals are simply the negative of those in (5.33) and (5.34).

The code for the air dielectric case was written and apparently works, but incompatible compiler/operating system versions at my computer site prevented me from getting results in time to include in this paper. Work on that item is proceeding separately.

5.4 Perfect dielectric case (substrate $\epsilon_r \geq 1$)

There was not enough time to fully address this case. The main difference between this case and the air dielectric case is that the Green's function is different. It now involves Sommerfeld integrals instead of contour integrals; this is a result of having a source over an infinite dielectric.

CHAPTER VI

CONCLUSIONS

This dissertation contains the results of work carried out both at the University of Colorado at Boulder and at the Avionics Laboratory at Wright-Patterson Air Force Base in Dayton, Ohio. This work involved fabricating gold-on-GaAs microstrip lines with tightly controlled surface roughness and cross sectional area, as well as making careful on-wafer measurements of these lines attenuation constants. More work was performed on the solution of an integral equation which can be used to calculate loss; however, this particular equation is not usually used for this purpose since applying the method of moments yields a nonlinear complex eigenvalue problem. The complex eigenvalues are the complex propagation constants for the modes which may exist on the line. We were only interested in the dominant mode.

Much work was expended in developing and characterizing the process used to fabricate the passive MMIC's for this project. Many of the techniques could be used here at the University of Colorado with minor changes in the way things are done now. Making these changes and documenting the procedures would, I believe, greatly improve any in-house processing of GaAs which might be carried out here. I hope that this document is the start of such improvement.

Much work was also expended in setting up the measurement system here at the University of Colorado and in getting good, useful data from this system. This work has helped provide the university with the ability to make on-wafer measurements of both passive and biased active devices up to 49 GHz.

Again, many of these details and procedures are outlined in this work, and it will hopefully be a useful guide to those who come later. The use of on-wafer TRL calibration and the standards thereof are also discussed in some detail. The data collected and presented show that this system can make good measurements. Some work on computing and characterizing the effects of different errors on the TRL calibration needs to be done. In hindsight, I believe that work expended on the integral equation solution would have been more logically spent on a thorough error analysis of the effects of real-world variations on TRL calibrations: effects such as via hole variation, nonuniform substrate height, and differences in probing are not going to go away and must be accounted for.

Finally, work was started on the integral equation solution. Working code was written for the air dielectric case, but a compiler problem on my computer system prevented running the code enough to get results to include in this dissertation.

BIBLIOGRAPHY

- [1] R. A. Pucel, D. J. Massé and C. P. Hartwig, "Losses in Microstrip," **IEEE Trans. Microwave Theory Tech.**, Vol. 12, No. 6, pp. 342-350, 1968.
- [2] Marc E. Goldfarb and Aryeh Platzker, "Losses in GaAs Microstrip," **IEEE Trans. Microwave Theory Tech.** Vol. 38, No. 12, Dec. 1990.
- [3] Brian C. Wadell, **Transmission Line Design Handbook**. Artech House, Inc., Norwood, MA, 1991.
- [4] Christopher L. Holloway, "Edge and Surface Shape Effects of Conductor Loss Associated with Planar Circuits," **MIMICAD Technical Report No. 12**, University of Colorado, Boulder, CO, April 1992.
- [5] Terry Edwards, **Foundations for Microstrip Circuit Design, Second Edition**. John Wiley & Sons, New York, NY, 1992.
- [6] Tony Leung and Constantine A. Balanis, "Attenuation Distortion of Transient Signals in Microstrip," **IEEE Trans. Microwave Theory Tech.**, Vol. 36, No. 4, April 1988.
- [7] Robert R. Romanofsky, "Analytical and Experimental Procedures for Determining Propagation Characteristics of Millimeter-Wave Gallium Arsenide Microstrip Lines," **NASA Technical Paper 2899**, Lewis Research Center, 1989.
- [8] Samuel Y. Liao, **Microwave Circuit Analysis and Amplifier Design**. Prentice-Hall, Inc., Englewood Cliffs, NJ, 1987.
- [9] Robert E. Collin, **Foundations for Microwave Circuit Design**. McGraw Hill Book Co., New York, NY, 1966.
- [10] **Design Guide for PFTE-Based Circuit Boards**, Rogers Corporation, Soladyne Division.
- [11] G. J. Hill, "Alumina for Microwave Substrates," **High Frequency Dielectric Measurement**, pp. 127-134.
- [12] R. K. Hoffman, **Handbook of Microwave Integrated Circuits**. Artech House, Inc., Norwood, MA, 1987.
- [13] Thomas S. Laverghetta, **Practical Microwaves**. Howard W. Sams & Co., Inc., Indianapolis, IN, 1984.
- [14] **Trans-Strates Microwave Substrates**, Trans-Tech, Inc.

- [15] **Metallization Bulletin**, Trans-Tech. Inc.
- [16] James D. Woermbke, "Soft Substrates Conquer Hard Designs," **Microwaves**, Jan. 1982.
- [17] Samuel P. Morgan, Jr., "Effect of Surface Roughness on Eddy Current Losses at Microwave Frequencies," **Journal of Applied Physics**, Vol. 20, April 1949, pp. 352-362.
- [18] Ralph E. Williams, **Gallium Arsenide Processing Techniques**. Artech House, Inc., Dedham, MA, 1984.
- [19] Dylan Williams, Tom H. Miers, "A Coplanar Probe to Microstrip Transition", **IEEE Trans. Microwave Theory Tech.**, Vol. 36, No. 7, July 1988, pp. 1219-1223.
- [20] Doug Rytting, "An Analysis of Vector Measurement Accuracy Enhancement Techniques," **RF & Microwave Measurement Symposium and Exhibition**, date unknown.
- [21] **Network Analysis: Applying the HP8510B TRL Calibration for Non-Coaxial Measurements**, Hewlett-Packard Product Note 8510-8
- [22] Ronald F. Bauer and Paul Penfield, Jr., "De-Embedding and Unterminating," **IEEE Trans. Microwave Theory Tech.**, Vol. 22, No. 3, March 1974, pp. 282-288.
- [23] Jamal S. Izadian and Shahin M. Izadian, **Microwave Transition Design**. Artech House, Inc., Norwood, MA, 1988.
- [24] G. F. Engen and C. A. Hoer, "Thru-Reflect-Line: An Improved Technique for Calibrating the Dual Six-Port Network Analyzer," **IEEE Trans. Microwave Theory Tech.**, Vol. 27, No. 12, Dec. 1979, pp. 987-993.
- [25] Stephen Lantzenhiser, Andrew Davidson, and Keith Jones, "Improve Accuracy of On-Wafer Tests Via LRM Calibration," **Microwaves & RF**, Jan. 1990, pp. 105-109.
- [26] David Rubin, "De-Embedding mm-Wave MIC's with TRL," **Microwave Journal**, June 1990, pp. 141-150.
- [27] Renato R. Pantoja, Michael J. Howes, John R. Richardson, Roger D. Pollard, "Improved Calibration and Measurement of the Scattering Parameters of Microwave Integrated Circuits," **IEEE Trans. Microwave Theory Tech.**, Vol. 37, No. 11, Nov. 1989, pp. 1675-1680.
- [28] Richard Lane, "De-Embedding Device Scattering Parameters," **Microwave Journal**, Aug. 1984, pp. 149-156.
- [29] Joseph Staudinger and Warren Seely, "MMIC Tests Improved with Standards on Chip," **Microwaves & RF**, Feb. 1987, pp. 107-114.
- [30] Dale E. Carlton, K. Reed Gleason, and Eric W. Strid, "Microwave Wafer

Probing," **Microwave Journal**, 1985.

- [31] C. Woodlin and M. Goff, "Verification of MMIC On-Wafer Microstrip TRL Calibration," **IEEE Trans. Microwave Theory Tech. Symposium Digest**, 1990.
- [32] Mario A. Maury, Jr., Steven L. March, and Gary R. Simpson, "LRL Calibration of Automatic Network Analyzers," **Microwave Journal**, May 1987, pp. 387-392.
- [33] Eric W. Strid, "26 GHz Wafer Probing for MMIC Development and Manufacture", **Microwave Journal**, Aug. 1986, pp. 71-82.
- [34] James C. Rautio, "A Possible Source of Error in On-Wafer Calibration," **34th Automatic RF Techniques Group Conference Digest**, Ft. Lauderdale, FL, Nov. 30-Dec. 1, 1989, pp. 118-126.
- [35] Roger B. Marks and Kurt Phillips, "Wafer-Level ANA Calibrations at NIST," **34th Automatic RF Techniques Group Conference Digest**, Ft. Lauderdale, FL, Nov. 30-Dec. 1, 1989, pp. 11-25.
- [36] Roger B. Marks, "Multi-Line Calibration for MMIC Measurement," **36th Automatic RF Techniques Group Conference Digest**, Monterey, CA, Nov. 29-30, 1990, pp. 47-56.
- [37] Roger B. Marks, "A Multiline Method of Network Analyzer Calibration," **IEEE Trans. Microwave Theory Tech.**, Vol. 39, No. 7, July 1991, pp. 1205-1215.
- [38] Jeff Raggio, "Results of a Multi-Site Round-Robin to Examine Probed Measurements of an Impedance Standard Substrate," **IEEE Trans. Microwave Theory Tech.**, Vol. 19, No. 16, Dec. 1990, pp. 962-963.
- [39] M. C. Sanchez, E. Martin, and J. M. Zamarro, "Unified and Simplified Treatment of Techniques for Characterizing Transmission, Reflection or Absorption Resonators," **IEE Proceedings**, Vol. 137, Pt. H, No. 4, Aug. 1990.
- [40] R. D. Poshusta, "Spreadsheet Error Analysis of Least-Squares Fitted Models Using Monte Carlo Simulation," **Computers in Physics**, March-April 1991.
- [41] Philip R. Bevington, **Data Reduction and Error Analysis for the Physical Sciences**. McGraw-Hill Book Company, New York, NY, 1969.
- [42] William J. Diamond, **Practical Experiment Designs for Engineers and Scientists**. Lifelong Learning Publications, Belmont, CA, 1981.
- [43] Brad Brim, Hewlett-Packard Co., personal communication.
- [44] Roger F. Harrington, **Field Computation by Moment Methods**. Rober E. Krieger Publishing Co., Malabar, FL, 1968.

- [45] Edward F. Kuester and David B. Seidel, "Low-Frequency Behavior of the Propagation Constant Along a Thin Wire in an Arbitrarily Shaped Mine Tunnel," **IEEE Trans. Microwave Theory Tech.**, Vol. 27, No. 8, Aug. 1979, pp. 736-741.
- [46] Ronald C. Payt, "Solution of Fundamental Propagation Modes on Dielectric Waveguide of Arbitrary Cross Section," MS Thesis, Department of Electrical Engineering, University of Colorado, Boulder, CO, 1979.
- [47] Ed. by Tatsuo Itoh. **Numerical Techniques for Microwave and Millimeter-Wave Passive Structures**. John Wiley & Sons, Inc., New York, NY, 1989.
- [48] Ed. by Eikichi Yamashita. **Analysis Methods for Electromagnetic Wave Problems**. Artech House, Norwood, MA, 1990.
- [49] Constatine A. Balanis. **Advanced Engineering Electromagnetics**. John Wiley & Sons, Inc., New York, NY, 1989.
- [50] Jean-Fu Kiang, "Integral Equation Solution to the Skin Effect Problem in Conductor Strips of Finite Thickness," **IEEE Trans. Microwave Theory Tech.**, Vol. 39, No. 3, March 1991, pp. 452-460.
- [51] Franco Giannini. Claudio Paoloni. Marina Ruggieri. "CAD-Oriented Models for Lossy Stubs," **IEEE Trans. Microwave Theory Tech.**, Vol. 36, No. 2., pp. 305-312.
- [52] Steven L. March, "Analyzing Lossy Radial-Line Stubs," **IEEE Trans. Microwave Theory Tech.**, Vol. 33, No. 3., March 1985, pp. 269-271.
- [53] Harry A. Atwater, "Microstrip Reactive Circuit Elements," **IEEE Trans. Microwave Theory Tech.**, Vol. 31, No. 6, June 1983, pp. 488-491.

APPENDIX A

INITIAL WAFERS

A.1 Non-via-hole coplanar-to-microstrip transition

At the start of this research there was a lack of processing experience. Therefore the decision was made to use a coplanar probe to microstrip transition (Figure A.1) that does not require via holes [19], therefore saving one mask and two processing steps (via lithography and via etch). This transition is a radial stub whose dimensions are selected so that its impedance to (microstrip) ground is minimized over a certain frequency range. Of course the ground contacts of the probe make contact with this stub, and the center conductor of the coplanar waveguide contacts the microstrip line proper.

There are three major drawbacks, though. First, the structure will not have a constant impedance. Figures A.2 and A.3 show the theoretical impedance of the transitions used in the first two wafer designs. Second, these structures consume large amounts of area on the wafer. Due to the dependence of dimensions on frequency, lower frequencies require prohibitively large stubs. Increasing substrate height h also increases size. Third, by their very nature these transitions are resonant or near-resonant structures. If one is trying to measure loss and/or measure resonator responses, then there may be difficulties due to these extra resonances in the measurement path. Calibration, however, should remove concern for the first effect and remove or reduce concern for the third effect. The second effect is a physical phenomenon and must simply be tolerated as an engineering tradeoff for not having to do via hole processing.

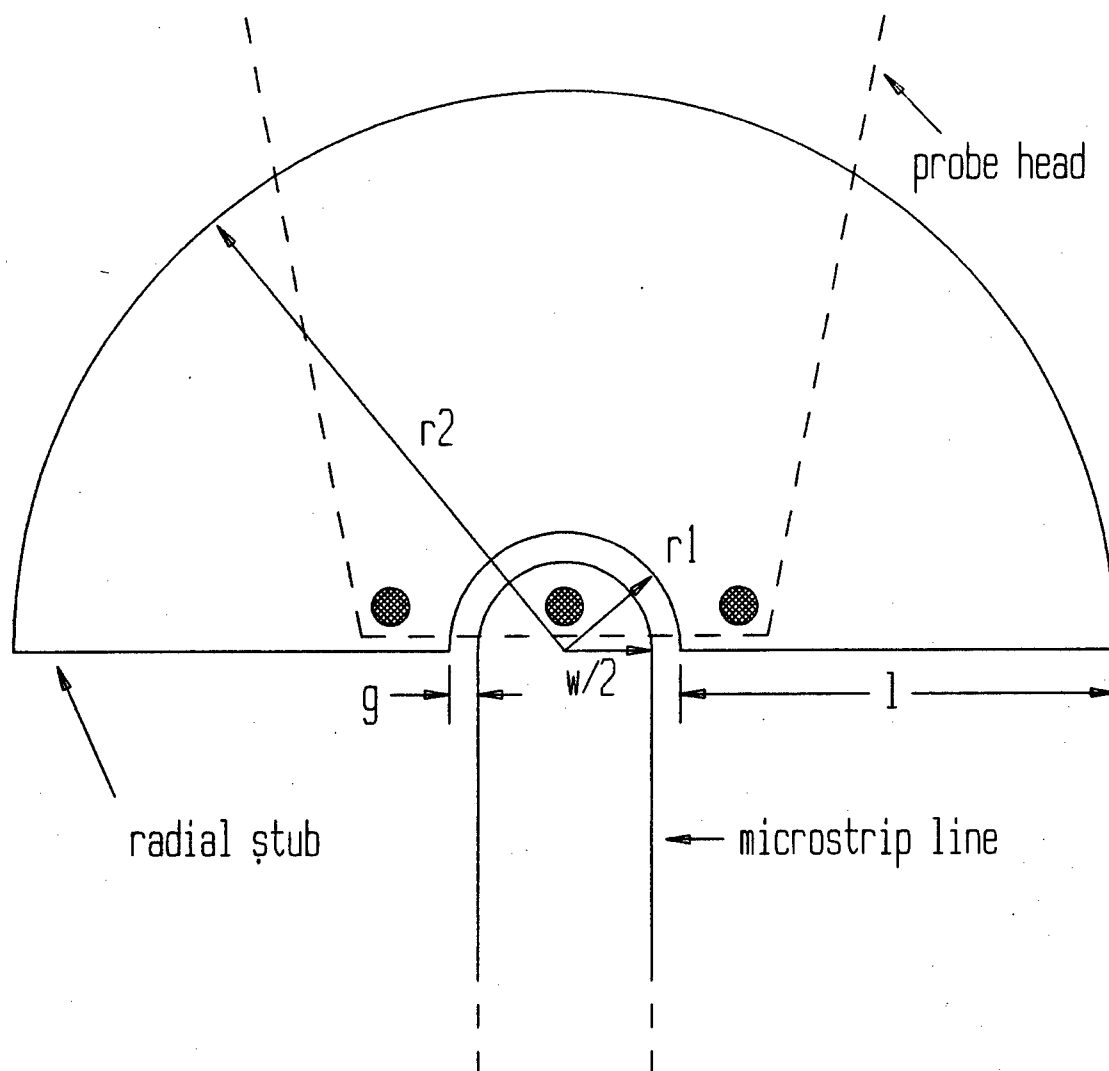


Figure A.1 Coplanar probe to microstrip transition without vias

For completeness the design equations as derived in the reference [51-53] are presented below. The dimensions refer to those shown in Figure A.1, and X is the reactance of the stub.

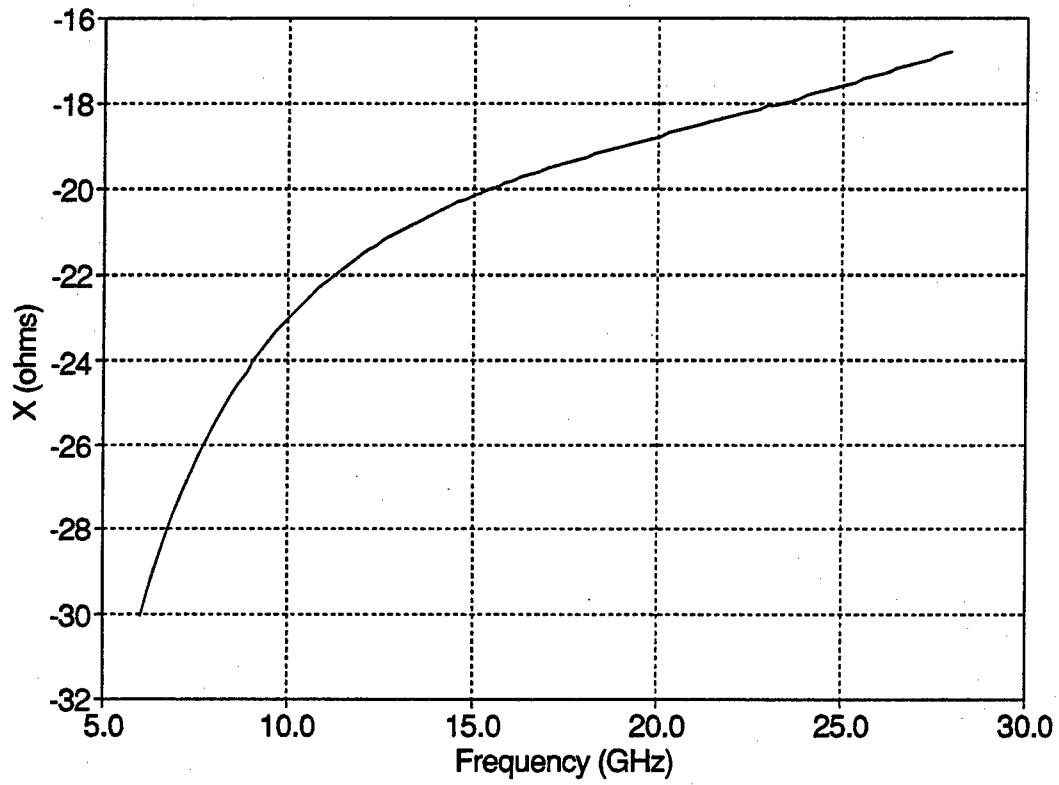


Figure A.2 Impedance of non-via-hole coplanar transition for first wafer design

$$X = \frac{h}{r_1} Z_o(r_1) \frac{1}{\pi} \frac{\cos(\theta_1 - \Phi_2)}{\sin(\Phi_1 - \Phi_2)} \quad (\text{A.1.1})$$

where

$$\theta_1 = \tan^{-1} \left[\frac{N_o(kr_1)}{J_o(kr_1)} \right] \quad (\text{A.1.2.a})$$

$$\Phi_i = \tan^{-1} \left[\frac{J_1(kr_i)}{N_1(kr_i)} \right] \quad (i = 1, 2) \quad (\text{A.1.2.b})$$

$$Z_o(r_1) = \frac{120\pi}{\sqrt{\epsilon_{re}}} \sqrt{\frac{J_o^2(kr_1) + N_o^2(kr_1)}{J_1^2(kR_1) + N_1^2(kr_1)}} \quad (\text{A.1.2.c})$$

$$k = \frac{2\pi\sqrt{\epsilon_{re}}f}{c} \quad (\text{A.1.2.d})$$

$$l = r_2 - r_1 \quad (\text{A.1.2.e})$$

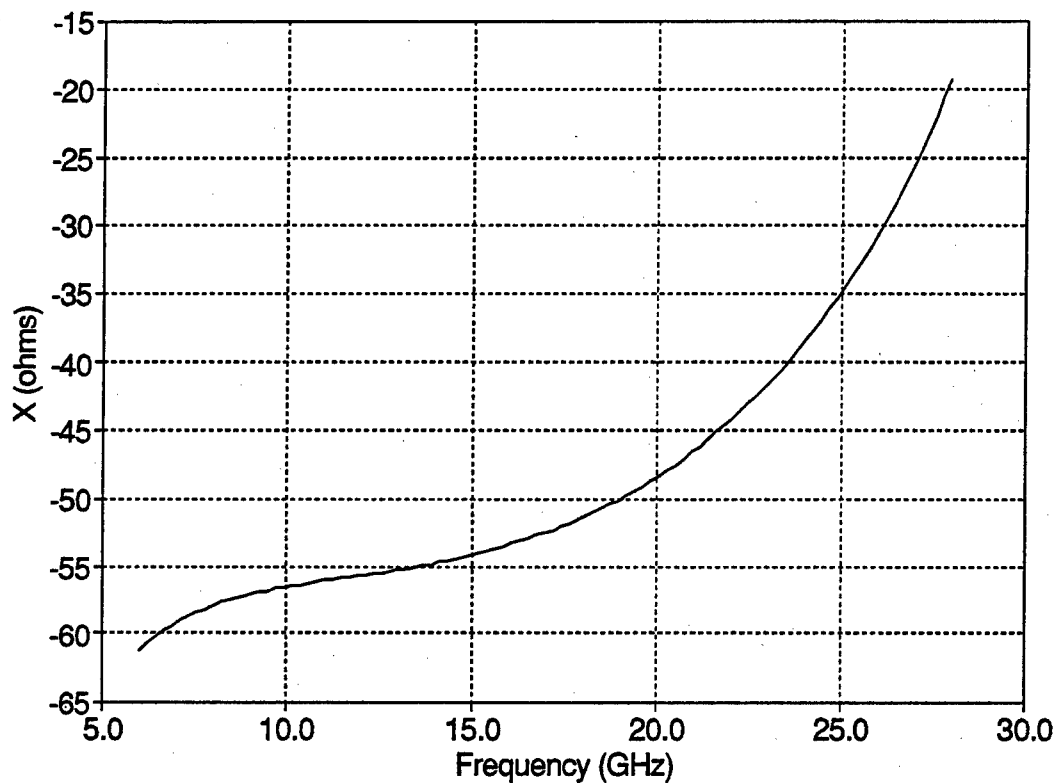


Figure A.3 Impedance of non-via-hole coplanar transition for second wafer design

X is minimized when

$$l \approx \frac{c}{2\pi f \sqrt{\epsilon_{re}}} \quad (A.1.3.a)$$

and X is maximized when

$$l \approx \frac{3.832c}{2\pi f \sqrt{\epsilon_{re}}} \quad (A.1.3.b)$$

In the calculations for these wafers r_1 was selected on basis of a 5 mil probe tip pitch.

A.2 First wafer designs

Figures A.4 and A.5 are views of the first two wafer designs. Only one of each wafer was successfully fabricated. Some initial measurements were made

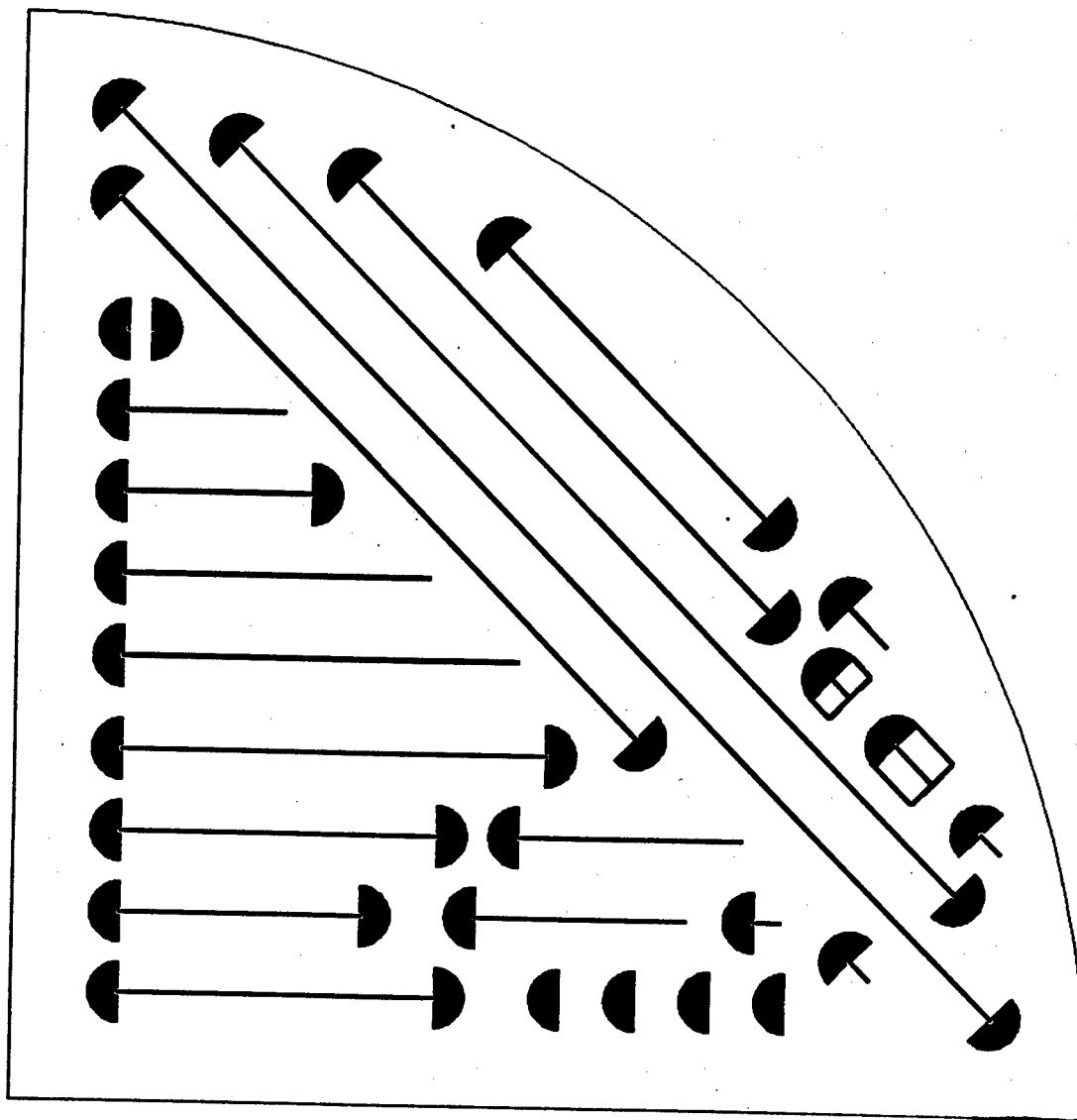


Figure A.4 Layout of first wafer design

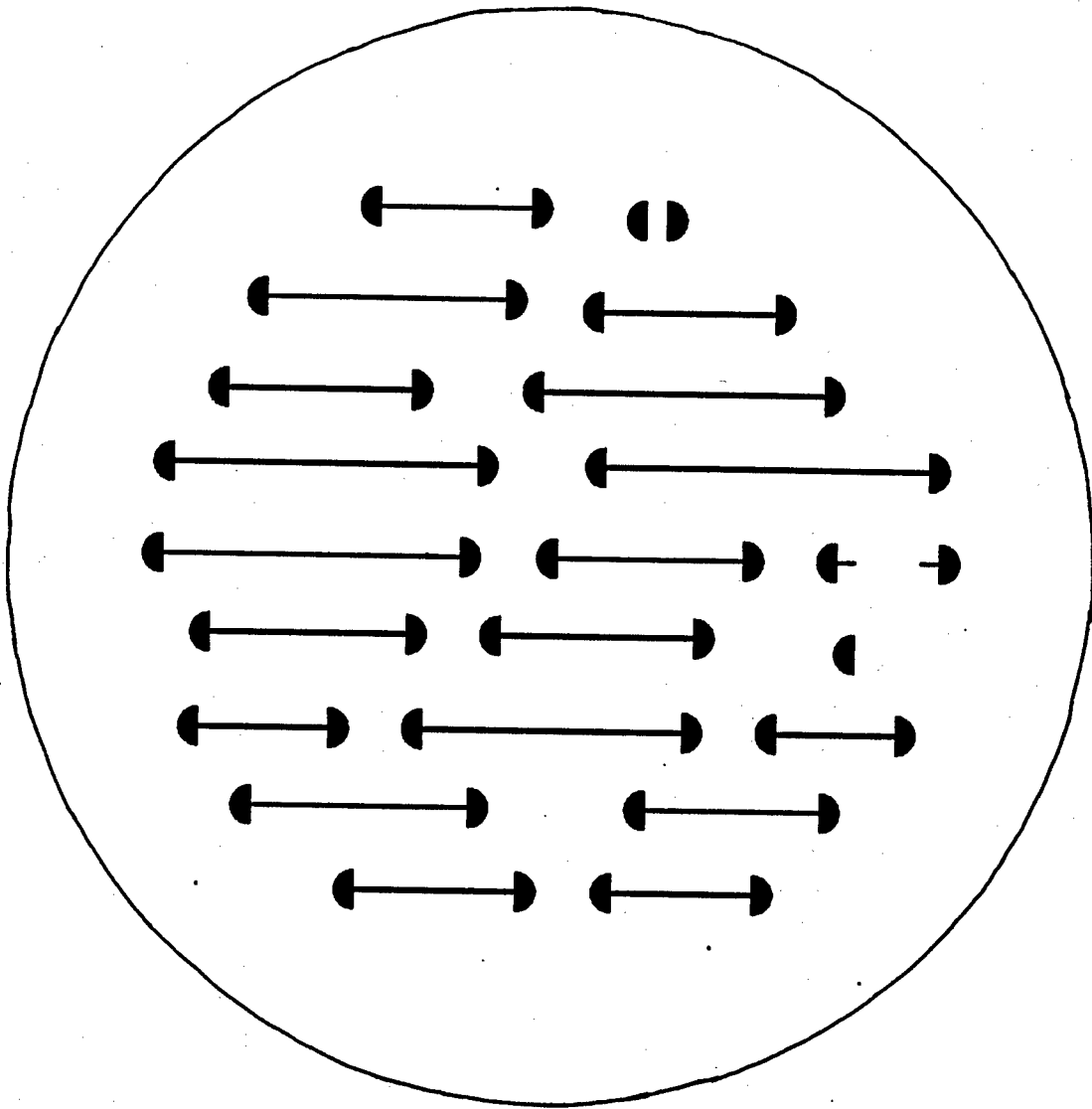


Figure A.5 Layout of second wafer design

on the first, and the second was broken shortly after completion. The first wafer is a 100 μ thick design just like the newer grooved wafer. Some two-port and one-port gap-coupled resonators are included, and their resonant frequencies were selected to be around 12 GHz and 17 GHz. There were long lines and calibration standards. This wafer was used in setting up the probe station at the University of Colorado. The second wafer had only one set of calibration standards and just resonators. The noteworthy thing about this wafer is that it was designed to be fabricated on unthinned (20 mil) GaAs, therefore eliminating another fabrication step. Thus these transitions are bigger and spaced farther apart. This wafer was simply an attempt to have something which could be easily and quickly fabricated, which seems to be something which cannot be asked of GaAs.

APPENDIX B

MEASUREMENT SETUP

This appendix presents the measurement setup at the University of Colorado at Boulder, and discusses how to use it. This setup is very versatile and provides the following:

- 1) general network analyzer functions,
- 2) optional computer control of network analyzer,
- 3) on-wafer probing of passive devices, and
- 4) on-wafer probing of active devices.

Figure B. 1 is a block diagram of this measurement system.

B.1 Power Up Sequence and Station Assembly

Ideally the 8510B and associated equipment would never be turned off. This would minimize thermal drift, which is a dominant source of error. However, the equipment usually gets turned off for various reasons, so the first thing to do when making measurements is to turn everything on and allow it to warm up for at least an hour - preferably several hours. The power up sequence is not critical except for one thing: the 8510B display and processor unit must be turned on last; otherwise there may be bus contention. One useful sequence is to turn on equipment in this order:

- 1) Outlet strip A
- 2) Microscope light (setting 2 is a good compromise between brightness and heat generation)
- 3) Chuck control power supply

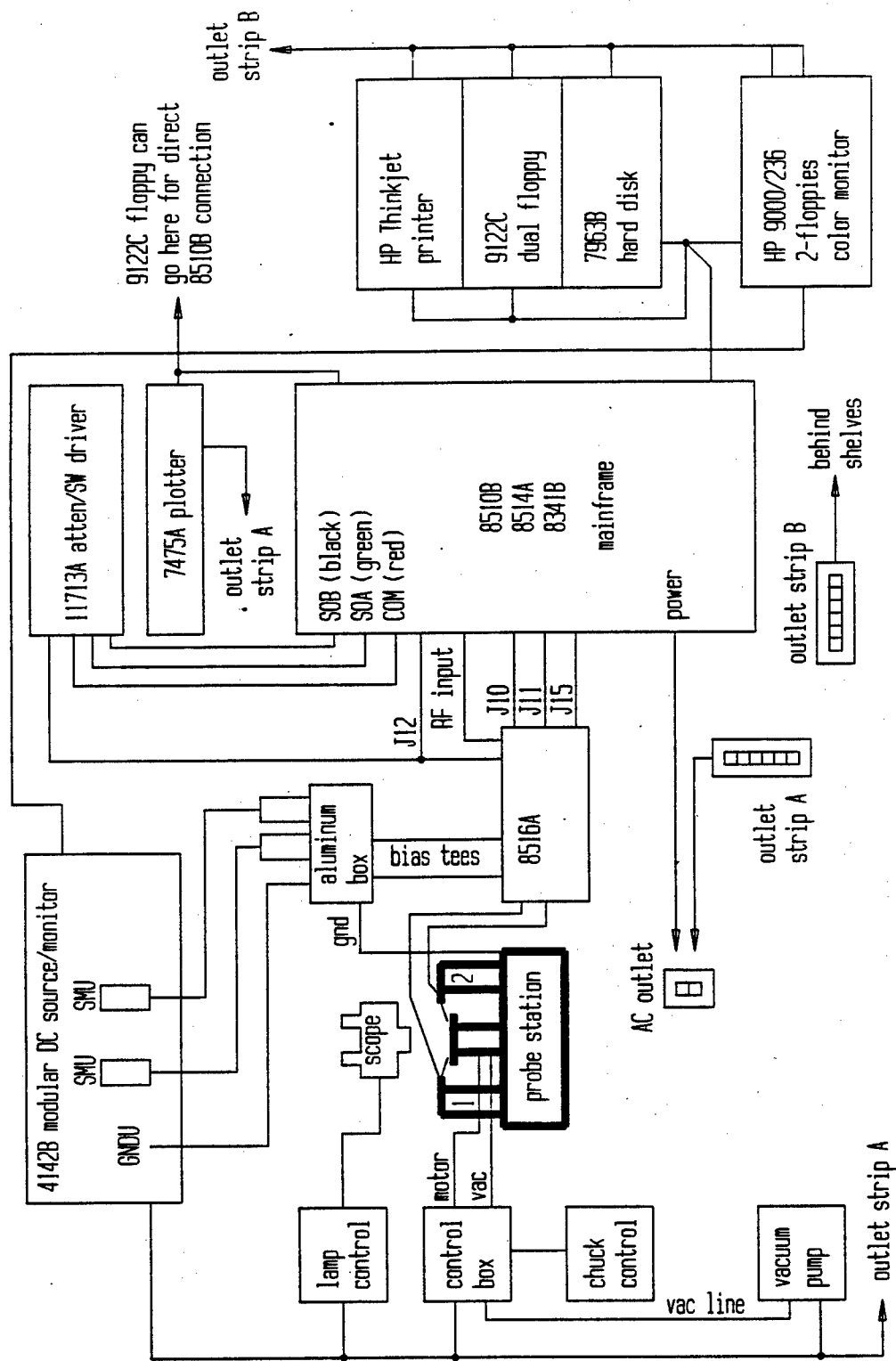


Figure B.1 Block diagram of the microwave measurement system at the University of Colorado at Boulder

- 4) 8341B source (from standby)
- 5) 8514A test set
- 6) Outlet strip B
- 7) HP 9000/236 computer
- 8) 8510B display and processor

Finally, the dual 3-1/2" disk drive can be connected to two places. If the computer will be controlling the measurements (i.e., if NIST's DEEMBED program is being used) and the floppy is to be accessed from the computer, then its cable must go to the HPIB connector on the back of the hard drive. If the 8510B is being used and files will be stored and/or recalled directly from the front panel, then the cable should be attached to the connector on top of the plotter.

Due to the large number of students with access to this area and the tips' fragility, probe tips are not left on the probe station. This is unfortunate, as it increases chances of probe tip breakage through increased handling. It also greatly increases wear on the probe tip and cable connectors, which must be put on and taken off each time.

To mount the probe tips, make sure the probe arms are backed about halfway back from the stage (using the x-axis knobs on the left and right ends of the probe arms). This gives enough room to turn the Allen wrench without hitting the microscope housing. Now mount each probe tip in turn using the screws and an Allen wrench. Be careful not to let the probe tips contact anything, and tighten them down securely. Now attach the cables to the probe tip connectors. The cables are flexible to a certain degree. Grasp the cable and hold it so that the threads line up with those on the probe tip connector, and tighten it down finger-tight. Using the 3.5mm torque wrench and keeping the cable from rotating by holding a finger in front of it, tighten the connector.

Now the station is ready for sample loading and probing. When the measurement session is concluded, shut down the systems and remove the probe tips by reversing the order of the above procedure.

B.2 Mechanics of Probing

Before one attempts probing, one should have read the documentation contained in the probe station user's manual and one should have received hands-on training from someone with prior probing experience. The documentation contained in the other parts of this manual describe the operation of the probe arm micrometers and the electronic chuck control system.

To dispel any myths or rumors to the contrary, the z-axis stage or chuck will not "run away" and crush the sample against the probe tips. If there is a glitch or power shutdown and restoration, the stage will go through its auto-zero routine. This routine involves the chuck going to its zero position, which is all the way down. As it does its calibration, it cycles up and down below this zero position. Any type of glitch or reset will cause the chuck to go down—not up. The only way to damage the sample or the probes is operator error—by manually running the stage up against the probe tips. The HP computer does not control the z-axis stage!

Probing a sample requires a plan. One should know beforehand what things will be measured, what standards will be used for calibration, etc. and have a sequence in mind. This minimizes the time for the test set to drift. The normal time scale after which drift noticeably affects measurements (especially using on-wafer TRL and higher frequencies, above 30 GHz) is about two hours. Since placing the probes, saving data, and computing coefficients (using NIST's DEEMBED) are very time-consuming, it is mandatory to have a probing sequence in mind.

When ready to probe, pull the stage out by sliding it along the grease

plate. Apply a downward as well as a horizontal component of force; if an upward component is applied in haste or carelessness, the grease plates could part and the stage could fly up and impact the probe tips (this is, of course, operator error!). It is also advisable to move the stage horizontally slowly. This, like all facets of on-wafer probing, requires practice. After the stage is out, rest the sample on it in the center and apply vacuum. Move the stage back in.

Using the microscope on about 30X, place the scope in the center and position the probe tips within the field of view. This is somewhat more critical in the y-axis (in-and-out) so that, as the probes are moved in x, they remain in view. Now focus on the bottom of the probe tips. The reason for this is that when the sample comes into focus as the stage is raised in z, it will be in contact when it is in focus. Only rarely adjust the z-axis micrometers! Especially leave the LEFT one at "0". If the probe tip bottoms are not at equal heights, adjust the RIGHT micrometer. The best way to do this is to contact a noncritical area of the sample.

The probe tips are mounted at about an 11-degree angle with the horizontal. After the tips make contact and the stage is advanced past that stage in z, the tips will skid on the surface of the sample. The extra height past contact is called overtravel, and due to the 1:5 angle of the probes, the tips will skid 5 units on the sample for every 1 unit of overtravel. Make sure to use the recommended amount of overtravel for the probe tips being used.

There is one final adjustment to be made before measurements can be made, and it must be checked and adjusted, if necessary, before every contact on the sample. This adjustment is planarity. The only way to effectively tell if the probe tips are planar is to contact the sample (in an unobtrusive place) NEAR where the contact will be made. If only two marks are made (or one!) then the

probe tip must be rotated with the supplied Allen wrenches that are kept on the probe arm near the planarity adjustment screws. Since the sample will rarely be flat, this check must be performed all over the sample if accurate results are to be obtained – especially with TRL on-wafer calibration of microstrip media.

On-wafer probing is a skill that can only be improved with practice. Everyone develops their own techniques and their own ways of “feeling” what is happening with the equipment. Care, though, is always required—care and awareness of a myriad of tiny details. Perhaps this appendix will eliminate some of the tedium and time of finding and learning some of those details.

APPENDIX C

CITIFILE FORMAT CONVERSION

This appendix describes how to port data from the HP 8510 network analyzer to the HP workstations and, if desired, from there to a DOS machine.¹ The conversion of the resulting files to a format useable by other programs or user-written software is also discussed.

The 8510 currently has a dual disk drive attached to it; disk 0 is the one to which the 8510 defaults on power-up. This drive (and the ones connected to the workstations) only read and write 730K 3-1/2" floppy disks.

When you want to save data which is being measured and/or displayed on the 8510, insert a disk into drive 0. Press the TAPE hardkey at the bottom center of the 8510 display unit. There are two softkeys under STORAGE IS; they are TAPE and DISC. If the DISC selection is not already indicated, press that softkey. (The machine will power up with storage set to TAPE.) Now press the STORE softkey; a menu of choices as to what data can be stored will present itself. Usually you will want to press MORE and DATA (under the DATA: heading. The measured data will be stored. The three choices under the DATA: heading are RAW, DATA, and FORMATTED. Raw data is what the 8510 measures before calibration is applied; data under the DATA heading has been processed with the current cal set (if calibration is on). Formatted data is stored in the manner in which it is displayed. (Example: if you were viewing S₁₁ data in log

¹ Step-by-step commands pertain to the network in the MIMICAD Center at the University of Colorado at Boulder.

magnitude format, it will be stored as log mag S_{11} , 0.0) Data is normally saved in real, imaginary format. Formatted data, though, is just what is displayed upon the 8510's screen. The 8510 stores these files in a format called "lif". It also capitalizes the file names. Since UNIX is case-sensitive, these filenames must be typed in upper case on the workstation. Once the data files are stored on disk, they can be copied to your workstation account.

There are two HP workstation drives, referred to as `/dev/rmdleft:` and `/dev/rmdright:`. These drives are connected to kamikaze, so if you logged on to a different workstation, you must `rlogin kamikaze`. Once you are properly logged in,

```
lifcp /dev/rmdleft:source-file destination-file
```

or

```
lifcp /dev/rmdright:source-file destination-file
```

will copy the desired file to your account. Other basic file commands are made by joining "lif" with basic UNIX file commands; for instance,

```
lifls /dev/rmdleft:
```

will list the files on the disk in the left drive.

UNIX and DOS store files in a slightly different manner. In order for other programs (such as editors and plot programs) to work correctly with these files, a conversion must be performed after a transfer in either direction. If a file is to be copied to a DOS disk, it must be converted with

```
ux2dos filename > newname.
```

On the other hand, if a file was just copied from a DOS disk (or uploaded via modem), this command must be executed:

```
dos2ux filename > newname.
```

When you are ready to copy files to a DOS disk, commands similar to `lifcp` and `lifls` are available. The command

```
doscp source-file /dev/rmdright:destination-file
```

copies a file from the workstation to a DOS disk in the left drive. Remember, DOS only allows eight characters in a filename and three characters in the extension, and is not case-sensitive. Likewise,

```
dosls /dev/rmdright:
```

lists the files on a DOS disk in the right disk drive.

The HP 8510 also arranges the data in the file it stores in a manner referred to as citifile format. This refers to the arrangement of information in the header and the ordering of data in the rest of the file. Figure C. 1 is an example of a raw data file. The first two lines are always the same for this machine. The next line indicates whether data is raw, measured, or formatted (NAME_RAW_DATA, NAME_DATA, or NAME_FORMATTED, respectively). The next line gives some information not normally needed. In the next four lines the data that is actually stored is indicated; these are usually S-parameters in real, imaginary (RI) format. The middle line of the next three lines always contains SEG, a space, start frequency in hertz, a space, end frequency in hertz, a space, and the number of points. Each S-parameter is then stored with a line saying BEGIN, then the S-parameters themselves, and then a line saying END. This is a file format which is of little use to most other programs.

A FORTRAN program called `convert.f`, compiled to an executable `convert`, is available. It prompts for source filename, checks to see if the source is a valid data file, and finds out how many S-parameters are stored. The user then enters the destination filename and indicates whether separate files or one multi-column file are desired. Separate files will have appropriate extensions (.S11, .S21, etc.). The one combined data file will have the extension .DAT, but if this option is selected and only one S-parameter is stored, it will still be given the proper .Smn extension. The program stores converted data in

columns with frequency in GHz in the first column and converted S-parameters in the following columns, in one of a choice of formats: log magnitude/phase (degrees), linear magnitude/phase (degrees), or real/imaginary. The source code is available and easily modified.

Table C.1 Example HP 8510 raw data file in citifile format

```
CITIFILE A.01.00
#NA VERSION HP8510B.05.00
NAME RAW_DATA
#NA REGISTER 1
VAR FREQ MAG 801
DATA S[1,1] RI
DATA S[2,1] RI
DATA S[1,2] RI
DATA S[2,2] RI
SEG_LIST_BEGIN
SEG 150000000000 180000000000 801
SEG_LIST_END
BEGIN
4.97345E-1,-4.86526E-1
3.40637E-1,-6.30218E-1
.
5.16143E-1,-4.17022E-1
3.29437E-1,-5.48584E-1
END
BEGIN
-2.54839E-4,-0.03740E-4
-4.33698E-4,-4.10512E-4
.
-3.15159E-4,-5.86032E-4
-5.95986E-4,-7.71135E-4
END
BEGIN
-2.36421E-4,0.43705E-4
0.17419E-4,-2.93001E-4
.
-1.68502E-4,-1.14297E-3
-0.85659E-4,-1.60181E-4
END
BEGIN
-5.18096E-1,5.07598E-1
-3.30230E-1,6.30218E-1
.
-3.36669E-1,5.16082E-1
-1.83136E-1,6.15173E-1
END
```